NTNU

Norwegian University of
Science and Technology

Production of Lead-free Electroceramics

K0.5Na0.5NbO3 substituted with Li & Ta

Jon Martinsen Strand

Nanotechnology

Submission date: June 2011

Supervisor: Kjell Wiik, IMTE
Co-supervisor: Tor Grande, IMT
Mari-Ann Einarsrud, IMT
Astri Haugen, IMT

Norwegian University of Science and Technology
Department of Materials Science and Engineering

Declaration

I, Jon Martinsen Strand, hereby declare that the work presented in this document has been performed by myself, without any help, guidance or supervision, exceeding, surpassing, or otherwise violating, that which is allowed, according to the current rules and regulations of the Norwegian University of Science and Technology (NTNU). Thus, this thesis is the result of my own research work.

Trondheim, June 8th 2011

Jon Martinsen Strand

Preface

This thesis is submitted to the Norwegian University of Science and Technology (NTNU) in partial fulfillment of the requirements for the degree of Master of Science.

The work presented in this report was conducted at the Department of Materials Science and Engineering, NTNU, Trondheim, between January 20th and June 3rd, 2011.

Professor Kjell Wiik served as main supervisor, and Professor Tor Grande and PhD candidate Astri Bjørnetun Haugen as co-supervisors.

Acknowledgements

First of all, I want to thank my supervisor Professor Kjell Wiik, as well as my co-supervisors Professor Tor Grande and PhD candidate Astri Bjørnetun Haugen, without whom this work would not have been possible. Their insight and helpfulness proved to be a significant source of input in this project. Professor Mari-Ann Einarsrud also was of great help, and is acknowledged for her enthusiasm, and willingness to share important insights. I also wish to thank the team at Ceramic Powder Technology AS, together with whom I now have worked for 3 years, which has provided me with a very useful experience basis for carrying out my thesis work. Thanks to Svein Arne Pedersen, Marte Aurstad Aspnes, Ruth Astrid Strøm and Lars Petter Bjørkeng for their combined dedication, devotion and determination.

Post doc. Sverre Magnus Selbach is highly acknowledged for his help in understanding and interpreting critical results, and sharing from his widespread experience. Post doc. Maxim Morozov is recognized for his sharing of knowledge and contributing to a piezoelectric understanding. PhD candidate Ky-Nam Pham is acknowledged for his help and support.

Many thanks go to Julian Richard Tolchard for training me to use the Scanning Electron Microscope as well as the Energy-dispersive X-ray spectroscopy, and providing top quality feedback on arising issues.

Special thanks go to Chief Engineer Eli Beate Larsen and PhD candidate Sophie Beatrice Weber, for always being present and helpful.

HSE-responsible and Staff Engineer Gunn Torill Wikdahl is acknowledged for always ensuring a safe working environment, and dealing swiftly with pressing and important issues.

I also wish to thank Solveig Jonassen and Staff Engineer May Grete Sætran, for several times making me speechless by being able to provide even the most exotic equipment on short notice.

Staff Engineers Elin Harboe Albertsen and Harald Holm have been significant resources, and have saved the day countless times.

Finally I wish to state that I feel a large degree of gratitude towards the amazing people working in the Department of Material Science and Engineering, for constantly maintaining a positive, optimistic and effective working environment!

Abstract

$K_{0.485}Na_{0.485}Li_{0.03}Nb_{0.8}Ta_{0.2}O_3$ powder has been prepared by spray pyrolysis of aqueous solutions of K/Na/Li nitrates mixed with water soluble Nb and Ta precursors. The as-prepared ceramic powder was calcined at 600 °C to remove any organic residues after the spray pyrolysis process. Different milling methods for the calcined powders were attempted, revealing dry planetary milling to be the most suitable milling method. The powders were characterised using scanning electron microscopy. A complete milling process was developed based on sufficient destruction of the egg-shell like agglomerates from the spray pyrolysis process, avoidance of flake formation and reproducibility. Sintering was attempted using three different sintering methods, all using the reverse crucible method to limit the amount of alkali evaporation. An optimal temperature range was found for each of the three, achieving densities in the range of 94-97%. The microstructure of the different samples was explored by polishing the samples and investigating the surfaces by scanning electron microscopy. It was found that the average grain sizes were in the range of a few microns, with large variations in the broadness of the grain size distribution when comparing different sintering methods. For two of the three sintering methods a standard deviation of less than 0.3 micron is reported. An EDS analysis was performed, and it was found that all the samples demonstrate compositional homogenity.

Dielectric testing was performed on the samples sintered using the three different sintering methods. Polishing of the sample surfaces and storage in dessicators had to be performed in order to avoid moisture influence and achieve reproducibility. The piezo- and ferroelectric effect was observed for all the different sintering methods, along with coercive fields in the range of 669 - 889 $\frac{V}{mm}$ and remnant polarizations in the range of 16 - 29 $\frac{\mu C}{cm^2}$, depending on the sintering method used. A strictly monotonic relationship between average grain size and the coercive field was identified. The normalized strain d_{33}^* was found to be in the range of 230 - 330 $\frac{pm}{V}$, after poling using an electric field of 4 $\frac{kV}{mm}$ at 100 °C. It is argued that on the basis of the present results, $K_{0.485}Na_{0.485}Li_{0.03}Nb_{0.8}Ta_{0.2}O_3$ has potential as a leading candidate for environmentally friendly ferroelectric materials, and spray pyrolysis seems an excellent choice of synthesis method.

Contents

1 Introduction

1.1 Motivation

Electroceramics is a group of very important materials, used primarily for their electrical properties. They are applied in most components that are used in electronics. While ceramics have traditionally been admired and used for their mechanical, thermal and chemical stability, the electrical, optical and magnetic properties of electroceramics have become of increasing importance in many key technologies including communications, energy conversion and storage, electronics and automation. Materials with such properties are now classified under electroceramics, as distinguished from other functional ceramics such as advanced structural ceramics [9].

Among electroceramics are capacitators with high dielectric constant, piezoelectric transducers, sensors, switches and ferroelectric thin films. Ceramic materials based on lead zirconate titanate, $Pb[Zr_xTi_{1-x}]O_3$ (PZT), have been the most common materials for this purpose for decades [9]. It is however a great interest in lead-free piezo/ferroelectric materials, as several EU-directives point to the fact that PZT needs to be replaced. This is due to the amount of lead contained in PZT, causing it to be hazardous [2, 3, 7]. One of the more promising materials to replace PZT is $K_{0.5}Na_{0.5}NbO_3$ (KNN) [6]. $Li_{0.5}Na_{0.5}NbO_3$ (LNN) has also been viewed as a possible alternative, but the piezoelectric properties have been found un-satisfactory in comparison with those of the PZT piezoelectrics [7].

Recently, KNN doped with Li & Ta (LKNNT) was found to have an electric-field-induced strain comparable to typical actuator-grade PZT. Lead-free piezoelectric ceramics with properties that closely match those of PZT were reported by Saito et al. [1]. One of the key challenges of KNN-based ceramics is the optimization of the sintering process, and to obtain high densities [35, 36]. Spray pyrolysis has earlier been used to synthesize LKNNT, and a pure orthorombic perovskite phase was achieved, demonstrated by X-ray diffraction (XRD) measurements. [51]. The piezo- and ferroelectric behaviour of the material was observed and reported. Still, many areas of improvement were identified, such as establishing an optimal powder pretreatment process, achieving higher sintered densities, as well as improved and reproducible dielctric properties.

1.2 Aim of work

In this project it will be attempted to develop a suitable processing route for KNN doped with $LiTaO_3$, $K_{0.485}Na_{0.485}Li_{0.03}Nb_{0.8}Ta_{0.2}O_3$ (LKNNT), synthesised using spray pyrolysis. The dielectric and sintering properties of the resulting material are also of great interest, as it shows how applicable the material is and how it can be processed. These properties will therefore be explored as well.

This will be done by milling and sintering attempts, identifying relevant parameters and making them subject to variation. The powder morphology and microstructure will be studied using Scanning Electron Microscopy (SEM), and the achieved densities will be measured by Archimedes' method. The compositional homogenity will be studied using Energy-dispersive X-ray spectroscopy (EDS). The dielectric properties will be explored using a dielectric test module which applies voltage to the material and measures displacement and polarization.

2 Theory

2.1 Piezoelectricity and ferroelectricity

2.1.1 Definitions

All materials experience a small change in dimensions when subjected to an electric field. If the resultant strain is proportional to the square of the field it is known as the electrostrictive effect. Some materials show the reverse effect, that is, the development of electric polarization when they are strained through an applied stress. These are said to be *piezoelectric* (the term originates from the Greek word "piezo", which translates to "pressure"). To a first approximation the polarization is proportional to the stress and the effect is called the "direct piezoelectric conversion". For these materials the reverse effect is also possible, shown as the development of a strain directly proportional to an applied electric field, which is known as the "converse piezoelectric effect" (see Figure 2.1) [4, 9, 29, 30].

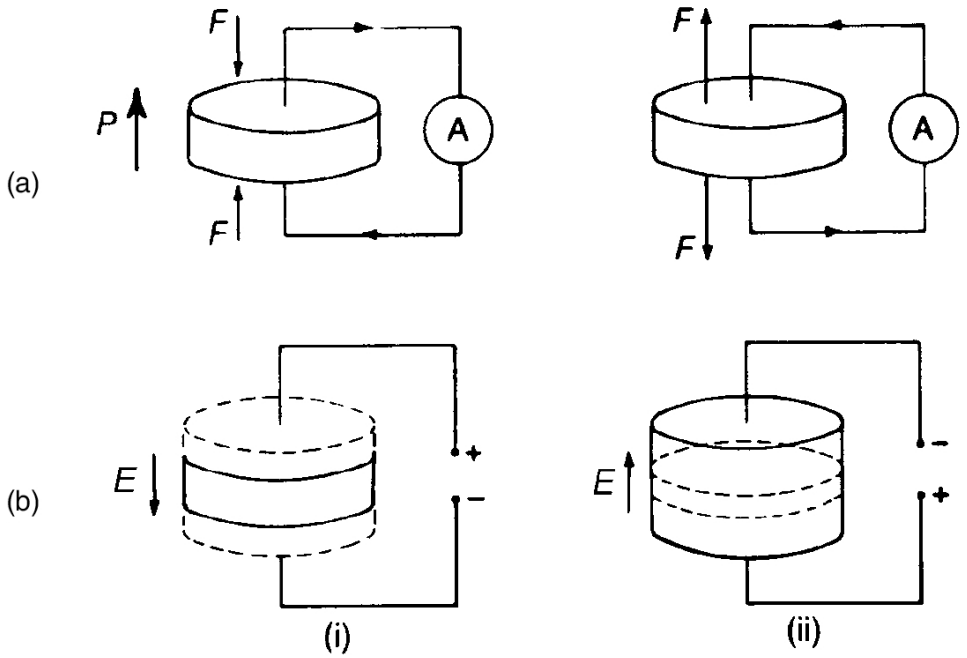

Figure 2.1: The piezoelectric direct and converse effect. When a voltage is applied across the material it expands in the direction of the field and contracts perpendicular to the field. When a force is applied to the piezoelectric, an electric field is generated. Image aqquired from Moulson et al. [4].

The symmetry elements used to define symmetry about a point in space, that is, the central point of a unit cell, are (1) a center of symmetry, (2) axes of rotation, (3) mirror planes, and (4) combinations of these. All crystals can be divided into *32 different classes* or point groups utilizing these symmetry elements (see Figure 2.2). These 32 point groups are members of the seven basic crystal systems that are, in order of ascending symmetry, triclinic, monoclinic, orthorhombic, tetragonal, rhombohedral (trigonal), hexagonal, and cubic.

Of these 32 point groups/crystal classes, only 21 are non-centrosymmetric, meaning that they do not have a centre of symmetry.

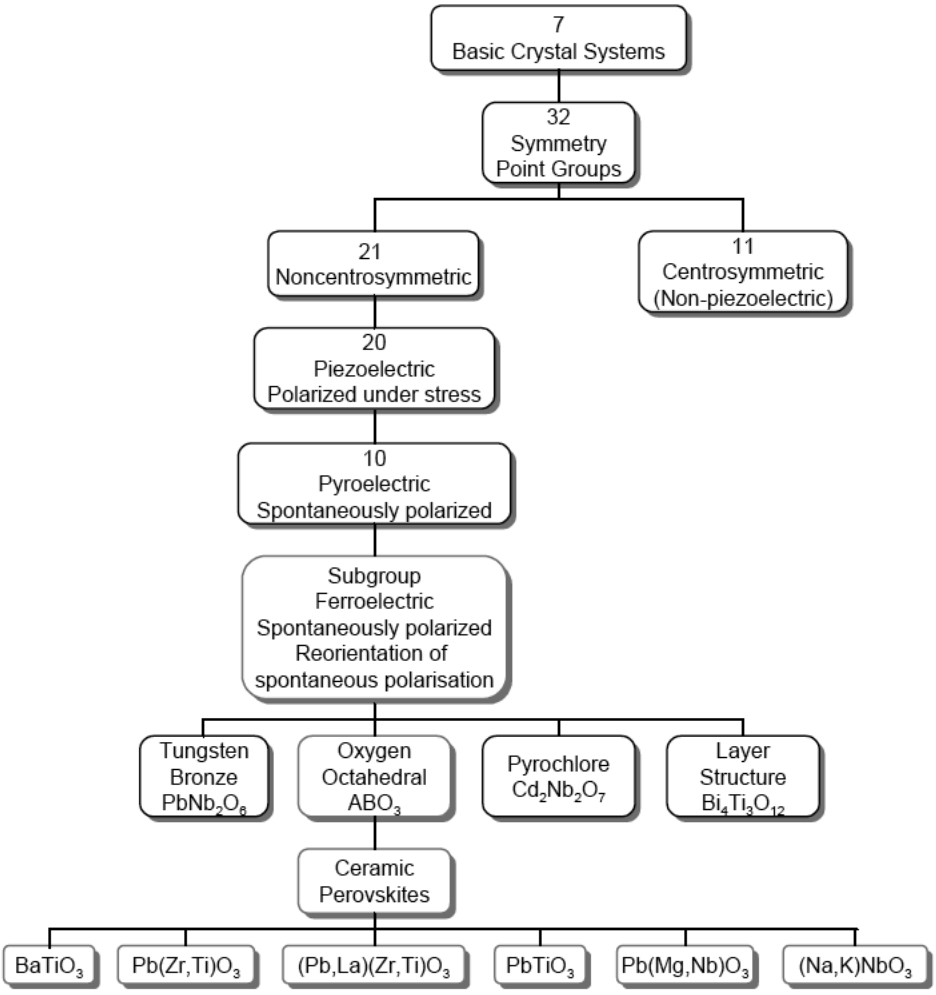

Figure 2.2: An overview of the different symmetry point groups, showing how many are piezoelectric. Image acquired from Haertling [9].

One class, although being non-centrosymmetric, is not piezoelectric because of other combined symmetry elements (all piezoelectric moduli are zero due to the high symmetry), leaving only *20 piezoelectric point groups* [9]. The non-centrosymmetry condition is a necessary condition for piezoelectricity to exist, because a homogeneous stress is centrosymmetric and cannot produce an unsymmetric result (such as a polarization), unless the material lacks a center of symmetry. In that case an applied stress leads to net movement of the positive and negative ions with respect to each other and produces electric dipoles and a net polarization. In the other case, the material experience symmetrical movement of ions, meaning there is no net polarization (see Figure 2.3 and 2.4).

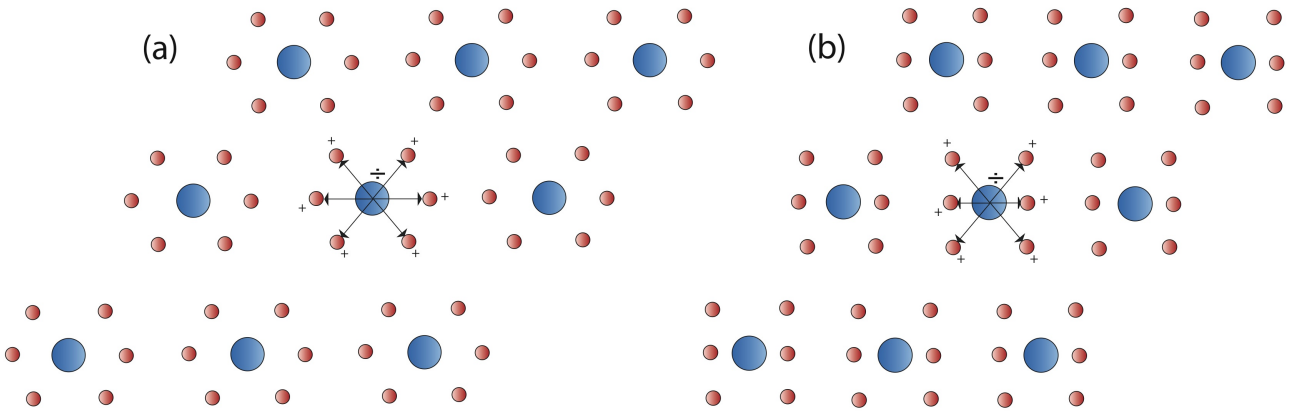

Figure 2.3: Planar model of a crystal having a center of symmetry, being centrosymmetric: (a) The centers of gravity of the positive and negative charges coincide; the arrows indicate the separate electric dipole moments of a group of charges. (b) A compressive stress changes the distances between the charges (in this case along the horizontal axis) but does not change the angles. As any charge has an equal charge on the opposite side of the symmetry element (the blue atom), a net dipole moment cannot be produced.

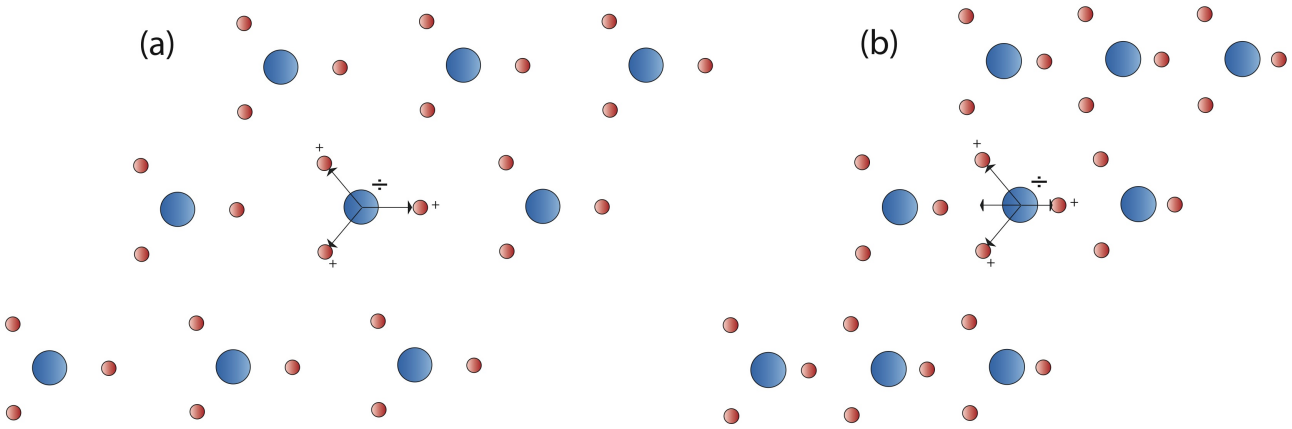

Figure 2.4: Planar model of a crystal lacking a center of symmetry, being non-centrosymmetric: (a) The centers of gravity of the positive and negative charges coincide; the arrows indicate the separate electric dipole moments of a group of charges. (b) A compressive stress changes the distances between the charges (in this case along the horizontal axis) but does not change the angles. The blue atom does no longer represent an inversion point, thus a dipole moment can be produced. The horizontal arrow pointing to the left represents the resultant electric dipole moment of a group of charges.

10 of the 20 piezoelectric classes have a unique polar axis, which means that the electric dipole moment is found only along a unique polar direction which has no symmetrically equivalent directions. These special classes of crystals are called *pyroelectric* and they exhibit a permanent, spontaneous polarization below a characteristic temperature, known as the Curie temperature, T_C. A subgroup of the pyroelectric class is known as *ferroelectric*, characterized by the possibility to switch the permanent electric dipole moment reversibly by applying an electric field. In other words: ferroelectric materials are required by symmetry considerations to also be piezoelectric as well as pyroelectric.

Ferroelectrics thus exhibit a spontaneous electric polarization below the Curie temperature, a hysteresis loop, and an associated mechanical strain. Ferroelectrics have reversible spontaneous polarization. The word *spontaneous* refer to that the polarization has a nonzero value in the absence of an applied electric field. The word *reversible* refers to the direction of the spontaneous polarization that can be reversed by an applied electric field in opposite direction [5].

2.1.2 Piezoelectrics in the electronics industry

As mentioned in Section 1.1, piezoelectric ceramics are heavily applied in many electronic components. Shrout et al. states that the dependence of piezoelectric components in the electronics industry is so large, that in the past, innovations in *actuators, sensors, and ultrasonic transducers* have been the driving force for new developments in piezoelectric ceramics [6].

Due to their intrinsic dielectric nature and also a large number of interactive and electrically variable properties, ferroelectric ceramics are probable to figure prominently in the future. Bulk, thick-film, and thin-film forms of these materials have now proved their worth, and it is likely that they will constitute a strong portfolio of materials for future applications in electronics as well [9]. Figure 2.5 shows an example of an application, the auto zooming mechanism (by mechanical motion, not "digital" zooming) in a camera. The optical zoom requires more than 2 mm stroke, which can be realized by a piezoelectric micro ultrasonic motor (USM) [37]. Figure 2.6 shows another example, an injection valve. In order to increase the diesel engine efficiency, high pressure fuel and quick injection control are required, and the multiple injections should be realized in a very sharp shape. For this purpose, piezoelectric actuators were adopted [39].

The most useful and applied piezoelectric materials display a *transition region* in their composition phase diagrams, known as a *morphotropic phase boundary* (MPB), where the crystal structure changes abruptly and the electromechanical properties therefore are maximal. The search for alternative piezoelectric materials is therefore being focused on systems in which a MPB will occur [41, 42, 43, 44]. Properties of ferroelectric solid solutions may also be considerably enhanced in the vicinity of a MPB, where solid solution changes structure as a function of the chemical composition [40, 45].

Figure 2.5: Camera auto zooming/focusing mechanism with two USM's [37].

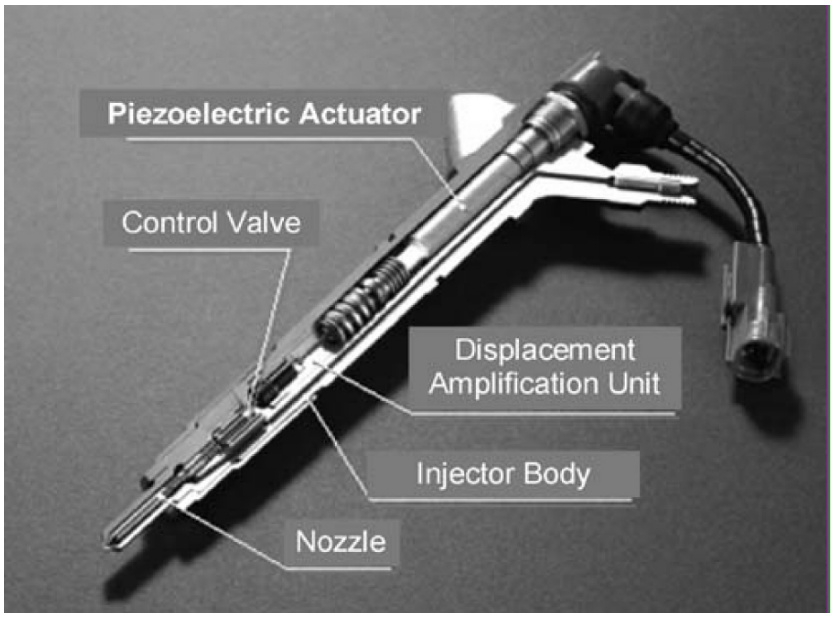

Figure 2.6: Diesel injection valve with a piezoelectric multilayer actuator [38].

2.1.3 Measurements and response

In general, piezoelectric properties are dependent on orientational direction, so they must be described in terms of tensors. A convenient way to specify the directional properties is to use subscripts that define the direction and orientation. The subscript 3 refers to the polar axis (or poling axis). 1 and 2 refer to arbitrarily chosen orthogonal axes perpendicular to 3 [5]. A measure of the piezoelectricity of a material is the material-specific piezoelectric *charge sensor constant* d_{33}. It is defined as the polarization generated per unit of mechanical stress applied to a piezoelectric material or, alternatively, the mechanical strain experienced by a piezoelectric material per unit of electric field applied. The subscript "33" then indicates that the polarization generated is measured in the same direction as the direction the stress is applied in (d_{31} is a related constant, where the polarization generated is measured in the direction perpendicular to the direction the stress is applied in). The piezoelectric charge sensor constant is thus an important constant, as high values of this constant are desirable for those materials that are utilized in motional or vibrational devices, such as sonars and sounders [9]. It is common to measure these constants using resonance–antiresonance methods or a Berlincourt d33-meter [1, 10, 11].

It is also common to instead calculate the *normalized strain* d^*_{33}, usally obtained from the strain measured under an unipolar electric field. The normalized strain is calculated from the ratio of the maximum strain to the maximum electric field from the unipolar strain curves, and has units $\frac{pm}{V}$ [12]. Differences in d_{33} and d^*_{33} are often observed, and could be correlated with different measuring frequencies [13].

$$d^*_{33} = \frac{\triangle S_{max}}{E_{max}} \left(\frac{pm}{V}\right)$$

Figure 2.7(a) shows the strain–electric field characteristic for a piezoelectric ceramic and Figure 2.7 (b) the absence of significant hysteresis in a electrostrictive ceramic [4].

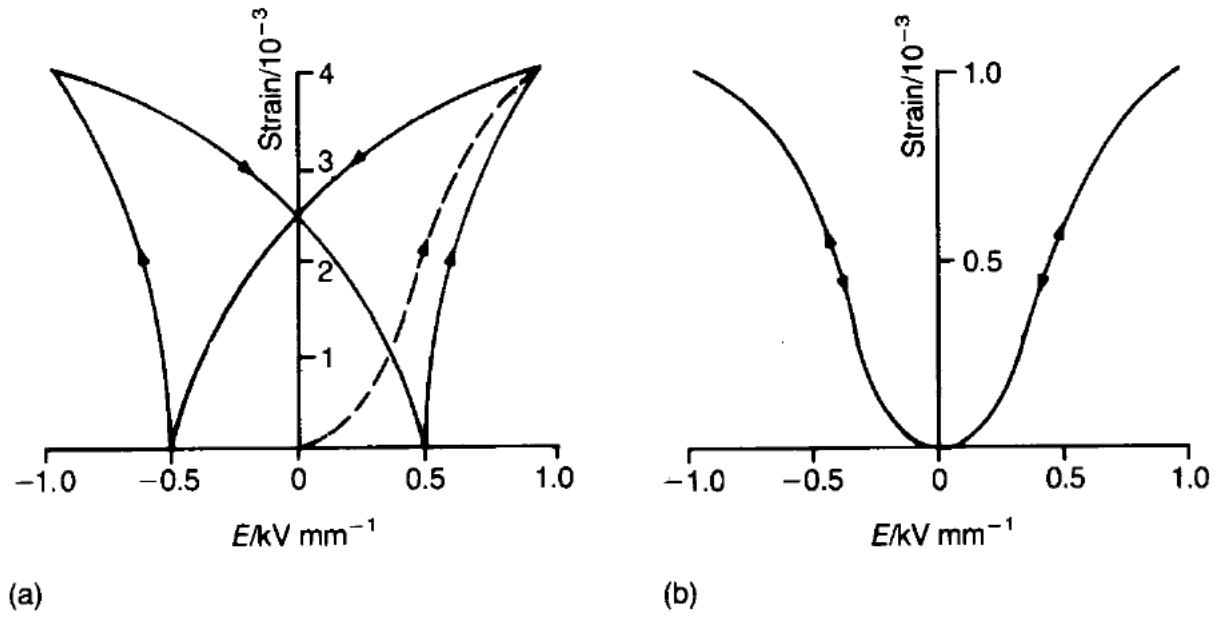

Figure 2.7: Dependence of strain on electric field for (a) a readily poled and depoled piezoelectric ceramic and (b) an electrostrictive ceramic. Image aqquired from Moulson, J. et al. [4].

A typical ferroelectric hysteresis loop is shown schematically in Figure 2.8. When the field is small, the polarization increases linearly with the field. This is due mainly to field-induced polarization, because the field is not large enough to cause orientation of the electrical domains (OA). At higher electric fields, polarization increases nonlinearly with increasing field, because all the domains start to orient themselves towards the direction of the field (AB). At even higher electric fields, polarization will reach a state of saturation corresponding (BC), where most domains are aligned towards the direction of the poling field. If the field is now gradually decreased to zero, the polarization will decrease, following the path CBD. OD represents the remnant polarization P_r. The field required to bring the polarization to zero is called the coercive field F_C or E_C . The coercive field depends not only on temperature, but also on the measuring frequency and the waveform of the applied field [5].

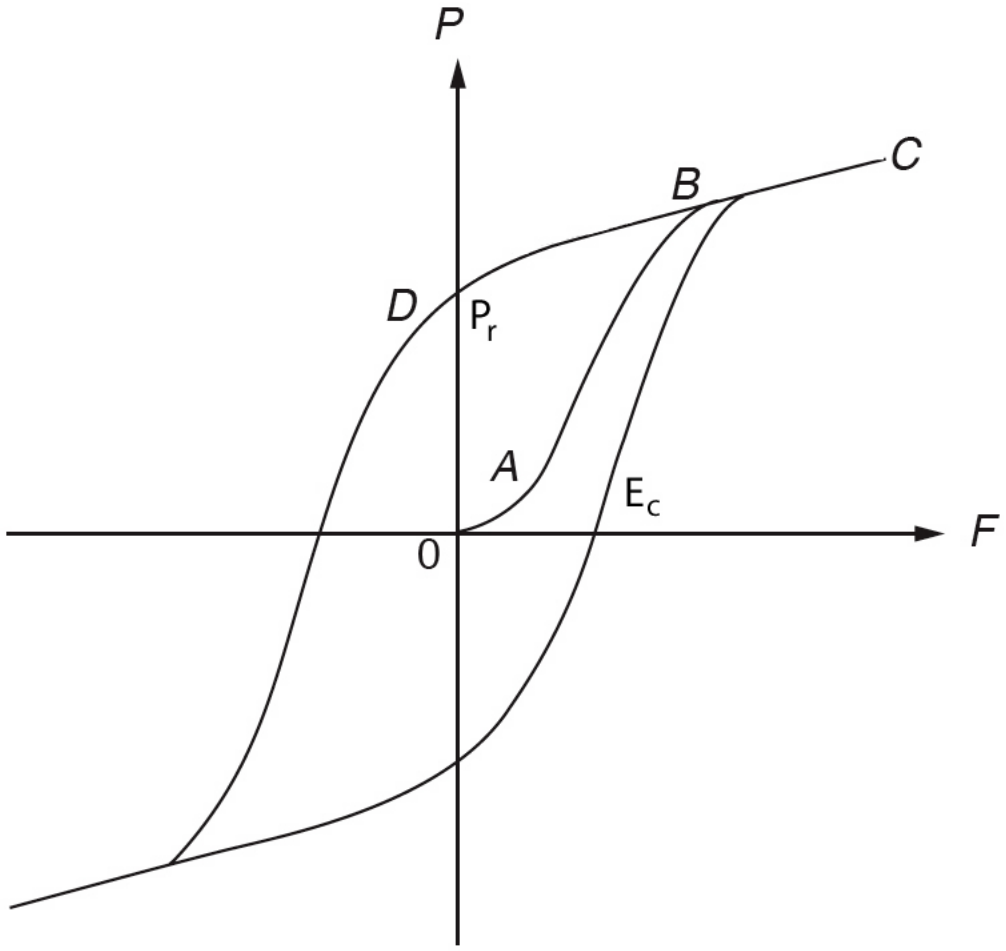

Figure 2.8: Schematic diagram of a typical ferroelectric hysteresis loop. Image aqquired from Kwan, C. [5].

2.1.4 Poling

A polar direction can be developed in a ferroelectric ceramic by applying a static field; this process is known as *poling*. The grains are not rotated themselves, but the crystal axes can be oriented by reversal, or by changes through other angles that depend on the crystal structure involved, so that the spontaneous polarization has a component in the direction of the poling field. Electrodes have to be applied to the ceramic for the poling process and these also serve for most subsequent piezoelectric applications [4]. It is common to pole the materials before performing piezoelectric measurements, usually at elevated temperatures [18].

2.2 Perovskites

A large group of ferroelectrics is the ceramic perovskites [9]. Many KNN-based ceramics are found to be perovskites [20, 28, 46]. A perovskite is a material which has the same type of crystal structure as calcium titanium oxide ($CaTiO_3$) known as the perovskite structure, or ${}^{XII}A^{XVI}B^{Y}O_3^{2-}$ (X+Y=6) with the oxygen in the face centers [15]. The general chemical formula for perovskite compounds is thus ABO_3, where "A" and "B" are two different cations of very different sizes, and the O-anion bonds to both cations. The "A" atoms are larger than the "B" atoms. The ideal cubic-symmetry structure of the perovskite has the B cation in 6-fold coordination, surrounded by an octahedron of anions, and the A cation in 12-fold cuboctahedral coordination.

A possible way to visualize this structure is in terms of the BO_6 octahedra which share corners infinitely in all 3 dimensions, creating a highly symmetric structure. The A cations occupy every hole which is created by 8 BO_6 octahedra, giving the A cation a 12-fold oxygen coordination, and the B-cation a 6-fold oxygen coordination (see the right part of Figure 2.9). The ideal structure of perovskite, which is illustrated in Figure 2.9, is a cubic lattice [14].

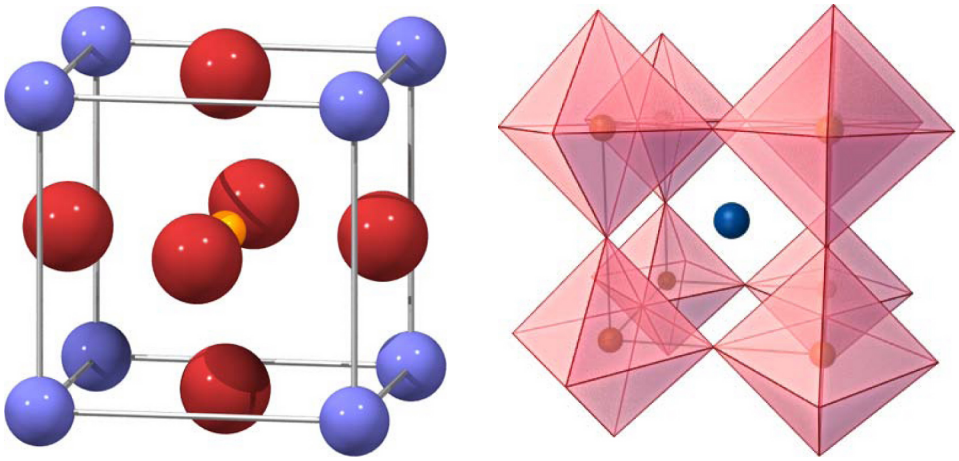

Figure 2.9: The "ideal" structure of perovskite, a cubic lattice. (left) Unit cell with B in the center, (right) same structure with A in the center and the BO_6 octahedra in red [32].

2.3 Spray pyrolysis

Solution processes can yield fine and intimately mixed precursor powders. In this way, the repeated milling and calcination steps common to conventional solid state processes are eliminated, reducing the powder contamination and processing time [52]. Spray pyrolysis is such a technique, and utilizes a solution-based precursor being fed into a rotating furnace through a nozzle. In the hot-zone, the atomized solution is dried and the constituent metal salts decompose and form an intimate metal oxide mixture. The spray pyrolysed powders are collected in a cyclone. Through spray pyrolysis chemically homogeneous and high purity ceramic powder can be synthesized. Oxide powders with homogeneous particle sizes and crystallite sizes less than 100 nm may be produced by this method. A schematic diagram of the apparatus is shown in Figure 2.10.

Unlike many other techniques, spray pyrolysis represents a very simple and relatively cost-effective processing method (especially with regard to equipment costs). The method has been employed for the deposition of dense films, porous films, and for powder production [31]. Spray pyrolysis has been used for several decades in the glass industry [47] and in solar cell production [48].

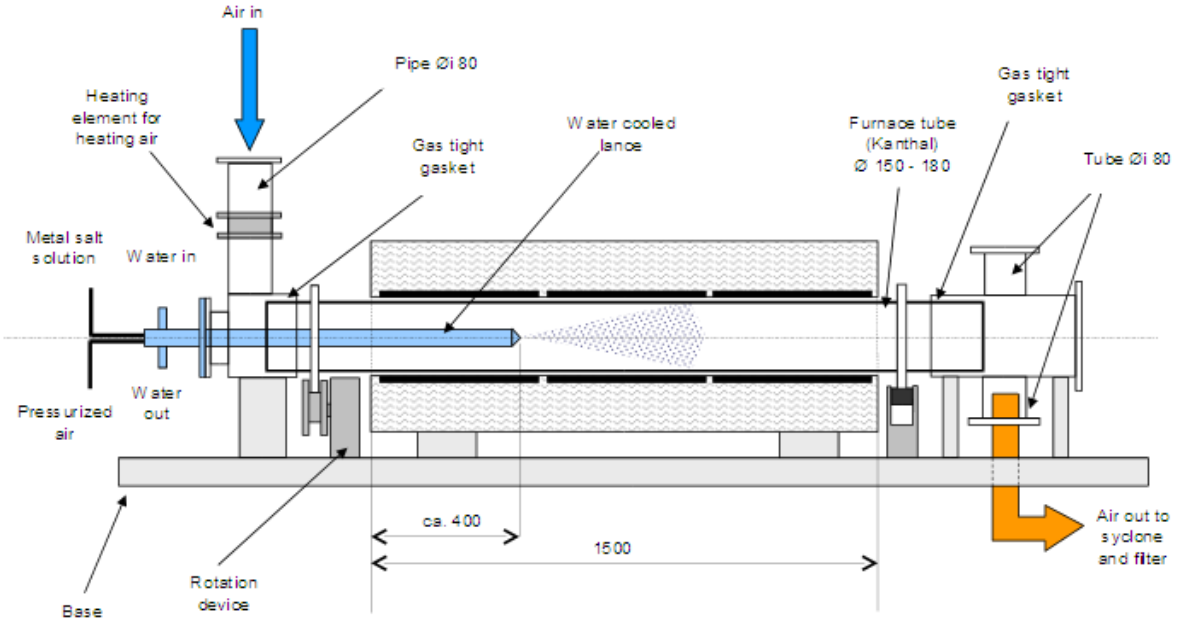

Figure 2.10: Schematic diagram of a spray pyrolysis apparatus. Image courtesy of SINTEF Senior Scientist Ove Paulsen.

2.4 Sintering

The densification of a ceramic compact is technically referred to as *sintering*. It is used as a method for making objects from powder, by heating the material in a sintering furnace. What happens during sintering is essentially that the pores between the starting particles are removed by mechanisms of mass transfer, and adjacent particles grow together and form strong bonds (the atoms diffuse through the microstructure). During the sintering process, it is essential to avoid coarsening and promote densification. Choosing a suitable sintering temperature is important in this aspect, as different temperature intervals will give rise to different coarsening and/or densification mechanisms [16]. The sintering parameters will affect the final density of the material, as well as the microstructure. It is well-known that microstructure plays a significant role toward the observed piezoelectric properties [17]. Therefore, it is of great importance to optimize the sintering process to achieve the desired properties. The sintering process is dependent on temperature, duration, particle size, green body density, atmosphere and pressure. Changing these parameters will thus affect the final properties.

3 Litterature review

3.1 Compositional and microstructural inhomogenity

Several authors have found that significant compositional inhomogeneity exists in Li- and Ta-modified KNN ceramics [20, 23, 54]. These inhomogenities appear more pronounced when the material has been synthesized by directly mixing alkali carbonates and Ta and Nb oxides, and Wang et al. found that they could not be eliminated by prolonged high-temperature annealing. These compositional inhomogenities lead to inferior ferro- and piezoelectric properties [23].

There is an opposite effect between adding lithium and tantalum as dopants to KNN. Lithium promotes grain growth and the development of an inhomogeneous grain size distribution, while tantalum is known to inhibit grain growth and produce materials with a narrow grain size distribution [56, 57].

3.2 Sintering

The effect of sintering condition on the microstructure of LKNNT-based ceramics has been investigated in prior studies [19-28]. The common conclusion in these studies is that this system is difficult to sinter due to:

1. Volatility of alkali elements.
2. Hygroscopic nature of alkaline carbonates.
3. Formation of secondary phases.

Hollenstein reported that 96% density of $K_{0.485}Na_{0.485}Li_{0.03}Nb_{0.8}Ta_{0.2}O_3$ was achieved by sintering in air at 1136 °C for 60 minutes [36]. Wang et al. have reported that they have achieved >95% density of $K_{0.48}Na_{0.48}Li_{0.04}Nb_{0.8}Ta_{0.2}O_3$, by sintering in air at 1145 °C for 60 minutes, through the use of a "reversed crucible method", where the material is sealed during sintering to cause a partial pressure build-up of alkali vapor, which acts as a inhibitor against their vaporization [20]. Li et al. reported densities exceeding 95% for $K_{0.44}Na_{0.52}Li_{0.04}Nb_{0.85}Ta_{0.15}O_3$ by sintering in air at 1120 °C for 2 hours, also using the reversed crucible method. Li et al. also reported that Ta doping seemed to shift the optimal sintering point to a higher temperature [27]. In that aspect it is also interesting to notice that Kim et al. found the optimim sintering point for $K_{0.475}Na_{0.475}Li_{0.05}Nb_{0.95}Ta_{0.05}O_3$ to be only 1000 °C.

Madaro found, for undoped KNN, that sintering in pure O_2 atmosphere avoided volatilization of alkali oxides during sintering [8]. Zhen et al. found that there is a narrow processing window for the sintering densification without drastic volatilization, and that the piezoelectric

properties are not only affected by density but are also sensitive to the degree of volatilization, as this leads to a change of composition [46].

López et al. reported obtaining high densities for $(K_{0.48}Na_{0.52})_{0.96}\,Li_{0.04}Nb_{0.85}Ta_{0.15}O_3$ sintered in air at 1120 °C for 2 hours [53].

3.3 Piezoelectric properties of $K_{0.485}Na_{0.485}Li_{0.03}Nb_{0.8}Ta_{0.2}O_3$

Saito et al. have reported synthesis of $K_{0.485}Na_{0.485}Li_{0.03}Nb_{0.8}Ta_{0.2}O_3$ with an electric-field-induced strain comparable to typical actuator-grade PZT [1]. They anticipated the formation of a tetragonal-orthorhombic MPB in the perovskite-rich region by the dissolution of a small amount of a pseudo-ilmenite-structured material, causing a *lattice distortion* for the structural phase transition. The need for stable piezoelectric characteristics over a wide temperature range made them choose high Curie-temperature ($T_C \geq 250°C$) end members: orthorhombic perovskite-type $K_{0.5}Na_{0.5}NbO_3$ ($T_C = 415°C$) and hexagonal pseudo-ilmenite-type $LiTaO_3$ ($T_C = 615°C$). The highest piezoelectric charge sensor constant d_{33} was reported to be 230 $\frac{pm}{V}$ with a Curie temperature of 323 °C. Saito et al. also reported producing textured polycrystals of the alkaline niobate-based composition, enhancing the d_{33} constant to 373 $\frac{pm}{V}$. The Curie temperature was reported to be controllable between 170 and 500 °C in the compositional range, such that additions of Li and Ta elements actually *shifted the Curie temperature* higher and lower, respectively [1].

Wang et al. reported a d_{33} of 200 $\frac{pm}{V}$, after annealing the material at 1145 °C for 25 hours and poling it under 30 $\frac{kV}{cm}$ at 90 °C for 30 min [20]. Hollenstein reported a d_{33} of 310 $\frac{pm}{V}$, after poling the material under 50 $\frac{kV}{cm}$ at 50 °C for 30 min [36]. Both Wang et al. and Hollenstein used conventional solid-state reaction method to form the ceramics.

4 Experimental procedure

4.1 Apparatus/Chemicals

Lists of chemicals and apparatus used in the experimental procedure is listed in Table 4.1 and 4.2, respectively.

Table 4.1: List of chemicals used in the experimental procedure, in order of appearance.

Chemical	Purity	Name	Origin
$(NH_4)NbO(C_2O_4)_2{\cdot}5H_2O$		NAmOx	H.C. Starck, Goslar, Germany
Tantalum Oxalate solution		TamOx	H.C. Starck, Goslar, Germany
KNO_3	$\geq$ 99.0 %	KNO_3, pro analysi	Merck KGaA, Darmstadt, Germany
$NaNO_3$	$\geq$ 99.0 %	$NaNO_3$, pro analysi	Merck KGaA, Darmstadt, Germany
$LiNO_3$	$\geq$ 99.0 %	$LiNO_3$, reagent plus	Sigma-Aldrich, St. Louis, USA
Isopropanol	99,9 %	2-propanol	VWR, West Chester, PA, USA
Epoxy		EpoFix Resin	Struers A/S, Ballerup, Denmark
Epoxy hardener		EpoFix Hardener	Struers A/S, Ballerup, Denmark
Diamond solution, 9 µm		DiaPro Plan	Struers A/S, Ballerup, Denmark
Diamond solution, 4 µm		DiaPro Dur	Struers A/S, Ballerup, Denmark
Diamond solution, 1 µm		DiaPro Nap	Struers A/S, Ballerup, Denmark
Chloroform	99,2%	AnalaR Normapur	VWR, West Chester, PA, USA
Silicone oil		DC 704	Dow Corning, Midland, USA

Table 4.2: List of apparatus used in the experimental procedure, in order of appearance.

Apparatus	Name	Origin
Drying oven	TS 8024	Termaks, Bergen, Norway
S(T)EM	S-5500	Hitachi, Tokyo, Japan
Planetary mill	PM 100	Retsch, Haan, Germany
Scanning electron microscopy	S-3400N	Hitachi, Tokyo, Japan
Hydraulic press	C-press	Calfinn Ltd., Engadine, Australia
Balance	AG204 DeltaRange	Mettler-Toledo, Columbus, Ohio, USA
Caliper	Digimatic 500-301	Mitutoyo Corporation, Kanagawa, Japan
Furnace	L 3/12/P330	Nabertherm GmbH, Lilienthal, Germany
Hand polisher	LaboPol-21	Struers A/S, Ballerup, Denmark
Polisher	TegraForce-5	Struers A/S, Ballerup, Denmark
Energy-Dispersive X-ray Spectroscopy	EDS Model 7021	Oxford Instruments, Oxfordshire, UK
Sputter Coater	S150B	Edwards, Crawley, West Sussex, UK
High dc voltage generator	Model 609E-6	Trek, Tokyo, Japan
Dielectric test module	TF Analyzer 2000	aixACCT Systems, Aachen, Germany

4.2 Procedure

A flowchart describing the experimental procedure is shown in Figure 4.1.

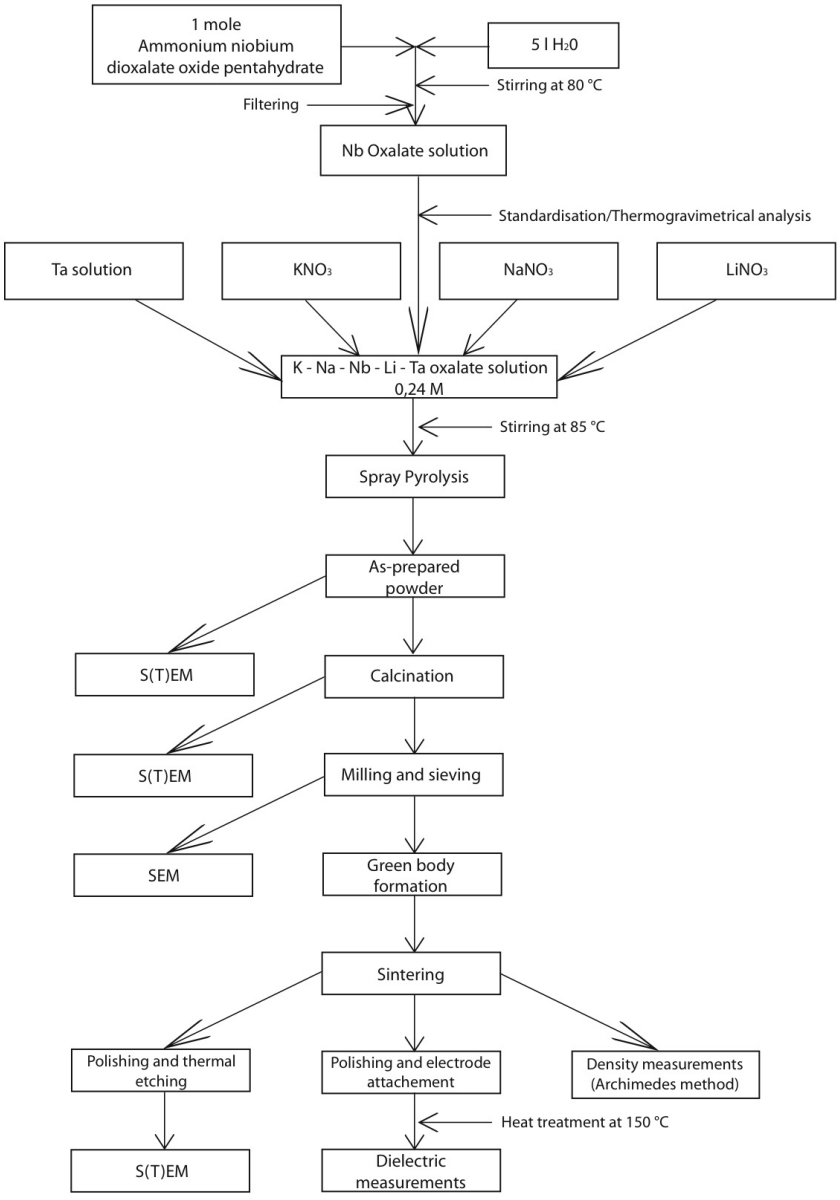

Figure 4.1: Flowchart of the experimental procedure.

4.2.1 Synthesis of precursor solution

Ammonium niobium dioxalate oxide pentahydrate, $(NH_4)NbO(C_2O_4)_2{\cdot}5H_2O$ (1 mole) was dissolved in 5 liters of distilled water, and heated to 80 °C, and then cooled to room temperature before filtering. The Nb-concentration in the solution was measured by thermogravimetrical analysis, which is based on the weight of the residual Nb_2O_5 after heat treatment of a small amount of the solution at 700°C. The solution was further mixed with stoichiometric amounts of tantalum oxalate solution. KNO_3, $NaNO_3$ and $LiNO_3$, pre-dried at 169 °C for 18 hours (TS 8024, Termaks, Bergen, Norway) in order to remove any moisture, was also added. This solution was stirred for 3 hours at 85 °C to obtain 0.24 M Nb-K-Na-Li-Ta oxalate solution, referred to from now on as a precursor solution [51].

4.2.2 Spray pyrolysis

The precursor solution was held at a temperature of 80-90 °C and stirred while being fed into the spray pyrolysis apparatus, due to signs of turbidity when precursor was cooled to room temperature. The precursor was atomized at a rate of $1.5\frac{l}{h}$ by a two-phase nozzle (diameter 1 mm) with internal mixing of liquid and 150 kPa pressurized air, directly into a furnace at 1000 °C via a lance in the spray pyrolysis apparatus (see Figure 2.10). The lance temperature of the furnace during synthesis was 855 - 862 °C [51]. Estimated range of droplet size is 20–40 μm. Residence time calculated from the air flow through the system is 0,4 s [33].

4.2.3 Powder preparation and pellet formation

A calcination step was performed in order to decompose the residual traces of nitrates, oxalates and carbonates in the as-prepared powder. A suitable calcination treatment has earlier been found to be 600 °C for 6 hours, with a heating rate of 200 $\frac{^\circ C}{hour}$ [51]. The microstructures of the as-prepared powder and the calcined powder were investigated using scanning electron microscopy (S(T)EM, S-5500, Hitachi, Tokyo, Japan).

The calcined powder was milled (Planetary mill, PM 100, Retsch, Haan, Germany) to increase the tap density/remove aggregates, and then sieved at 250 µm. Different milling methodologies were attempted. The different milling approaches used are summarized in Table 4.3. To estimate which milling parameters to use, an analytical approach was made (see Appendix C).

For the dry planetary milling at 155 RPM, it was decided to attempt to increase the milling efficiency and homogenity by increasing the amount of powder being milled at a time, from 1.35 g to 5.35 g, as well as stopping the planetary mill every 15 minutes to loosen the powder (technically referred to as 6 x 15 min-milling). The microstructures of

the as-prepared powder and the calcined powder were investigated using scanning electron microscopy (SEM, S-3400N, Hitachi, Tokyo, Japan).

Table 4.3: List of milling approaches used. All powders were calcined at 600 °C prior to milling.

Milling method	Milling container	Milling liquid	Milling medium	Rotation speed, RPM	Powder amount, g	Duration, min
Planetary dry milling	ZrO_2, 125 ml	N/A	ZrO_2, #24, 10mmØ	100	1.35	150
Planetary dry milling	ZrO_2, 125 ml	N/A	ZrO_2, #24, 10mmØ	155	1.35-5.35	14-120
Planetary dry milling	ZrO_2, 125 ml	N/A	ZrO_2, #24, 10mmØ	200	1.35	30
Planetary dry milling	ZrO_2, 125 ml	N/A	ZrO_2, #24, 10mmØ	300	1.35	10-14
Planetary dry milling	ZrO_2, 125 ml	N/A	ZrO_2, #24, 10mmØ	600	1.35	10-20
Planetary wet milling	ZrO_2, 125 ml	100% ethanol	ZrO_2, #24, 10mmØ	300	1.35	32
Planetary wet milling	ZrO_2, 125 ml	100% ethanol	ZrO_2, #24, 10mmØ	500	1.35	240
Planetary wet milling	ZrO_2, 125 ml	100% ethanol	ZrO_2, #24, 10mmØ	600	1,35	165
Wet ball milling	Plastic bottle, 500 ml	100% ethanol	ZrO_2, #121, 5mmØ	70	20	26 hours

Disk-shaped pellets with thicknesses of 1 mm, radii of 5 mm and weighing 0.2 gram, made of powders milled using the milling setups shown in Table 4.3 and sieved at 250 µm, were uniaxially pressed (C-press hydraulic press, Calfinn Ltd., Engadine, Australia) at 150 MPa, as this pressure is found to be optimal with respect to defect-free as well as high density green bodies [34]. The green body densities were measured using a balance (AG204 Deltarange, Mettler-Toledo, Columbus, Ohio, USA) and a caliper (Digimatic 500-301, Mitutoyo Corporation, Kanagawa, Japan).

4.2.4 Sintering

The disk-shaped pellets were sintered in air without binder, inside an alumina crucible and on a powder bed, and three different sintering setups were attempted. The sintering parameters used in the different approaches are summarized in Table 4.5. When using the direct insertion or immediate descent method, the sintering furnace was pre-heated to the given temperature, and the pellet was then placed inside to maximize the heating rate (see Section 6.2).

The first approach used was *conventional sintering*, where the pellet was placed inside the furnace at room temperature and exposed to a heating, holding and cooling step (see Figure 4.2). The second approach used was to insert the pellet at an elevated temperature, maintain the given temperature for a given time, and then remove the pellet while the furnace was still at elevated temperature (see Figure 4.3), from now on referred to as *direct insertion*. In the third approach, the pellet was inserted at an elevated temperature, and the temperature was set to decrease at the moment the pellet was inserted (see Figure 4.4), from now on referred to as *immediate descent*. In all the sintering approaches, the reversed-crucible method was used to prevent the volatilization of the alkali metal elements [20]. The temperatures reported was adjusted from the furnace set points through a calibration scheme, in order to reflect the actual temperature (see Appendix A).

Table 4.5: List of sintering parameters used in each of the sintering setups.

Sintering setup	Heating rate	Sintering temperature range	Hold time, min	Cooling rate
Conventional sintering	$10\frac{^{\circ}C}{min}$	1151-1166 °C	1	$4\ \frac{^{\circ}C}{min}$
Direct insertion	$>1000\frac{^{\circ}C}{min}$	870-1162 °C	60	$>1000\frac{^{\circ}C}{min}$
Immediate descent	$>1000\frac{^{\circ}C}{min}$	1152-1166 °C	0	$4{,}5\ \frac{^{\circ}C}{min}$

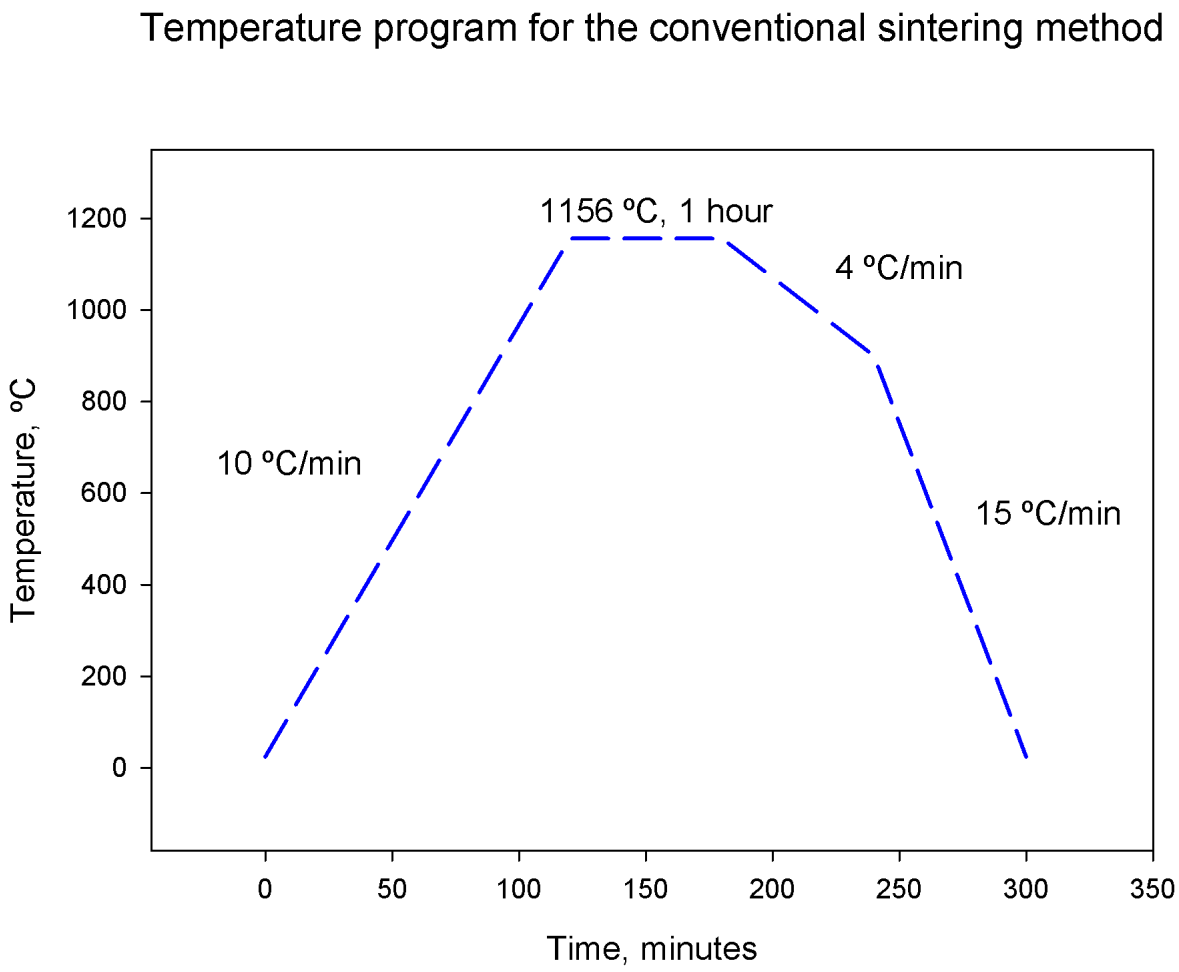

Figure 4.2: Temperature program for the conventional sintering method (using 1156 °C as an example of the sintering point). Since the heating and cooling steps are relatively slow, it was assumed that the temperature of the samples did not deviate significantly from the graph at any point. It should be noted that the heating rate represents an average heating rate, and the real heating rate is larger at the beginning and slower as the temperature approaches the set point.

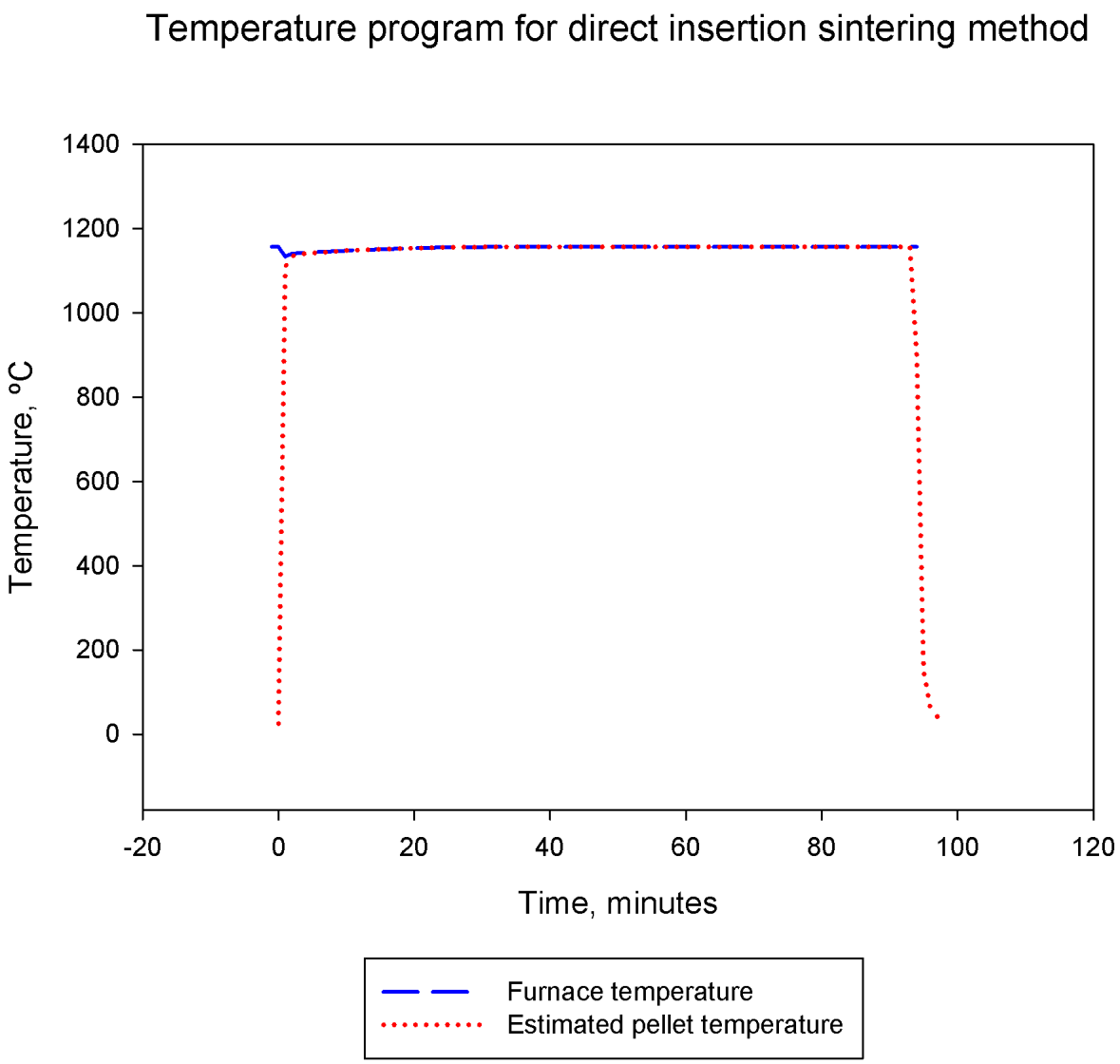

Figure 4.3: Temperature program for the direct insertion sintering method (using 1145 °C as an example of the sintering point). Since the heating and cooling steps are very rapid, it was assumed that the temperature of the samples needed some time to reach the temperature of its surroundings. Note the small drop and subsequent increase in temperature in the early minutes, this is due to opening the furnace door and inserting the sample, a process taking approximately 8 seconds. The furnace usually spends 20-30 minutes to reach the set temperature after the sample has been inserted.

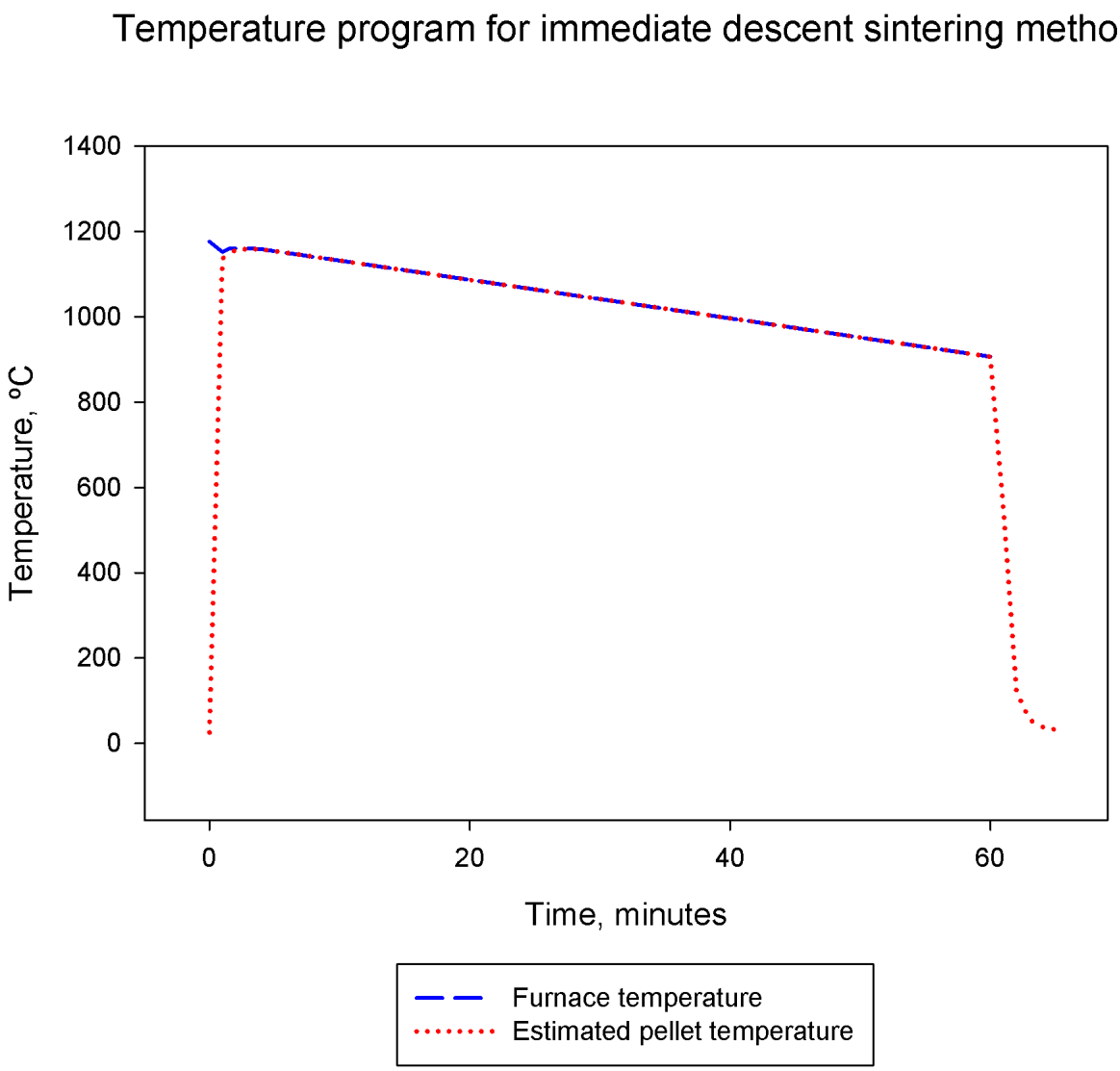

Figure 4.4: Temperature program for the immediate descent sintering method, the temperature starting at 1170 °C and spending 60 minutes to descend to 900 °C. Since the heating and cooling steps are very rapid, it was assumed that the temperature of the samples needed some time to reach the temperature of its surroundings. Note the small drop and subsequent increase in temperature in the early minutes, this is due to opening the furnace door and inserting the sample, a process taking approximately 8 seconds.

4.2.5 Sample characterisation

The final densities of the sintered samples were measured by Archimedes' method using 2-propanol.

Some of the sintered samples were cast in epoxy, and polished by hand using 220-grit and 1000-grit waterproof SiC-paper (LaboPol-21, Struers A/S, Ballerup, Denmark), followed by a three-step automated polishing process using a water based solution containing diamonds of sizes 9 µm , 4 µm and 1 µm, respectively (TegraForce-5, Struers A/S, Ballerup, Denmark). Most of the remaining epoxy was then removed from the sample by grinding using 80-grit waterproof SiC paper, followed by 24 hours of soaking in chloroform. See Figure 4.5 for a complete overview of the processing steps involved. The polished samples were thermally etched in air at 1050 ^{o}C for 30 minutes before investigation. The microstructures of the sintered samples were investigated along the polished surfaces using a S(T)EM (S-5500, Hitachi, Tokyo, Japan). The backscattered electron mode (BSE) and energy-dispersive X-ray spectroscopy (EDS, Model 7021, Oxford Instruments, Abingdon, Oxfordshire, UK) were also used on the polished surfaces to investigate the degree of compositional homogenity (S-3400N, Hitachi, Tokyo, Japan), using an acceleration voltage of 20 kV, and a vacuum of 25 Pa.

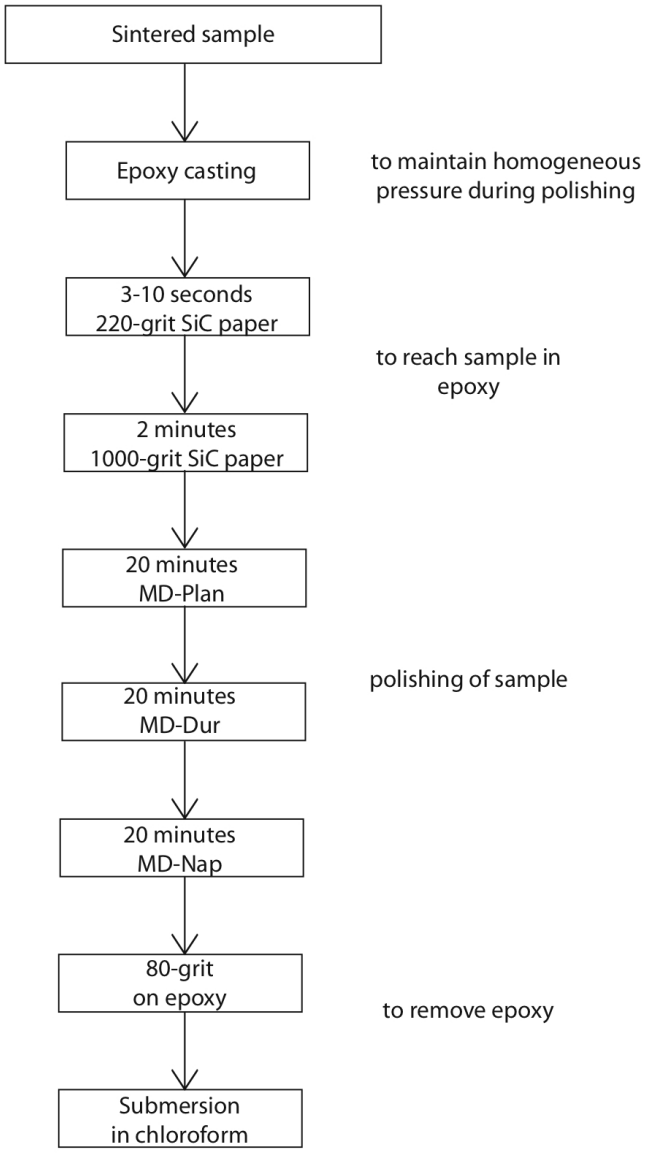

Figure 4.5: The procedure used when polishing sintered samples in order to investigate the microstructure.

4.2.6 Investigation of dielectric properties

Selected sintered samples were polished using 1000-grit SiC paper, to obtain a desired thickness and surface smoothness. The electrodes were formed at the sample surfaces by gold sputtering for 10 minutes on each side applying 20 mA (S150B, Edwards, Crawley, West Sussex, UK), followed by heat treatment for 30 minutes at 155 ^{o}C (TS 8024, Termaks, Bergen, Norway) to remove any moisture. During transfer from the furnace to the dielectric test module, the samples were kept in a dessicator with silica gel, to minimize moisture exposure. The samples were poled under a 4 $\frac{kV}{mm}$ bias, using a high dc voltage generator (Model 609E-6, Trek, Tokyo, Japan) at 100 ^{o}C in an oil bath for 10 minutes. The electric field was maintained during cooling to 61 ^{o}C. See Table 4.6 for a list of the samples investigated and their relevant parameters.

Table 4.6: List of sintered samples investigated for their dielectric properties.

Sintering method	Density	Initial thickness	Thickness after polishing	Poling field
Conventional sintering	92,3 %	2,44 mm	0,76 mm	4 $\frac{kV}{mm}$
Direct insertion	90,6 %	2,51 mm	0,84 mm	4 $\frac{kV}{mm}$
Immediate descent	96,1 %	0,83 mm	0,74 mm	4 $\frac{kV}{mm}$

The ferroelectric and piezoelectric measurements were performed using a dielectric test module (TF Analyzer 2000, aixACCT Systems, Aachen, Germany). All measurements were performed applying a triangular electric field at a frequency of 0.25 - 1 Hz, and an electric field of 1 - 2 $\frac{kV}{mm}$. To estimate E_C and P_r, a bipolar triangular electric field was applied before poling, at room temperature. To estimate d^*_{33} before and after poling, a unipolar triangular electric field was applied, at room temperature (see Section 2.1.3). To study the effect of aging after poling, a unipolar electric field was applied to the sample sintered using the conventional method, each hour for 24 hours after poling. It was also attempted to expose the materials to short bursts of electric fields in the range of 3-4 $\frac{kV}{mm}$, in order to study whether it had any poling effect compared to the poling procedure described above.

To study the temperature effect on d^*_{33}, the samples were heated after poling and aging, from room temperature to 120 ^{o}C while the d^*_{33} was measured every 4-5 ^{o}C using an electric field of 1.5 $\frac{kV}{mm}$ and a frequency of 1 Hz.

5 Results

5.1 Powder morphology

5.1.1 As-prepared and calcined powder

S(T)EM images of the as-prepared powder and powders calcined for 6 hours at 600 °C, all unmilled, are presented in Figure 5.1. The particles appear to take the shape of hollow spheres. It seems like there is little visible difference in the powder morphology before and after calcination, except that the spheres appear to be more battered and punctured after the calcination.

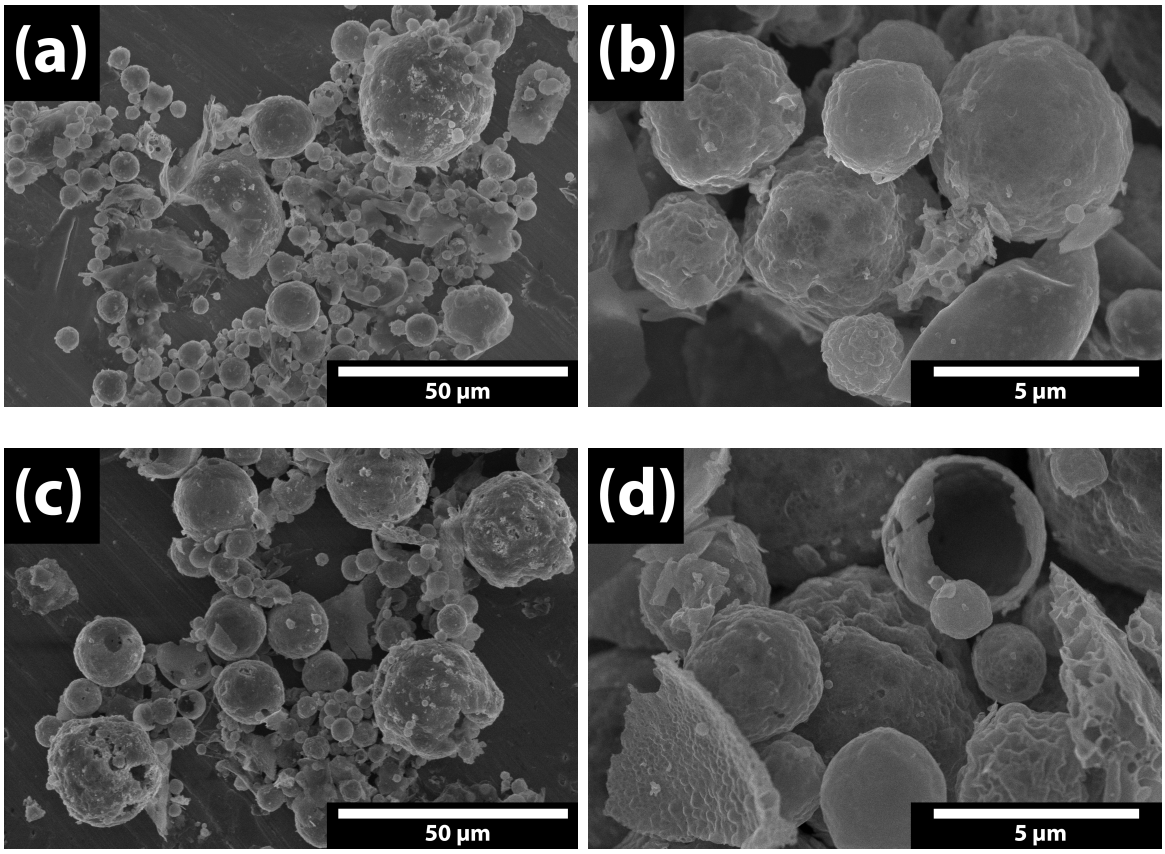

Figure 5.1: S(T)EM images of (a, b) as-prepared powder and (c, d) powder calcined for 6 hours at 600 °C [51].

5.1.2 Planetary dry milling

SEM images of powders planetary dry milled at 100 RPM, 155 RPM, 200 RPM, 300 RPM and 600 RPM are shown in Figure 5.2, 5.3, 5.4, 5.5 and 5.6, respectively. In some cases, unwanted flakes or sphere remnants were found in the powder. See Figure 5.7 for an overview of these findings.

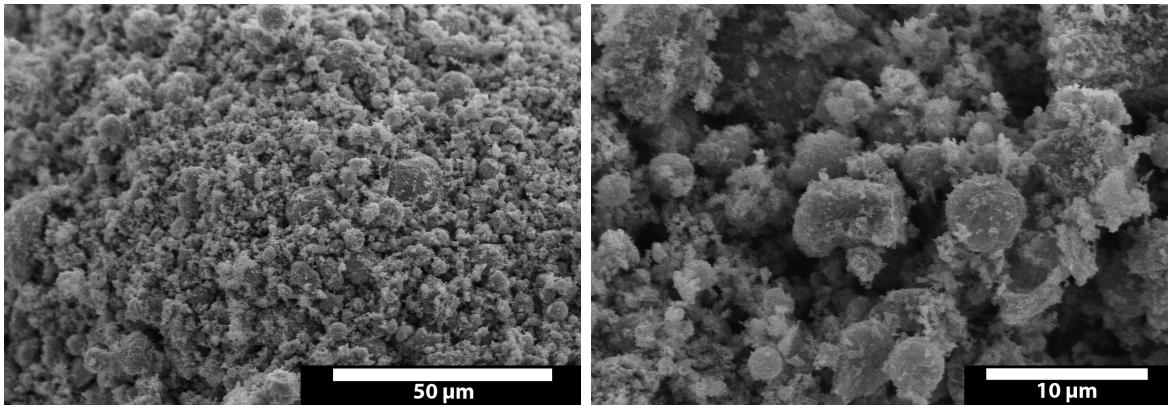

Figure 5.2: SEM images of powder planetary dry milled at 100 RPM for 150 minutes. Several remnants of the initial shells are visible.

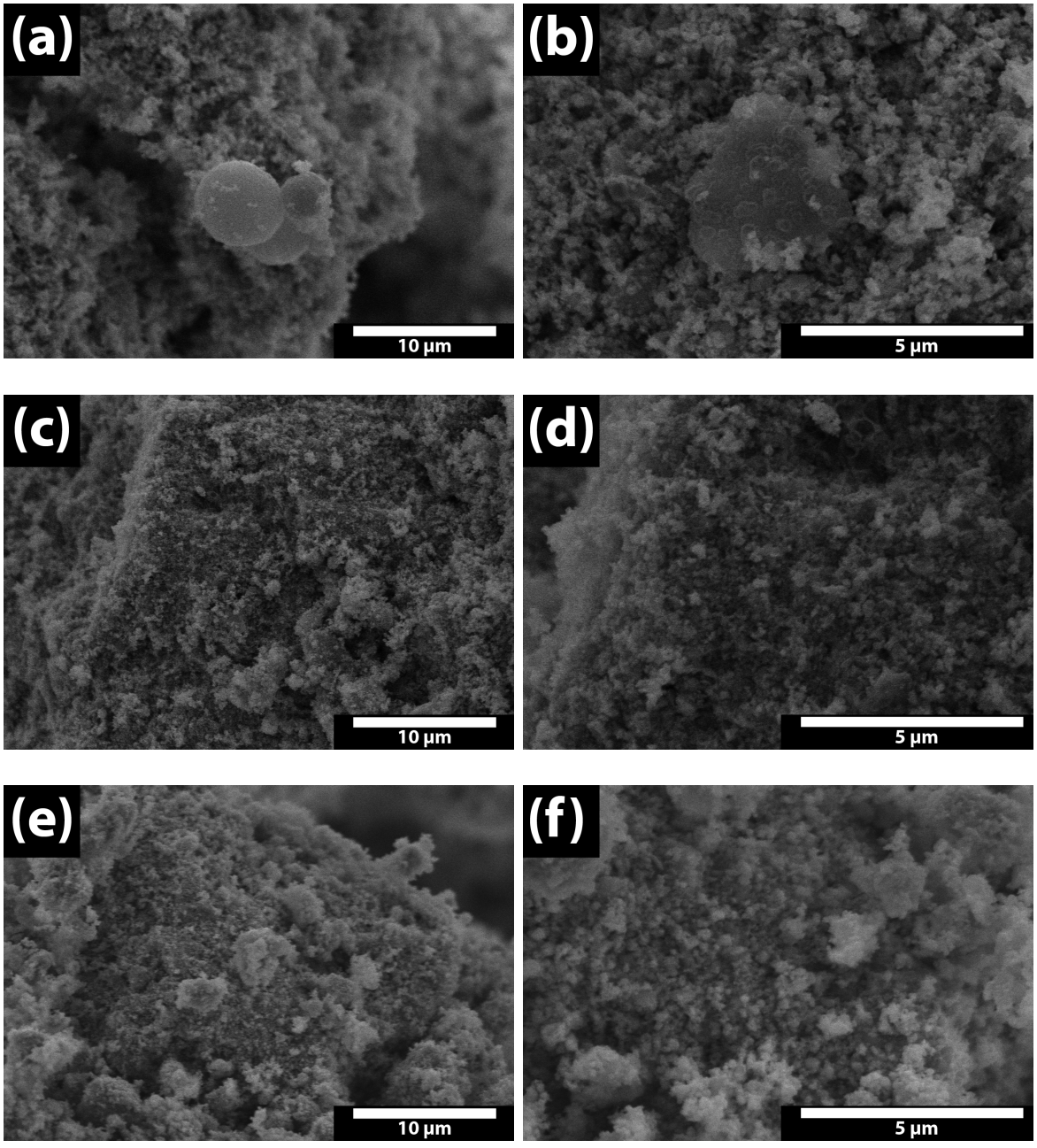
(a)
10 µm
(b)
5 µm
(c)
10 µm
(d)
5 µm
(e)
10 µm
(f)
5 µm

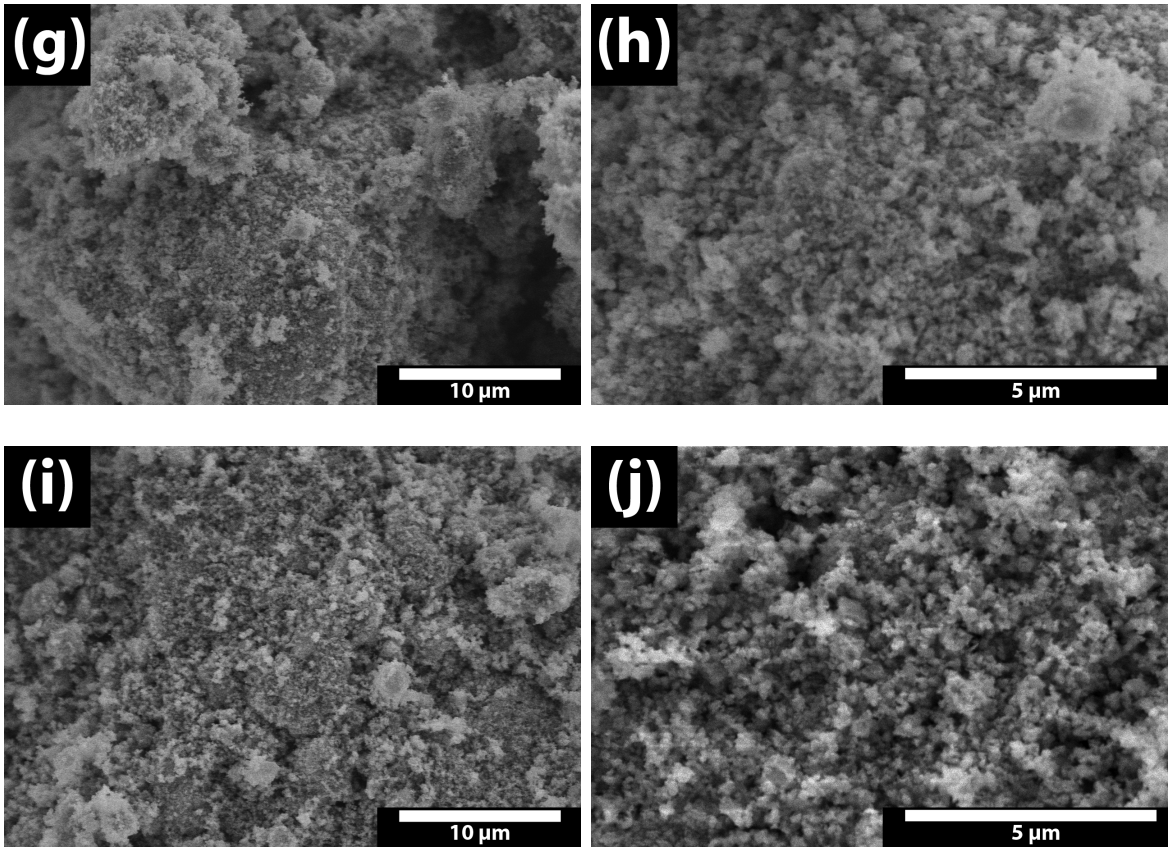

Figure 5.3: SEM images of powders planetary dry milled at 155 RPM (1,35 g batches) for (a, b) 14 minutes, (c, d) 17 minutes, (e, f) 120 minutes, and (5,35 g batches) for (g, h) 120 minutes and (i, j) 6 x 15 minutes.

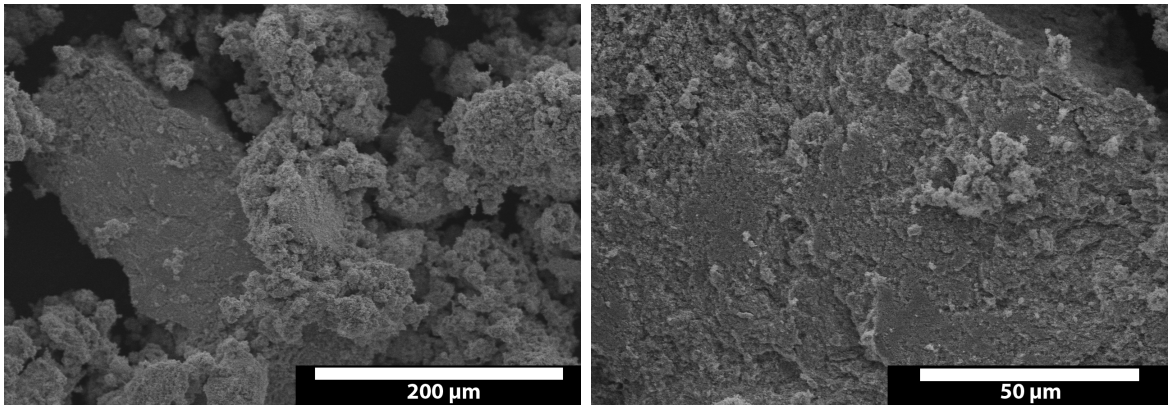

Figure 5.4: SEM images of powder planetary dry milled at 200 RPM for 30 minutes.

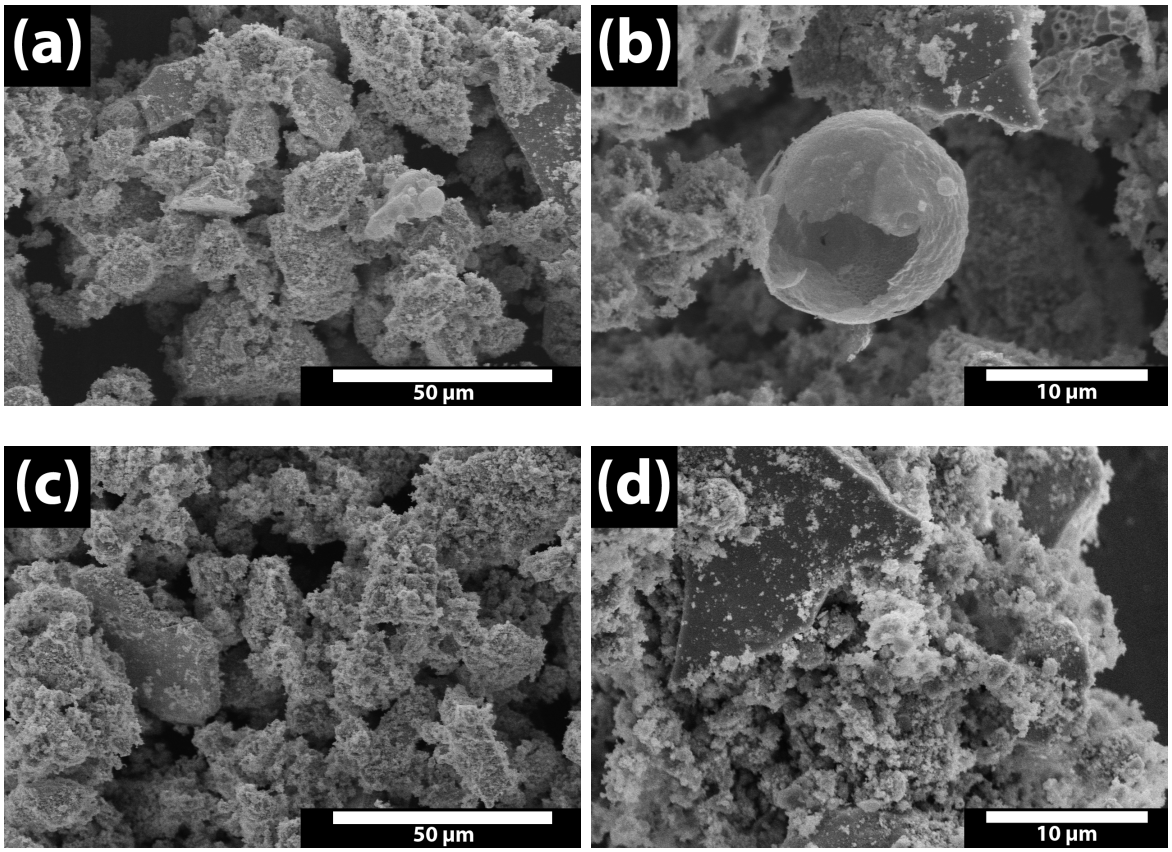

Figure 5.5: SEM images of powder planetary dry milled at 300 RPM for (a, b) 10 and (c, d) 14 minutes.

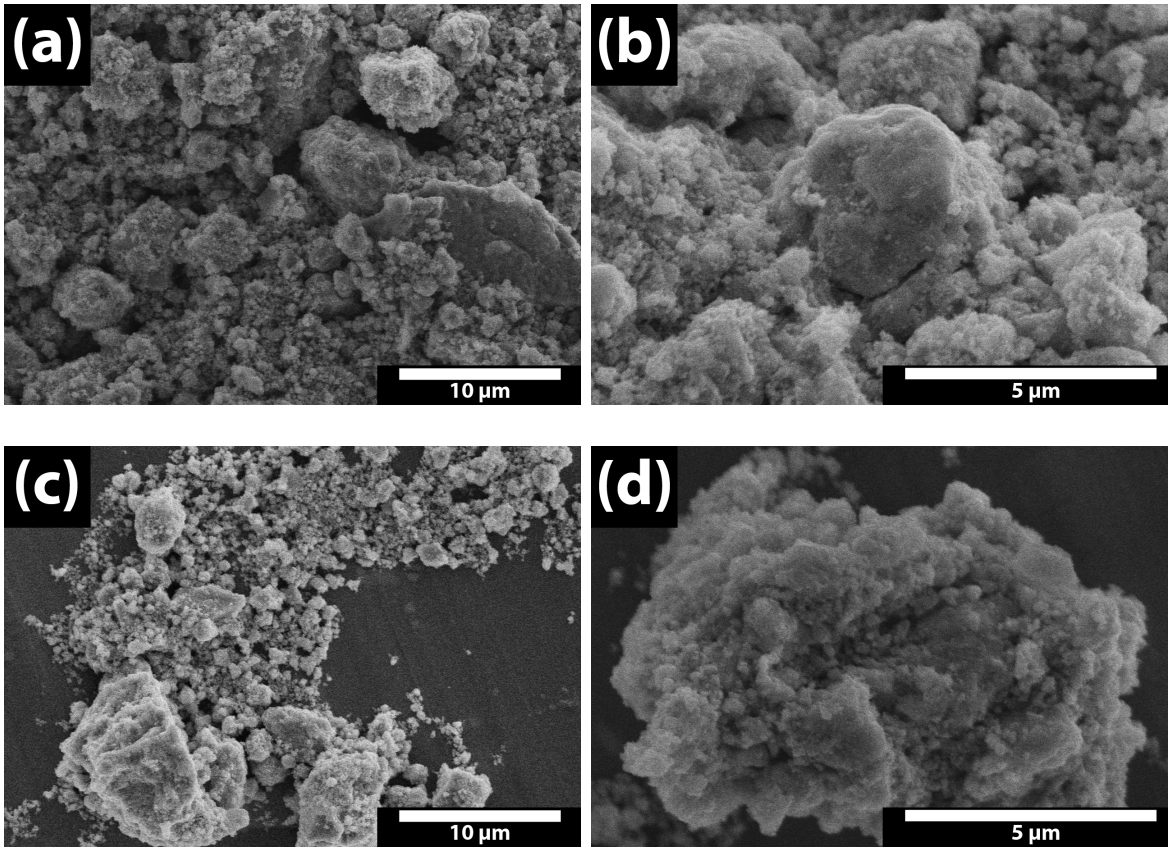

Figure 5.6: SEM images of powder planetary dry milled at 600 RPM for (a, b) 10 and (c, d) 20 minutes.

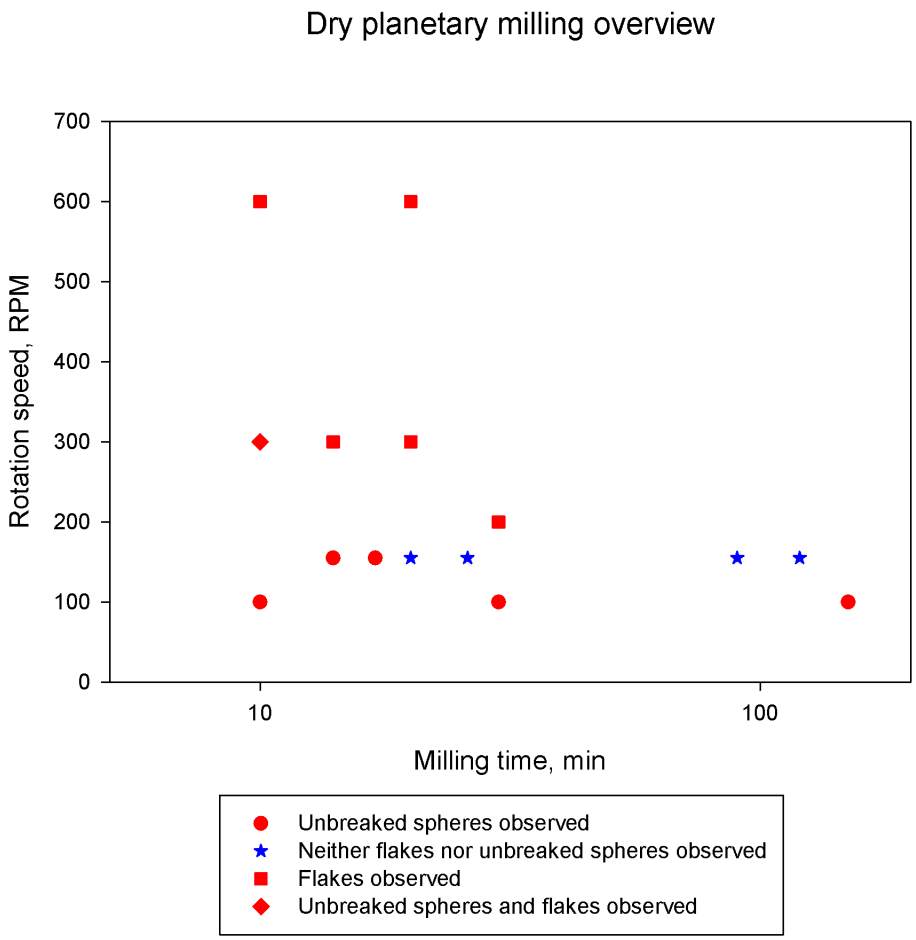

Figure 5.7: Overview of the different planetary dry milling conditions attempted, and whether the milling treatment resulted in insufficient sphere breakdown and/or unwanted flakes in the powder.

5.1.3 Planetary wet milling

SEM images of the planetary wet milled powder are displayed in Figure 5.8. In all cases, unwanted flakes and/or sphere remnants were found in the powder after milling, even after relatively long milling times. See Figure 5.9 for an overview of these findings.

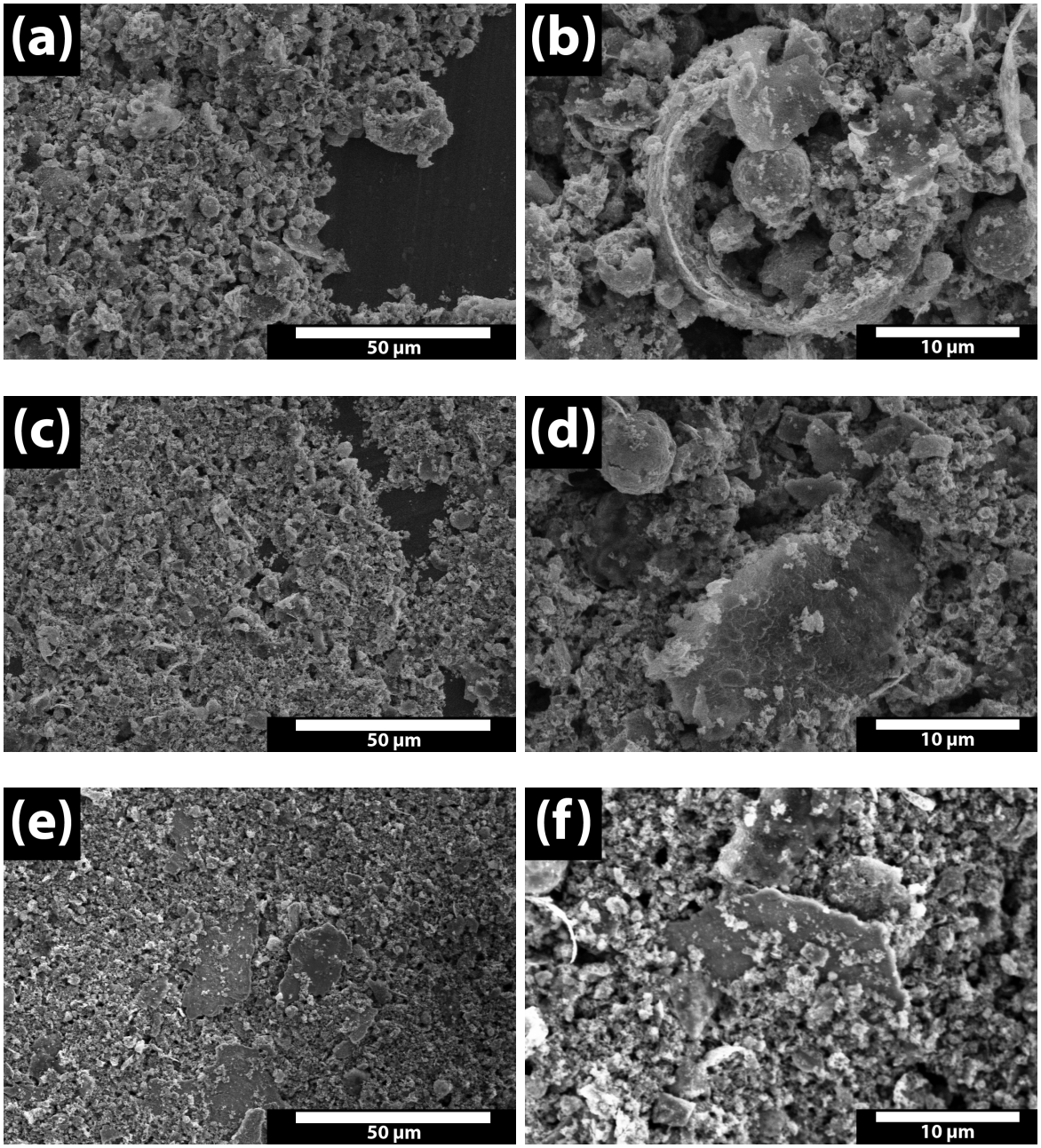

Figure 5.8: SEM images of (a, b) 300 RPM (32 minutes), (c, d) 500 RPM (240 minutes) and (e, f) 600 RPM (165 minutes) planetary wet milled powders.

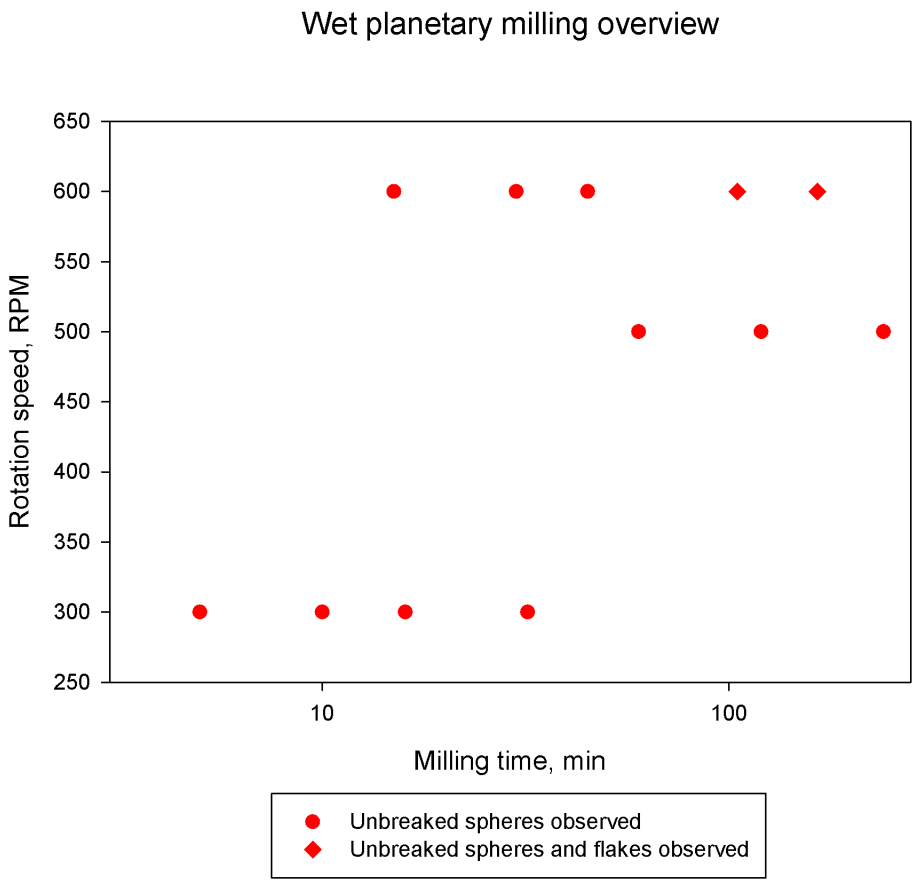

Figure 5.9: Overview of the different planetary wet milling conditions attempted, and whether the milling treatment resulted in insufficient sphere breakdown and/or unwanted flakes in the powder.

5.1.4 Ball milling

SEM images of the ball milled powder are displayed in Figure 5.10. There appears to be sphere remnants in the powder.

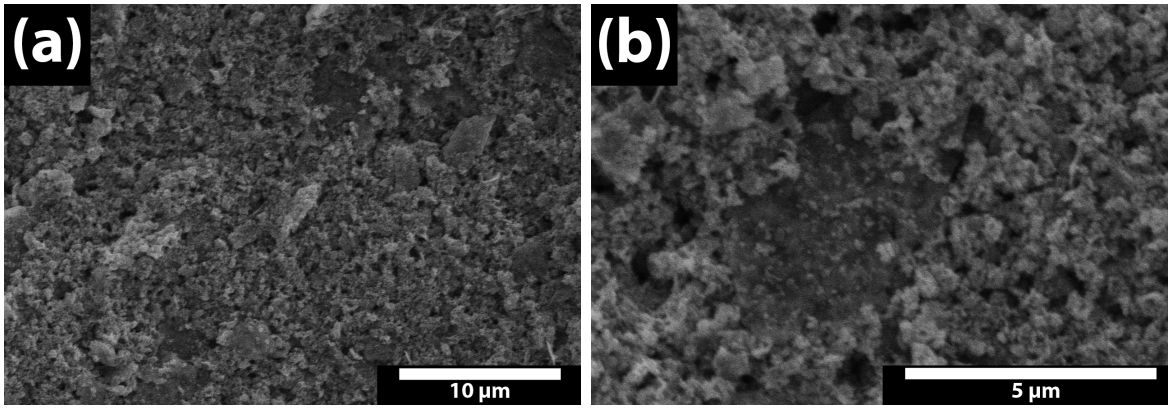

Figure 5.10: SEM images of powder ball milled for 26 hours.

5.2 Density measurements

5.2.1 Green bodies

The green body densities of the samples pressed with respect to the milling procedure used are displayed in Figure 5.11. The difficulty of achieving sufficient agglomerate break down through wet milling is visible, and a non-monotonic relationship between degree of milling treatment and green body density is evident.

Depending on the milling procedure, the green body density would attain a different degree of reproducibility. Figure 5.12 depicts a histogram showing the distribution of green body densities for two variations of the dry planetary milling at 155 RPM; 120 minutes of the milling without intervention, and 90 minutes of milling where the powder was physically loosened from the container every 15 minutes. In the latter case, the green body densities achieved from sample to sample seemed to be much more narrowly distributed, with a *lower* average density than the former case.

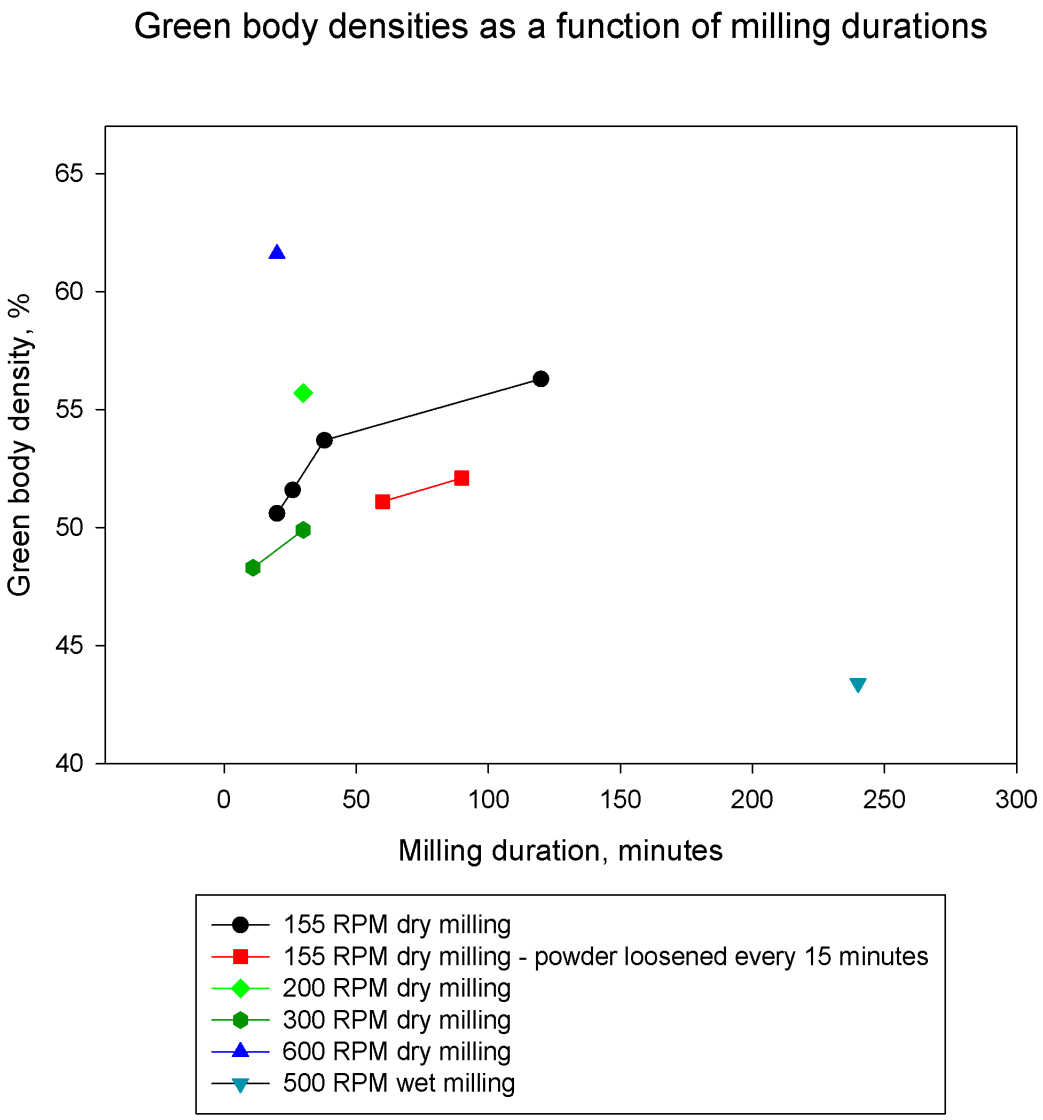

Figure 5.11: Average green body densities as a function of milling durations.

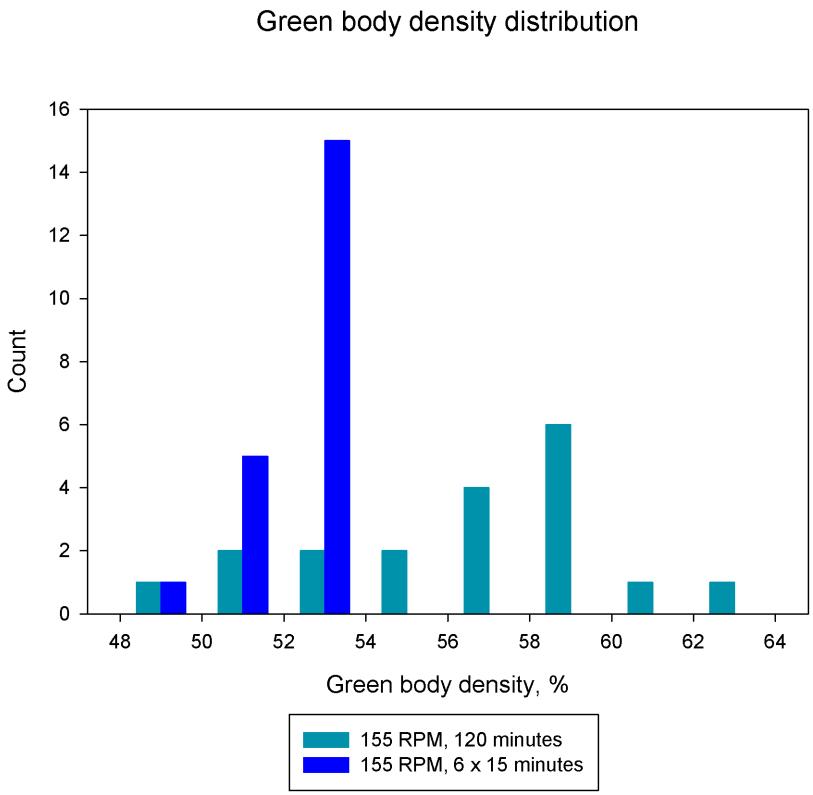

Figure 5.12: Distribution of the green body densities using 155 RPM dry planetary milling, with and without intermediate steps of loosening powder from the milling container.

5.2.2 Sintered bodies

The crystallographic density has earlier been found by standard XRD software (Diffracplus Topas, Bruker AXS, Billerica, Massachusetts, USA) to be 4.99 $\frac{g}{cm^3}$ (see Table 5.1), verified by Hollenstein et al. [22, 51].

Table 5.1: Lattice parameters and estimated crystallographic density for LKNNT [51].

a (Å)	b (Å)	c (Å)	Spacegroup	Density
3.9500	5.6288	5.6527	Amm2	4.9899

For an overview of the densities and porosities achieved using different milling setups, see Figure 5.13 (see Appendix B for a larger overview). The most successful sintering was carried

out using larger powder batches of 5.35 g, milled for 6 x 15 minutes (see Section 4.2.3). The sintering parameters found to be optimal for each sintering method (and therefore used for the samples investigated through dielectric measurements) are summarized in Table 5.2.

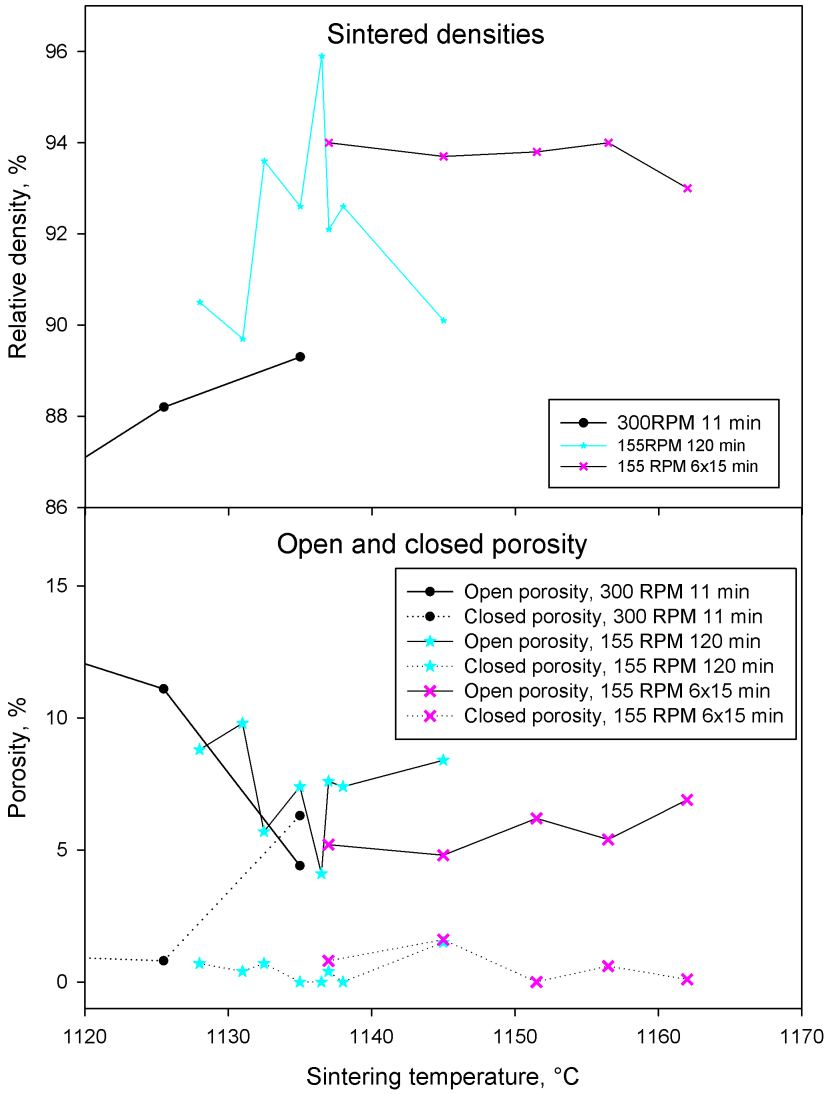

Figure 5.13: Final densities after sintering for 1 hour by direct insertion, measured by Archimedes' method. The reversed crucible method was used, and the samples were inserted into a pre-heated furnace to ensure a high heating rate. After 1 hour they were quenched in air.

Table 5.2: Sintering parameters found to be optimal for each sintering method, and thus used to make samples for dielectric characterisation.

Sintering method	Total duration	Temperature
Conventional	300 minutes	1156 °C
Direct insertion	90 minutes	1156 °C
Immediate descent	60 minutes	1164 °C (and descending)

Conventional sintering The final densities of the samples sintered conventionally, using powder milled at 155 RPM for 6 x 15 minutes, are shown in Figure 5.14. When sintering using this setup (see Figure 4.2), densities of more than 94% is achieved using a sintering temperature of 1156 °C, which repeatedly produces the highest densities. Mostly the porosity in the LKNNT ceramics sintered this way consists of open porosity, in some cases the closed porosity was dominant when sintering around 1156 °C.

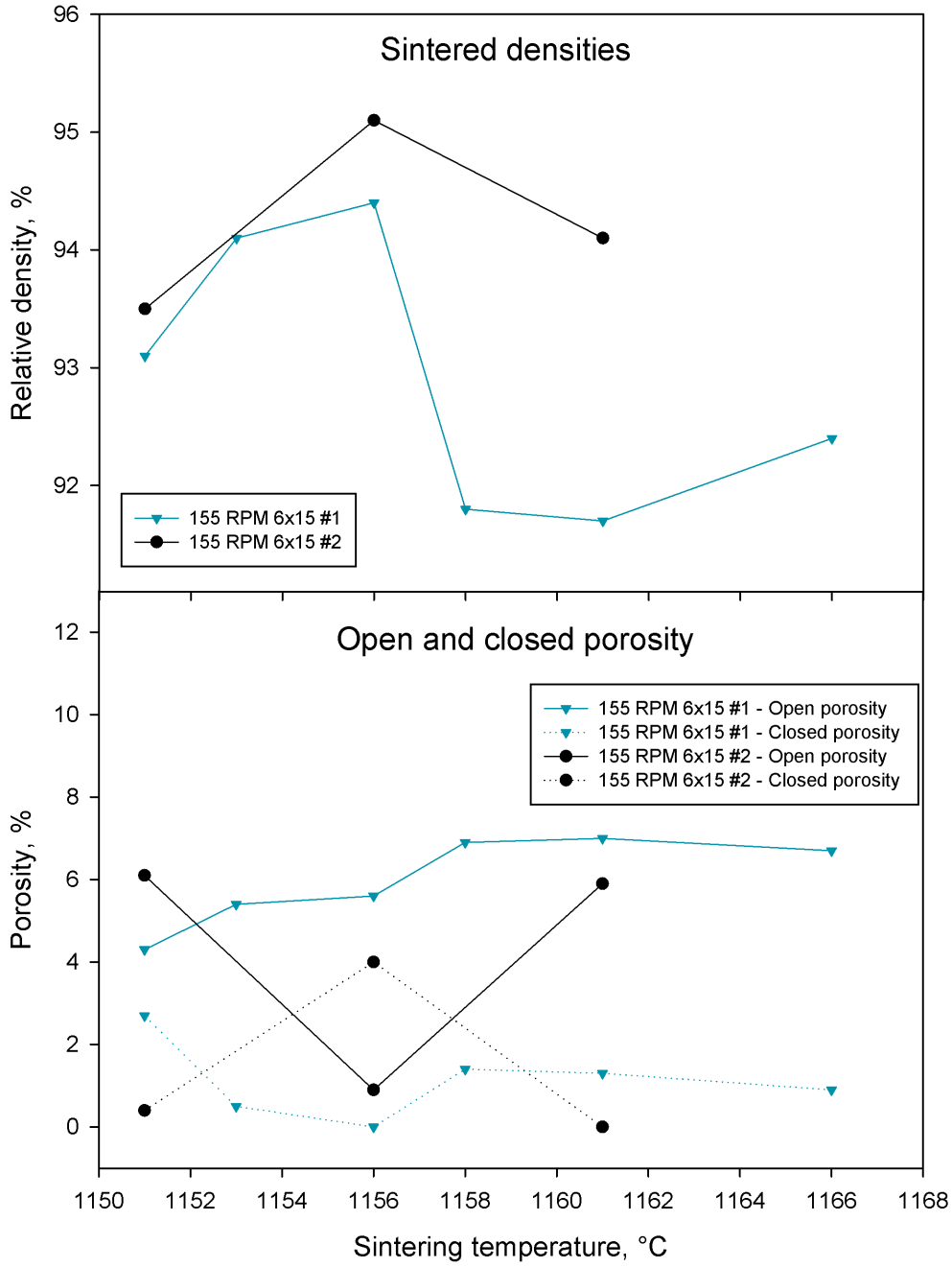

Figure 5.14: Final densities after conventional sintering for 1 minute, measured by Archimedes' method. The powder used was milled at 155 RPM for 6 x 15 minutes. The reversed crucible method was used.

Direct insertion The final densities of the samples sintered in the pre-heated furnace are shown in Figure 5.15. When sintering using this setup (see Figure 4.3), the final density seems to be more robust with respect to sintering temperature, attaining a density of around 94% when sintered in the temperature range of 1145-1156 °C. Mostly the porosity in the LKNNT ceramics sintered this way consists of open porosity. The achieved densities, optimum sintering temperature, as well as distribution of closed and open porosity appear to coincide with the respective parameters for the conventional sintering method.

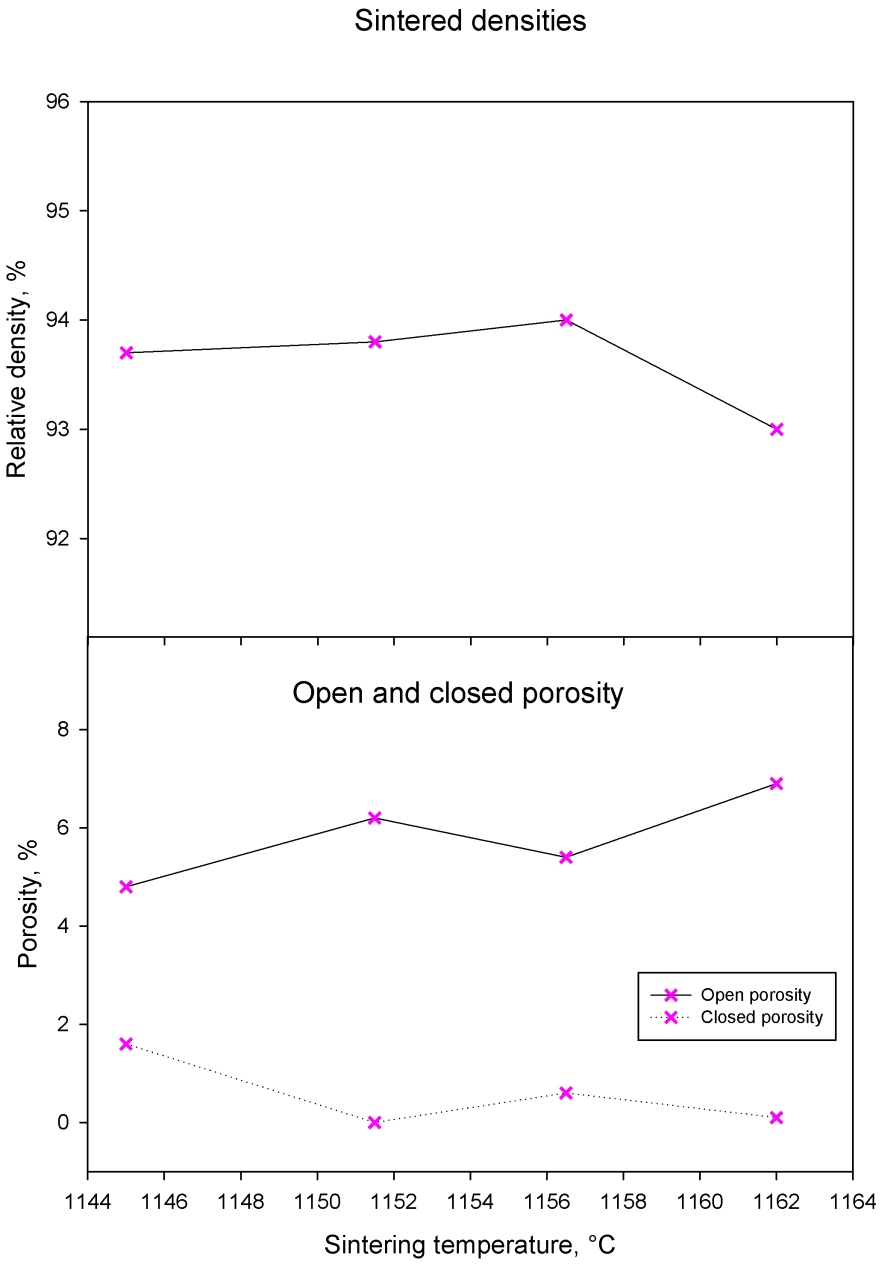

Figure 5.15: Final densities after sintering for 1 hour by direct insertion, measured by Archimedes' method. The reversed crucible method was used, and the samples were inserted into a pre-heated furnace to ensure a high heating rate. After 1 hour they were quenched in air. The powder used was milled at 155 RPM for 6 x 15 minutes.

Immediate descent The final densities of the samples sintered in a pre-heated furnace and letting the temperature drop immediately after insertion, with respect to the starting temperature, are shown in Figure 5.16. When sintering using this setup (see Figure 4.4), the final density arrives at 95-97 %. The sintered density seems to be relatively robust with respect to the *initial* temperature, with an optimum temperature range of more than 10 °C (1155-1165 °C). The vast majority of porosity in the LKNNT ceramics sintered this way consists of closed porosity. In order to check wheter the entire cooling step was needed, it was attempted to start (using powder milled for 120 minutes using 155 RPM) at 1158 °C and abort the procedure at 1111 °C, well below the sintering temperature range chosen for all other samples sintered conventionally or by direct insertion. This resulted in a final density of 85.1 %, much lower than what is achieved for the rest of the samples sintered using the immediate descent method.

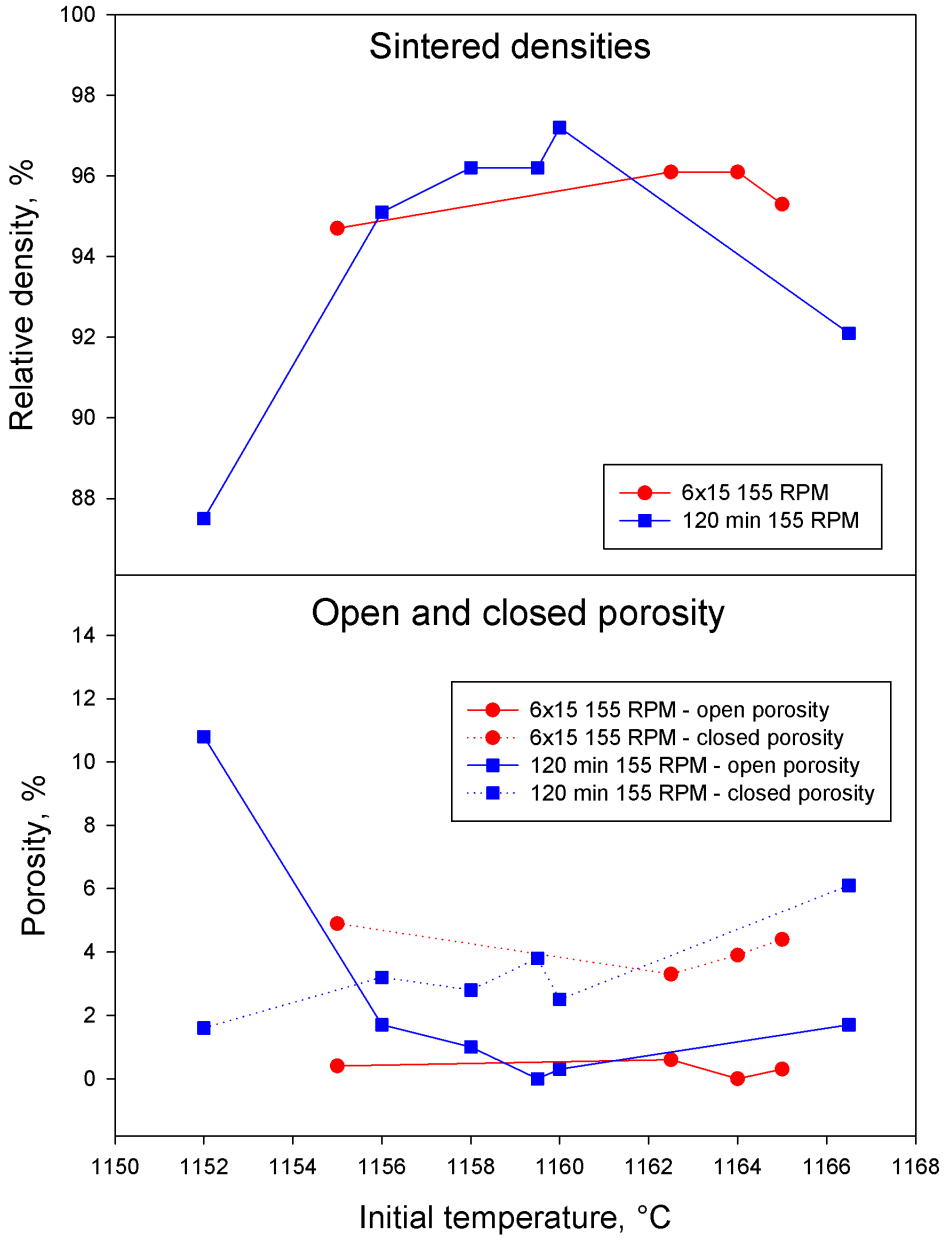

Figure 5.16: Final densities after sintering for 1 hour by immediate descent, measured by Archimedes' method. The reversed crucible method was used, and the samples were inserted into a pre-heated furnace to ensure a high heating rate. After 1 hour they were quenched in air. The powders used were milled at 155 RPM for either 6 x 15 or 120 minutes. The temperature reported refers to the initial temperature.

5.3 Microstructure

SEM images of samples sintered using the conditions found to be optimal for each sintering technique, are shown in the Figures below.

The linear intercept method was used to estimate the mean grain size of the different samples. These results are summarized in Table 5.3.

Table 5.3: Estimates of mean grain size for the different sintering methods, using linear interecept. Around 250 grains were used in the measurement, for each sintering method.

Sintering method	Mean grain size, µm	Standard deviation, µm
Conventional	2,37	1,12
Direct insertion	1,72	0,21
Immediate descent	1,50	0,25

5.3.1 Conventional sintering

SEM images of samples sintered for 1 hour at 1156 °C using the conventional method (see Section 4.2.4), and polished using the setup described in Section 4.2.5 are shown in Figure 5.17. The grain size distribution seems to be relatively broad, with some grains smaller than 1 µm and others having a size exceeding 5 µm, in accordance with the mean grain size and standard deviation estimated in Table 5.3.

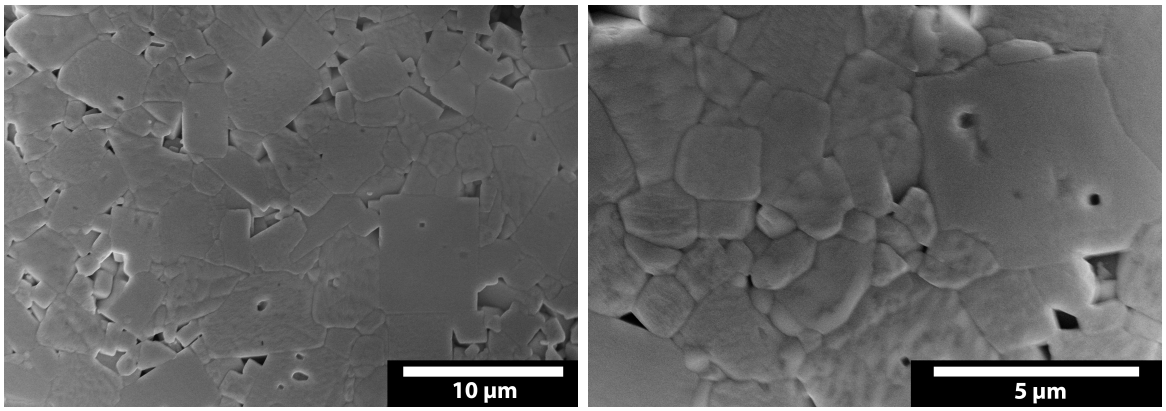

Figure 5.17: SEM images of a polished surface of a sample sintered for 1 hour at 1156 °C, using the conventional method. The reversed crucible method was used.

5.3.2 Direct insertion

SEM images of samples sintered by direct insertion into a hot furnace at 1156 °C for 1 hour (see Section 4.2.4), and polished using the setup described in Section 4.2.5 are shown in Figure 5.18. The grain size distribution appears to be more narrow than in the conventional case, with more "medium-sized" grains of sizes 2-3 µm present.

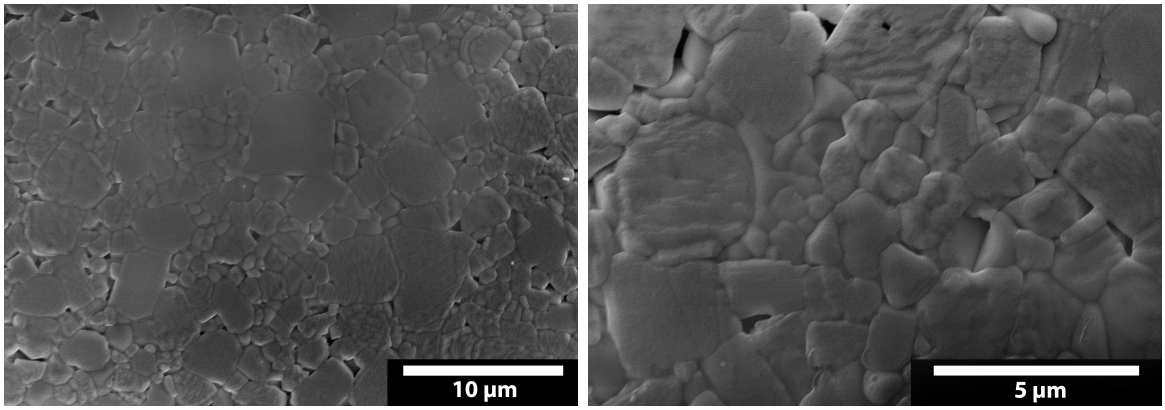

Figure 5.18: SEM images of a polished surface of a sample sintered for 1 hour at 1156 °C, using the direct insertion method. The reversed crucible method was used. After 1 hour it was quenched in air.

5.3.3 Immediate descent

SEM images of samples sintered using the immediate descent method (see Section 4.2.4), and polished using the setup described in Section 4.2.5 are shown in Figure 5.19. Little porosity is visible, and the grain size distribution appears to be more narrow than when using the two other sintering methods, with no grains exceeding 4 µm.

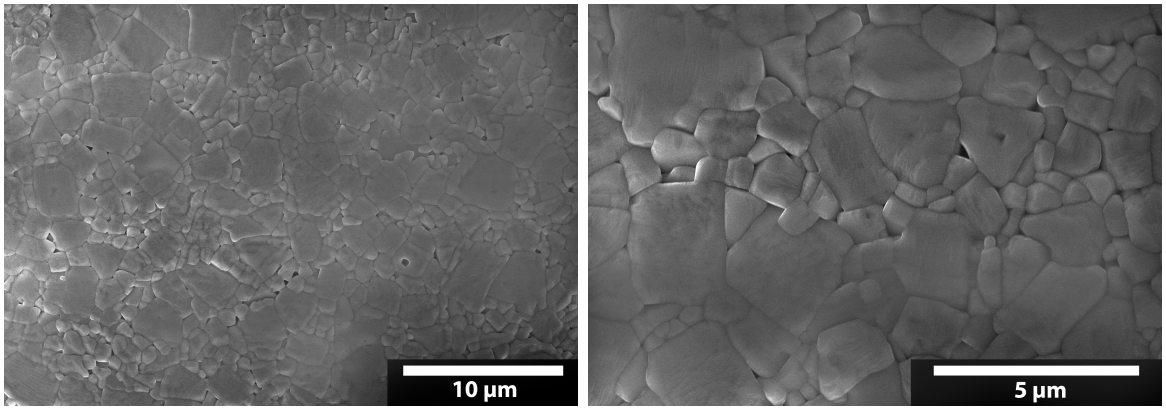

Figure 5.19: SEM images of a polished surface of a sample sintered using the immediate descent method. The reversed crucible method was used.

5.3.4 Compositional homogenity

BSE images with different selected areas and their corresponding EDS spectra are shown in Figure 5.20. EDS average elemental composition for all the sintering methods are shown in Table 5.4. EDS element maps showing the spatial distribution of elements are shown in Appendix D.

What appears to be melting phases are visible in Figure 5.20, and were observed to cover approximately 0,2 % of the polished surfaces. EDS average elemental compositions of these are shown in Figure 5.21. The only difference in atomic mass percent between the melting phase and the other grains is a smaller amount of sodium, which has been reduced to about 3 % (regardless of sintering method).

Apart from these melting phases, the material seems to possess a high degree of compositional homogenity, with elemental content close to what is expected.

Table 5.4: Expected atomic mass percent based on stoichiometry, and EDS estimates. Li content could not be estimated due to its low atomic number.

Element	Expected (atomic %)	Conventional sintering	Direct insertion	Immediate descent
K	9,7 %	9,1%	9,1%	9,3%
Na	9,7 %	8,7%	8,6%	9,1%
Li	0,6 %	N/A	N/A	N/A
Nb	16,0 %	16,1%	16,2%	16,4%
Ta	4,0 %	4,2%	4,4%	4,2%
O	60,0 %	61,9%	61,7%	61,0%

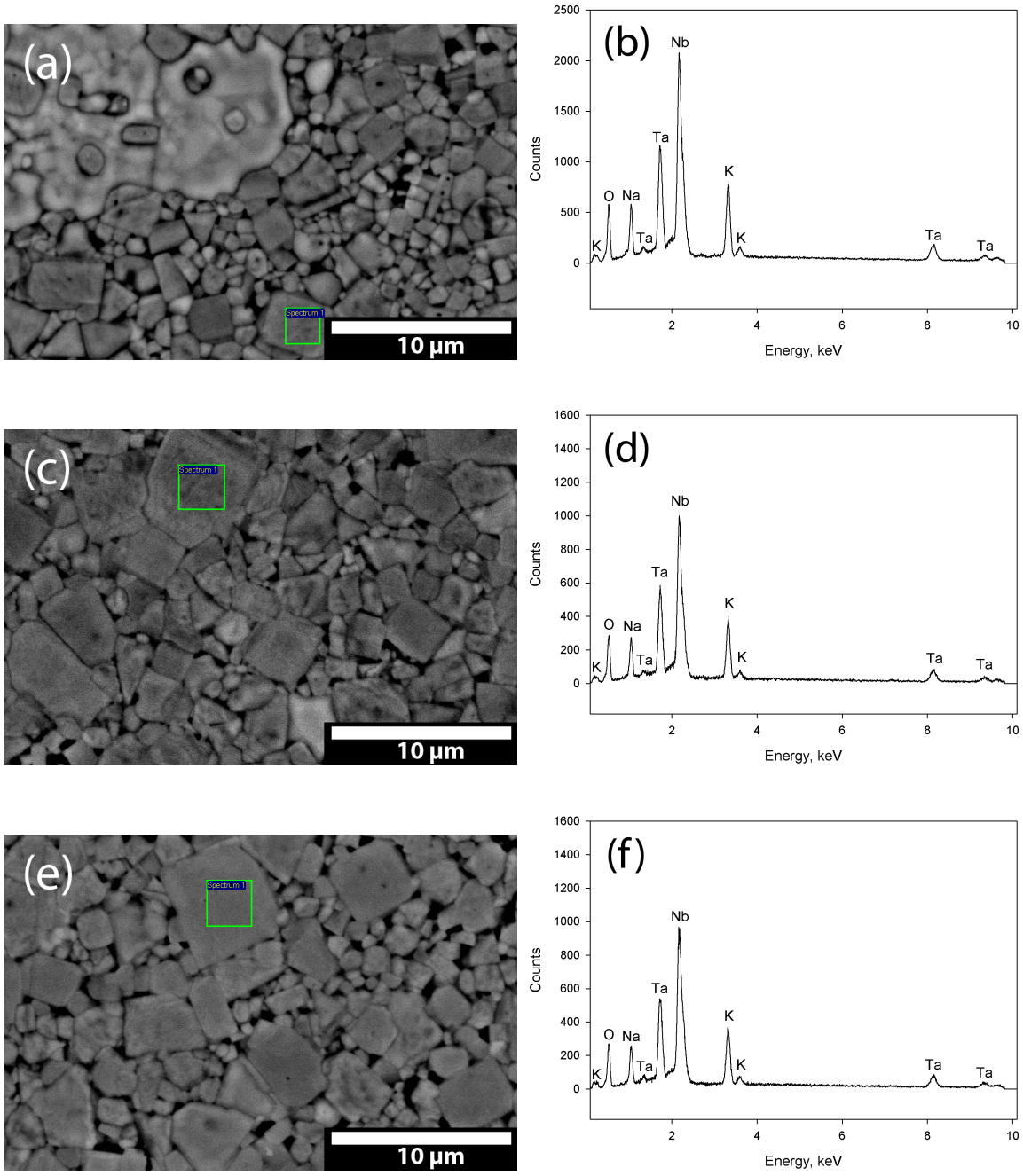

Figure 5.20: BSE images of a polished surface of a sample sintered using the (a) immediate descent method, (c) conventional method and (e) direct insertion method, and (b, d, f) their corresponding EDS spectrum based on the average over the depicted area. Very similar spectra and compositions were found in other grains.

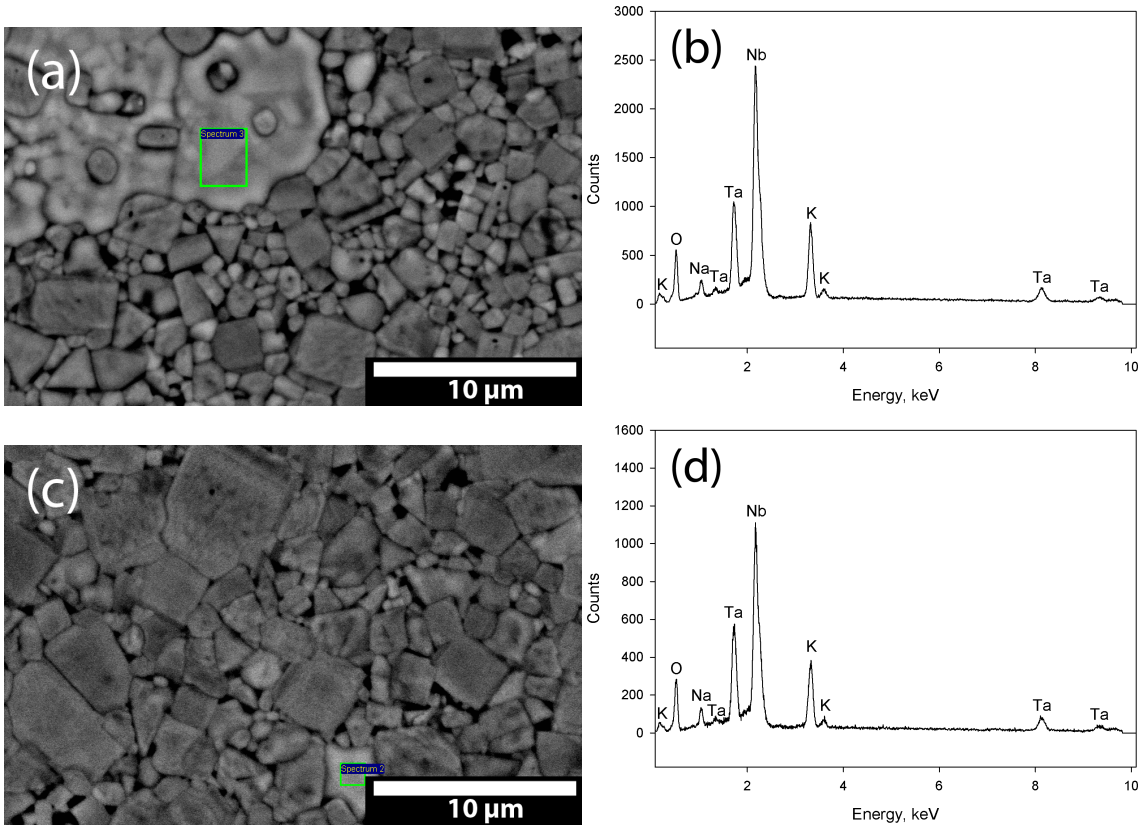

Figure 5.21: BSE images of a polished surface of a sample sintered using the (a) immediate descent method and (c) the conventional method, and (b, d) the corresponding EDS spectrum taken of the melting phases, based on the average over the depicted area.

5.4 Dielectric measurements

5.4.1 Polarization and displacement measurements

The *bipolar* polarization- and displacement-electric field hysteresis loops of the samples sintered using the conditions found to be optimal for each sintering technique (see Section 4.2.4), and the corresponding I-V curves, are shown in Figure 5.22. The switching effect is clearly observed in all the samples, with some variations in the dielectric parameters depending on the sintering technique being used. The switching effect is also visible for all the samples when measuring using a lower electric field (see Appendix G).

The *unipolar* polarization- and displacement-electric field hysteresis loops of the samples sintered using the conditions found to be optimal for each sintering technique (see Section

4.2.4) are shown in Figure 5.23. For the samples sintered using the conventional or direct insertion method, the d_{33}^* value seems to decrease with increasing field, as the slope of the displacement curve drops around 1 $\frac{kV}{mm}$. The opposite effect is observed in the sample sintered using the immediate descent method, leading to an increase in the measured d_{33}^* value when the field is increased. These effects can be even more readily observed when performing the same unipolar measurements using a frequency of 250 mHz (see Appendix H).

The dielectric parameters for all the samples are summarized in Table 5.5. To see the effects of a changing displacement slope, the d_{33}^* value measured using an electric field of 2 $\frac{kV}{mm}$ was the one reported.

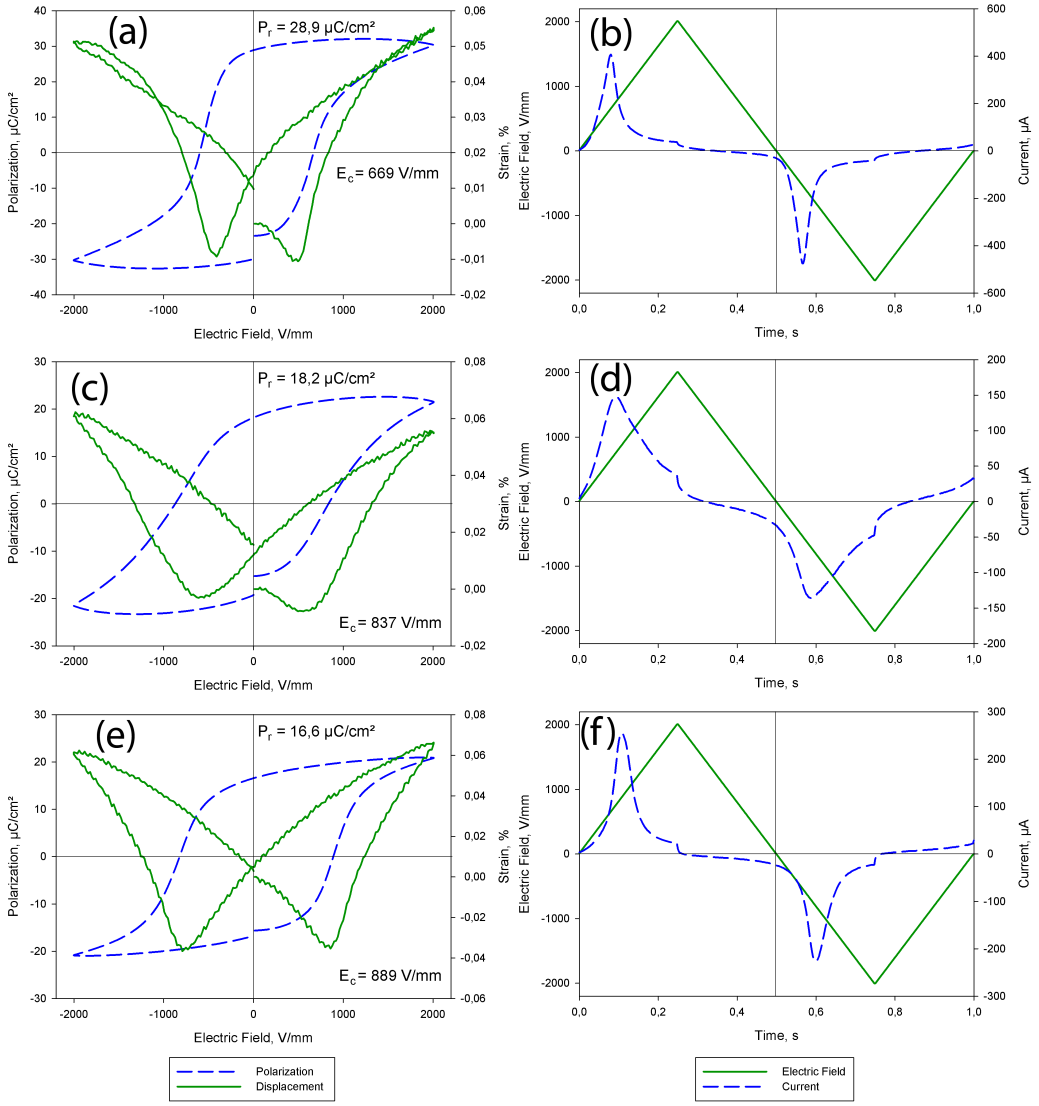

Figure 5.22: Bipolar polarization-displacement measurements and the corresponding I-V curves for the LKNNT samples sintered using the (a, b) conventional, (c, d) direct insertion and (e, f) immediate descent method. The measurements were made at room temperature and without any poling performed, using a frequency of 1 Hz and an electric field of 2 $\frac{kV}{mm}$.

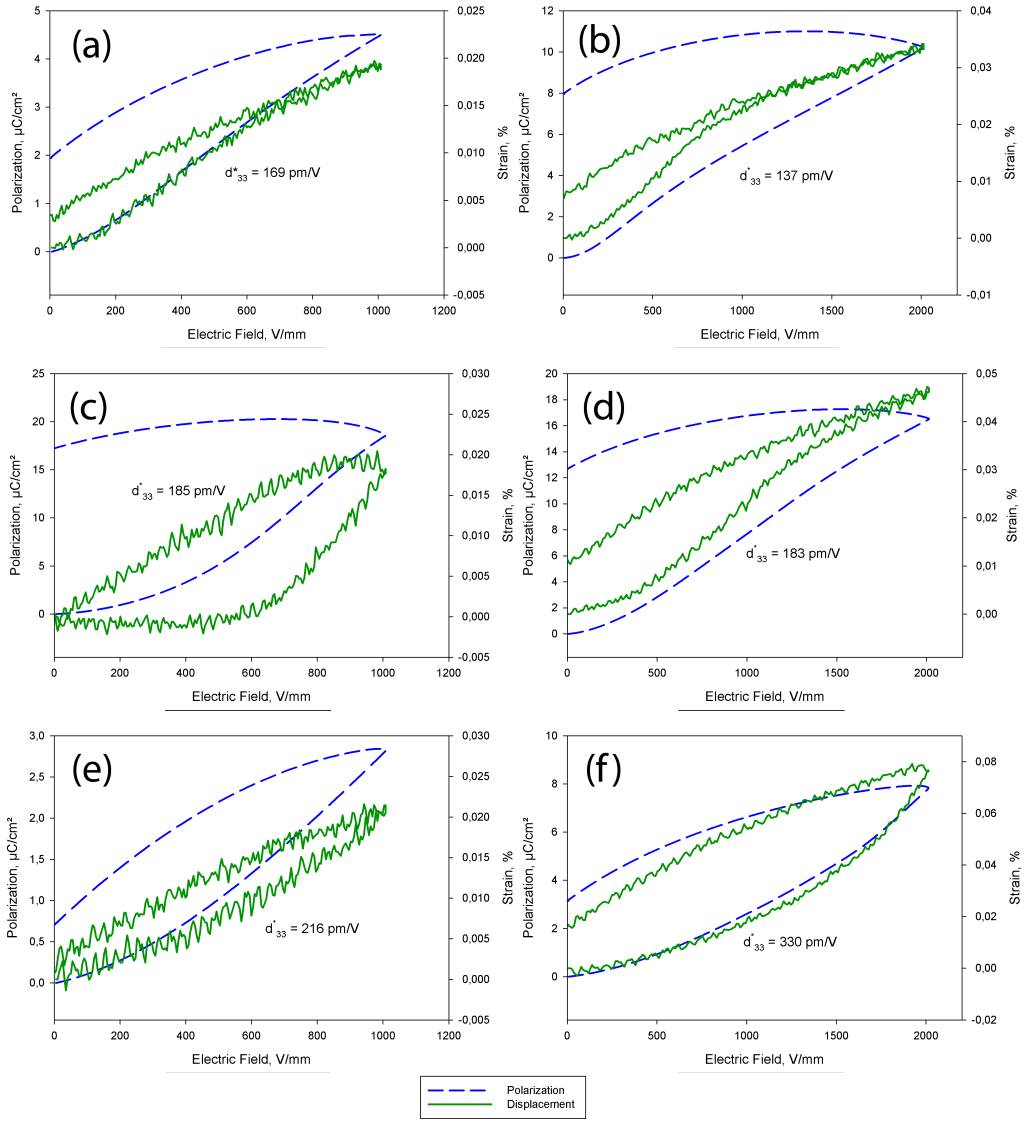

Figure 5.23: Unipolar polarization-displacement measurements for the LKNNT samples sintered using the (a, b) conventional, (c, d) direct insertion and (e, f) immediate descent method. The measurements were made at room temperature and without any poling performed, using a frequency of 1 Hz and an electric field of (a, c, e) 1 $\frac{kV}{mm}$ and (b, d, f) 2 $\frac{kV}{mm}$.

Table 5.5: Dielectric parameters of the samples sintered according to Section 4.2.4, and calculated according to Section 2.1.3. The values for the Curie temperature have been measured earlier [51].

Sintering method	$E_c\left(\frac{V}{mm}\right)$	$P_r\left(\frac{\mu C}{cm^2}\right)$	$d_{33}^*\left(\frac{\triangle S_{max}}{E_{max}}\right)\left(\frac{pm}{V}\right)$ (before poling)	$d_{33}^*\left(\frac{\triangle S_{max}}{E_{max}}\right)\left(\frac{pm}{V}\right)$ (after poling)	$T_C\,(^\circ C)$
Conventional	669	28.9	137	270	301
Direct insertion	837	18.2	183	230	301
Immediate descent	889	16.6	330	310	301

5.4.2 Poling effects

The *unipolar* polarization- and displacement-electric field hysteresis loops of the samples sintered using the conditions found to be optimal for each sintering technique (see Section 4.2.4), poled and aged using the setup shown in Section 4.2.6, are shown in Figure 5.24. The sloping effects mentioned in Section 5.4.1 seem to have been removed by the poling procedure. All the samples exhibit higher piezoelectric properties after poling and aging, except the sample sintered using the immediate descent method. The same behaviour can be observed when performing the same measurements at a lower frequency of 250 mHz (see Appendix H).

The *bipolar* polarization- and displacement-electric field hysteresis loops of the sample sintered using the direct insertion method (see Section 4.2.4), and the corresponding I-V curves, are shown in Figure 5.22. The butterfly loop is clearly distorted when comparing it to Figure 5.22, and the piezoelectric effect is observed to be much stronger in the forward direction (same direction as poling field). This effect is no longer observed after applying a negative, 1 Hz, 4 $\frac{kV}{mm}$ burst. Similar effects were observed in all the samples (see Appendix I).

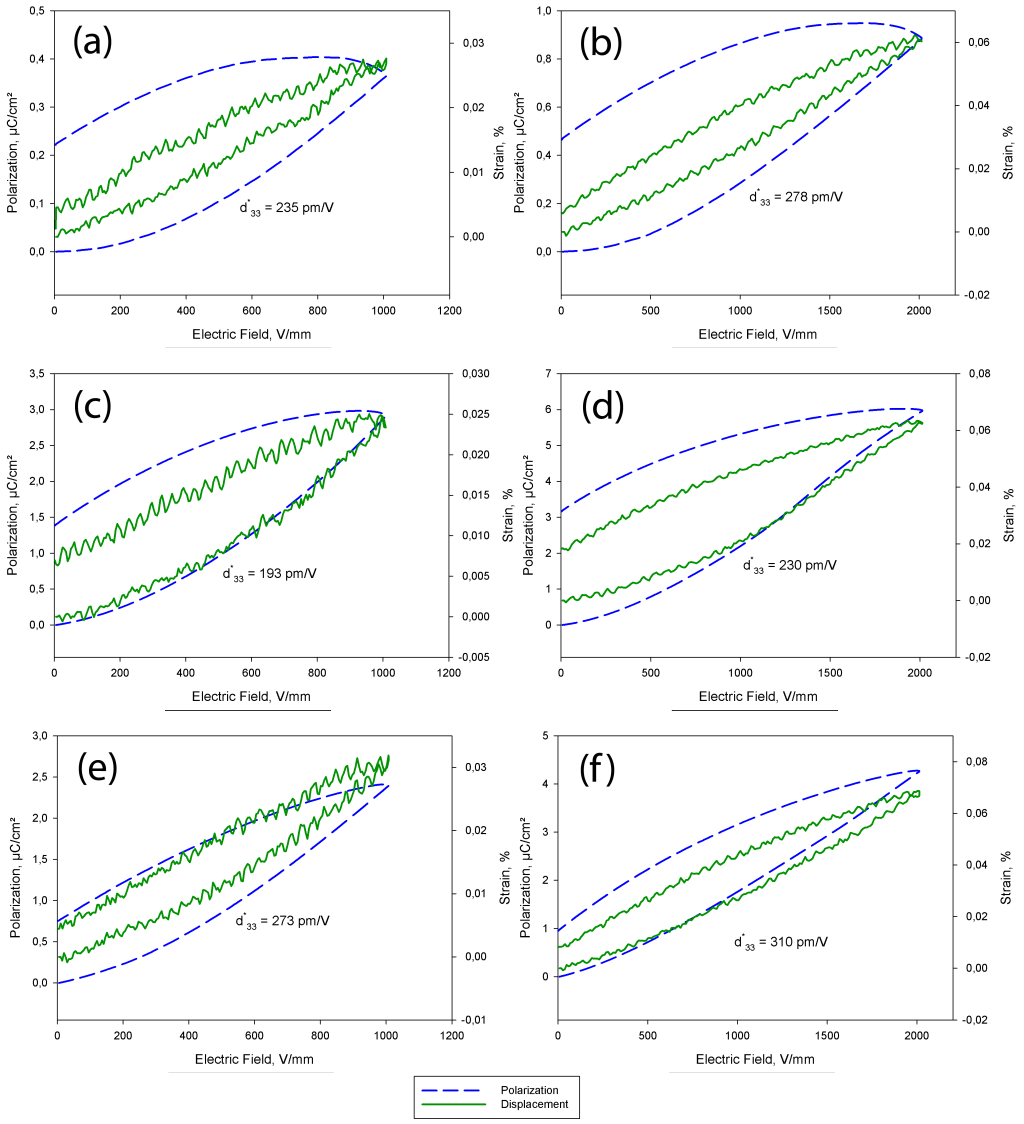

Figure 5.24: Unipolar polarization-displacement measurements for the LKNNT samples sintered using the (a, b) conventional, (c, d) direct insertion and (e, f) immediate descent method. The measurements were made at room temperature and after poling, using a frequency of 1 Hz and an electric field of (a, c, e) 1 $\frac{kV}{mm}$ and (b, d, f) 2 $\frac{kV}{mm}$.

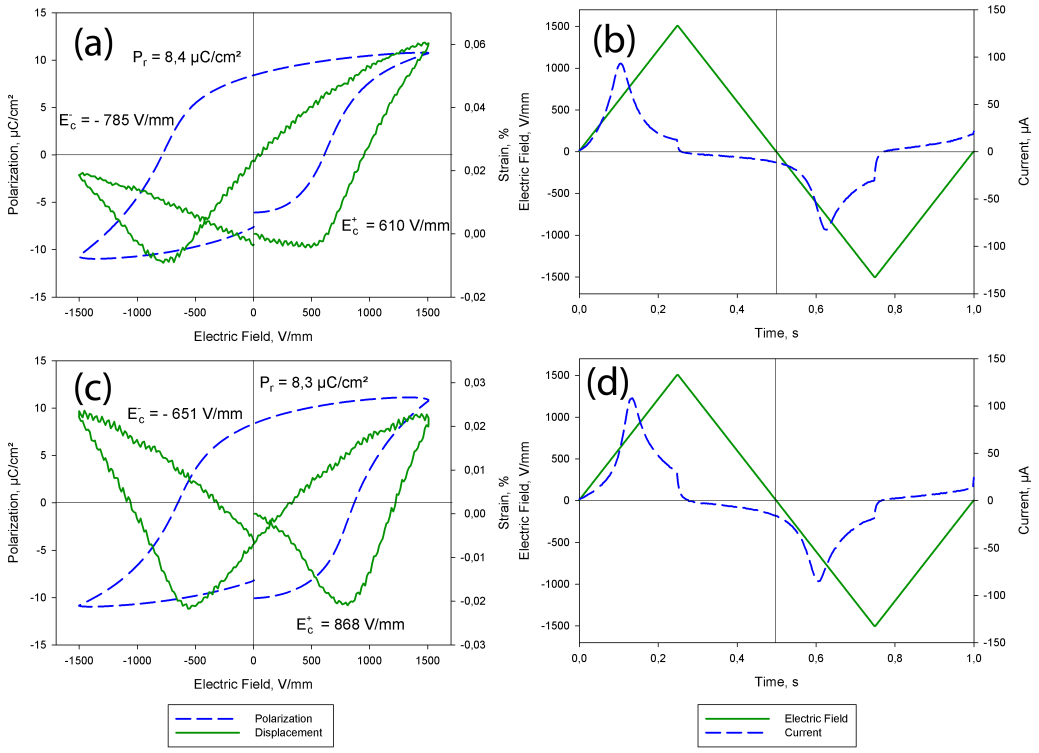

Figure 5.25: Bipolar polarization-displacement measurements and the corresponding I-V curves for the LKNNT sample sintered using the direct insertion method. The measurements were made at room temperature using a frequency of 1 Hz and an electric field of 1.5 $\frac{kV}{mm}$, and (a, b) after poling and aging, (c, d) after applying a negative, 1 Hz, 4 $\frac{kV}{mm}$ burst.

5.4.3 Aging effects

The d_{33}^*-value with respect to time after poling is shown in Figure 5.26, measured using different electric fields and frequencies. The d_{33}^*-value appears to increase drastically after poling, and then decrease to a relatively stable value after 5 hours. The d_{33}^*-value with respect to time for an unpoled material exposed to two 4 $\frac{kV}{mm}$ bursts are shown in Figure 5.27. The d_{33}^*-value appears to increase after the bursts, and be stable with respect to time. The unipolar, 1 Hz, 2 $\frac{kV}{mm}$ loops the d_{33}^*-measurements were based on are shown in Appendix I.

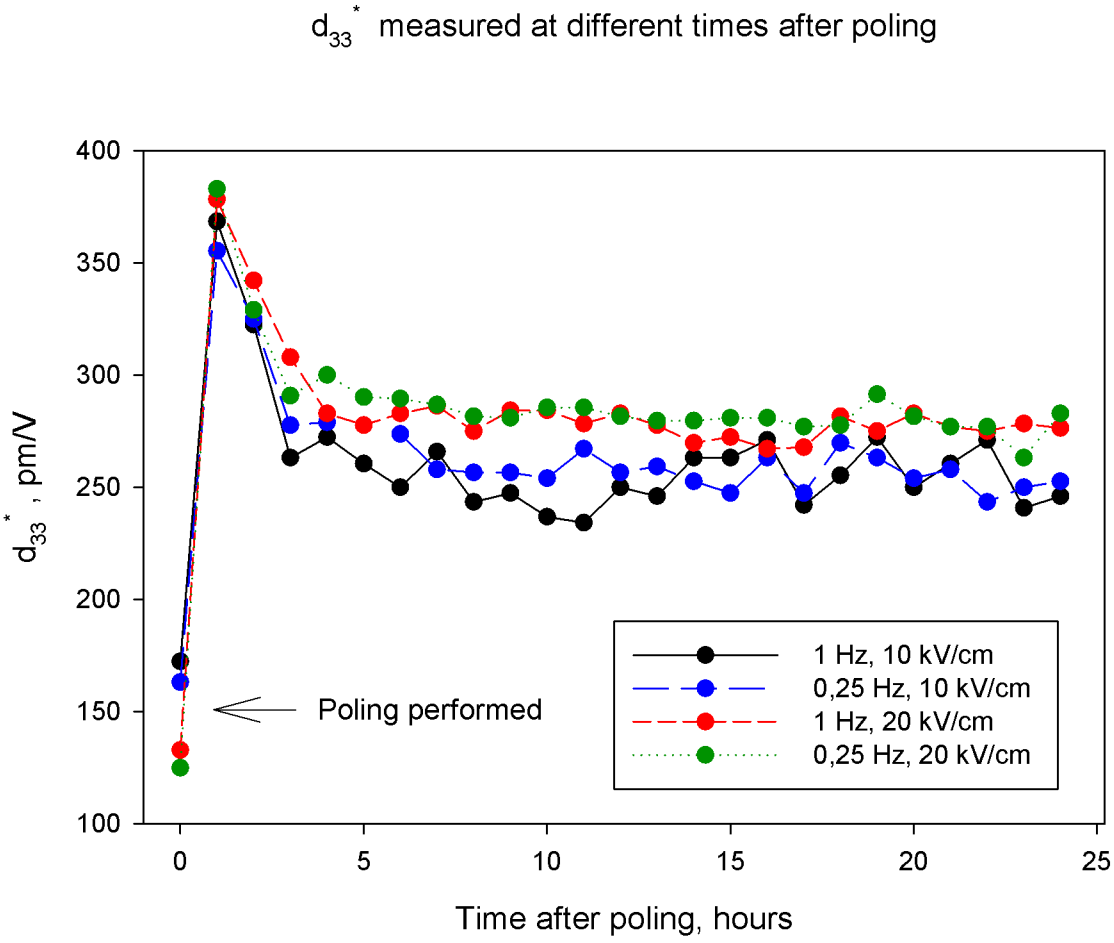

Figure 5.26: d^*_{33} measured at different times and conditions after poling, on the sample sintered using the conventional method.

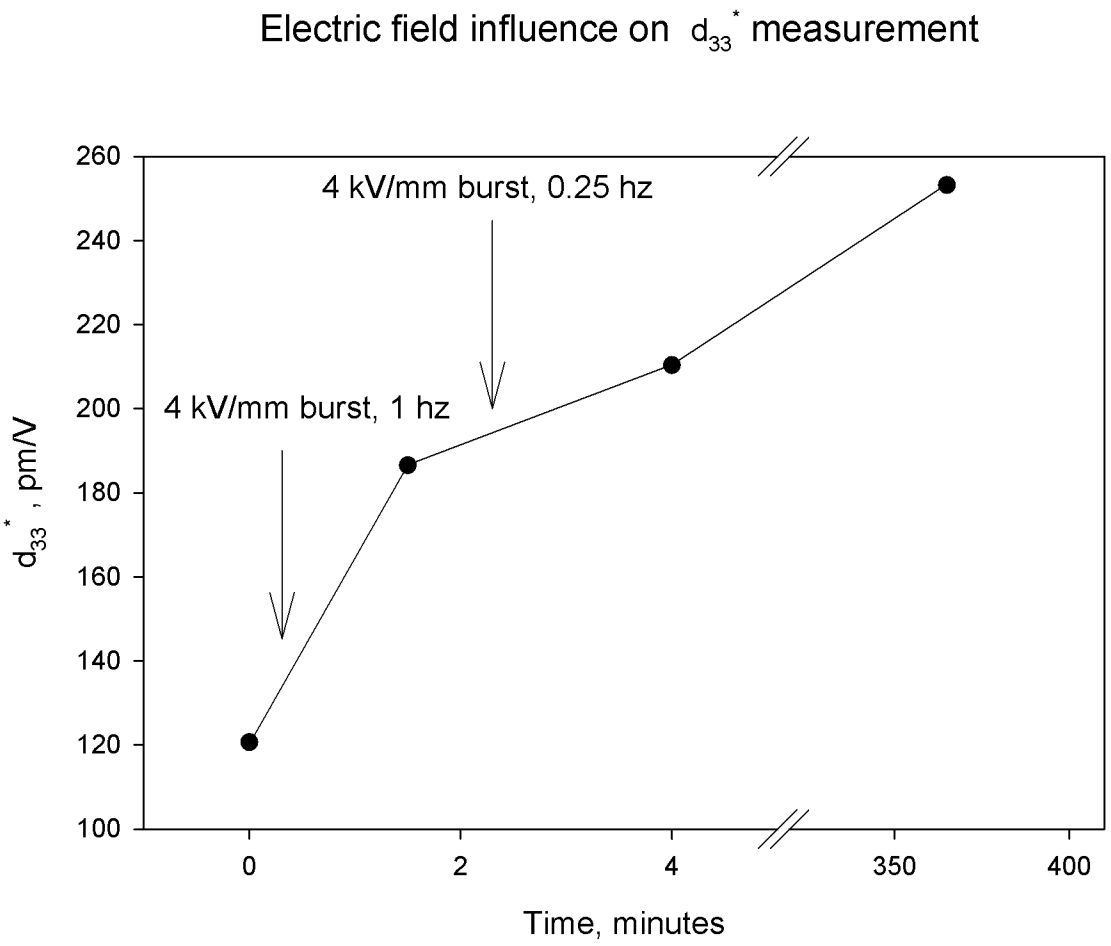

Figure 5.27: d_{33}^* measured on an unpoled sample sintered using the direct insertion method, after being exposed to two 4 $\frac{kV}{mm}$ bursts.

5.4.4 Temperature effects

d_{33}^* measurements performed at different temperatures are shown in Figure 5.28. The d_{33}^*-value appears to decrease with increasing temperature at all temperatures above 60 °C. At temperatures around 50 °C it seems the value could be increasing in a narrow temperature region.

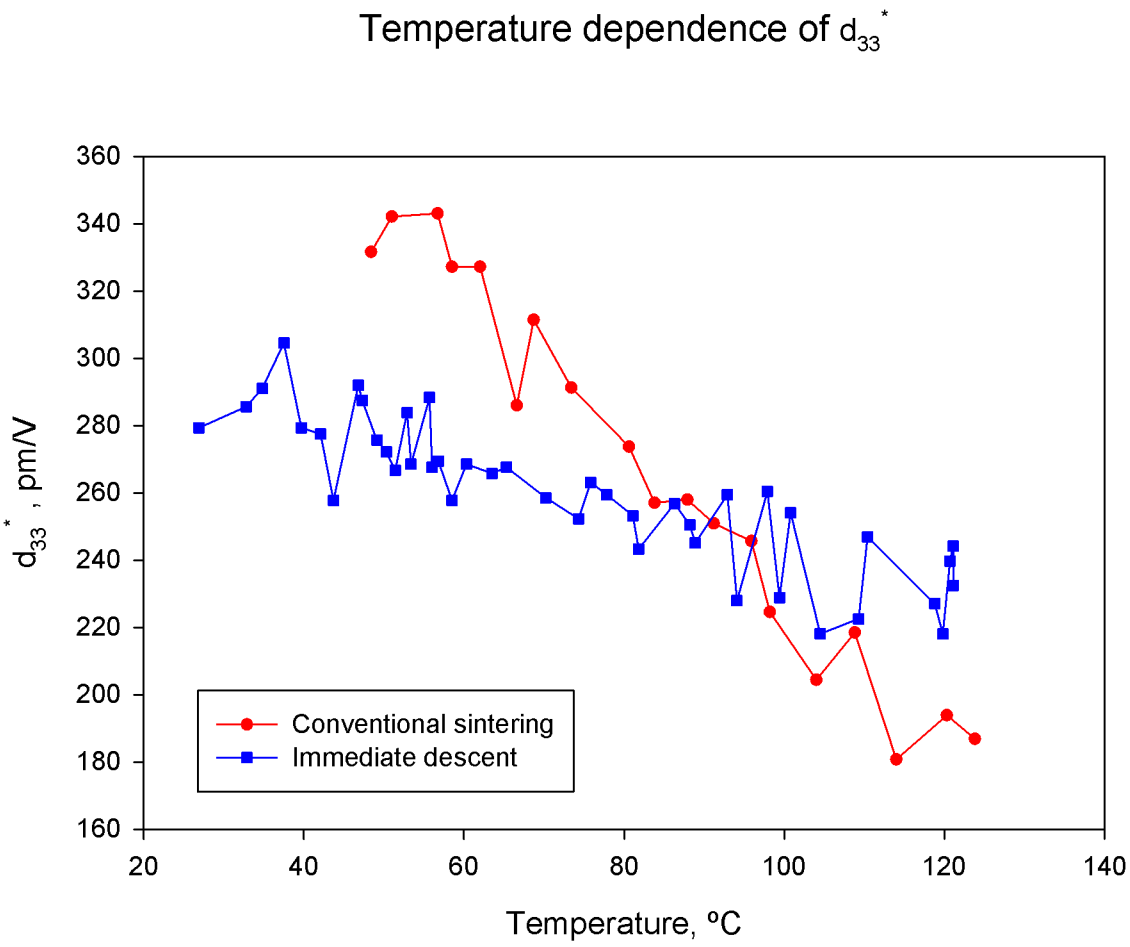

Figure 5.28: d_{33}^* measured at different temperatures after poling. The measurements were performed using a $1.5\frac{kV}{mm}$, 1 Hz unipolar loop.

6 Discussion

6.1 Milling

The as-prepared powder seems to consist of agglomerates of particles with a hollow, shell-shaped form (see Figure 5.1). The sizes of these particles fall in the range of 1 - 25 µm. This shape originates from the drying of the precursor solution droplets when being fed into the spray pyrolysis apparatus (see Section 2.3). Therefore, the thickness of the shells, and thus, the amount of energy needed to break them, probably depends on the concentration in the precursor. It is a common and necessary step to mill (grind) as-prepared ceramic powders, in order to increase the tap density/remove aggregates. This involves breaking the initial shells. Figure 5.1 clearly shows the necessity of this step, as a lot of solid spherical particles are visible. If attempting to form objects with unmilled powder, the object breaks apart as the agglomerates induce pore incorporation and a loose green body [16].

Three milling approaches were attempted (see Section 4.2.3). Dry planetary milling was found to be best suited with respect to powder morphology and sintering behaviour (see Section 5.2). The subsequent sieving at 250 micrometer seemed to be necessary, as several agglomerates existed in the powder after milling. This probably have some dependence on the degree of moisture present in the surrounding atmosphere. It is also evident that agglomerates smaller than 250 micrometer exist in the powder (see Figure 5.3). This should not represent a problem as long as the agglomerates are crushed in the green body formation, and could also give rise to a powder with good flowing properties and consequently a powder being easier to handle.

After this treatment, it should then be possible to form objects out of the powder and densify them with subsequent sintering (see Section 4.2.4 and 6.2).

6.1.1 Dry planetary milling

Several variations of rotation speeds and milling durations were attempted (see Figure 4.3). It was observed that fairly low rotation speeds were sufficient to break the shells, however a longer milling time seems to be necessary to achieve a powder with homogeneously sized particles. When applying too high rotation speeds, several objects resembling small and large flakes with sizes 10-100 µm were located in the powder afterwards (see Figure 5.5). It is speculated that these flakes originate when the powder is compressed between the wall of the milling container and the milling spheres, and/or between the milling spheres. For a simplified calculation of the pressures involved in the dry milling process, see Appendix C. These flakes are believed to resemble small green bodies, and is thus undesirable to have in the powder, as it generally will result in low quality green bodies. If they had their origin in the Zr milling spheres, a contrast should have been visible in the SEM images, which it

clearly is not (see Figure 5.6). When milling at a rotation speed of 200 RPM and above, the flakes are found evenly distributed in the powder after milling. When using 100 RPM, even a milling time in excess of 2 hours is not sufficient to remove the initial spheres (see Figure 5.2).

A suitable dry planetary milling process then becomes a question of using a rotation speed low enough to not creating flakes, and high enough to effectively break the shells. At the same time, it is desirable to spend as little time as possible, while still achieving a milled powder with a large degree of homogenity. In the light of these objectives, 155 RPM was chosen as the preferred rotation speed, using a milling time of 2 hours or less.

It was also observed that when dry milling the powder this way, it has a tendency to within minutes sink to the bottom of the container, which significantly reduces the milling effect. Therefore, a step of physically loosening the powder from the bottom of the container using a plastic spatula every 15 minutes of milling was included in the process. The milling time was then adjusted to be 6 x 15 minutes. This greatly improves the reproducibility of the green body densities (see Figure 5.12). The green body density is lowered with several percent with respect to the powder milled for 120 minutes (which is assumed to have undergone a smaller milling effect). This could be due to more homogeneously sized particles, and thus a smaller packing degree.

6.1.2 Wet planetary milling

Several variations of rotation speeds and milling durations were attempted, when using wet milling with 100% ethanol (see Figure 4.3). When applying wet planetary milling, it is observed that in general, the shells are harder to break. It also seems to be easier to avoid the flake formation, but unfortunately no milling treatment achieving no flakes and suitable shell breakage was found. If it is imperative to use a milling treatment using wet planetary milling, it is probably optimal to use a rotation speed of 300 RPM or lower, and a milling time of several hours (see Figure 5.9). It should then be possible to avoid flake formation, and still achieve sufficient shell breakdown. It is however problematic to use too long milling durations due to impurities being introduced to the powder, and the rotation speed should therefore be kept as high as possible, while still avoiding flake formation [52].

6.1.3 Ball milling

After ball milling with 100% ethanol for 26 hours, remnants of the initial shells were still present (see Figure 5.10). The degree of shell breakage still is quite high, and it seems likely that with an even higher milling time and/or a more suitable milling sphere/powder ratio, a sufficient milling treatment is achievable. This however is subject to the same disadvantage as the wet planetary milling: too long milling durations should generally be avoided due

to impurity introduction, assuming the amount of impurity addition is proportional to the distance traversed by the milling spheres [52].

6.2 Sintering

6.2.1 Temperature range

Results obtained earlier from dilatometry indicate that the densification process is favored by a large heating rate, rather than a small one [51]. The maximum densification rate seems to occur at temperatures above 1100 ^{o}C. It is known from prior studies that evaporation of the alkali metals occur at these temperatures (see Section 2.4). This could lead to evolution of abnormal grains, and poor sintering properties [20]. It should also be mentioned that the precise composition of the as-prepared powder is uncertain, and nonstoichiometries might be present from the beginning and affect the sintering process as well. If the phase transition is represented by a line in the phase diagram, nonstoichiometries might lead to secondary phases. This has not been observed for the samples used in this work. If there is an interval in the phase diagram instead, nonstoichiometries will change the point defects characteristics. In either case, it is likely that the sintering process will be affected [49]. Earlier it has been found that coarsening takes place in a broad temperature range below the temperature region where sintering is performed [51]. On this background, the method of pre-heating the sintering furnace and then inserting the uniaxially pressed pellets, was chosen as part of the procedure for two of the three sintering methods attempted, as this should result in a large heating rate. The reversed crucible method was always used during sintering, to limit the alkali evaporation (see Section 4.2.4) [20, 36, 51].

The sintering routes needed to be carefully optimised, as the final densities obviously are very dependent on sintering temperature, and even a change of 5-10 ^{o}C can cause a significant change (see Figure 5.14). This fact was also revealed by Hollenstein [36]. The sintering temperatures found to be optimal were around 10-15 ^{o}C higher than the ones chosen by previous studies [20, 36].

6.2.2 Optimal powder pretreatment

From Figure 5.13 and 5.3, it appears that a milling treatment of 155 RPM for 6 x 15 minutes provides the most suitable for achieving high densities. This could be due to the reduced agglomerate sizes facilitating larger driving forces for sintering. The flakes found when milling at higher rotation speeds probably inhibit the sintering driving force, resulting in less densified ceramics.

It is interesting to notice that the milling treatments leading to high green body densities, do not neccesarily correspond with high final densities (see Figure 5.11). It could be

speculated that this is due to the fact that powder with inhomogeneously sized agglomerates may attain a larger packing density, than the powder consisting of more homogeneously sized agglomerates due to heavier milling treatment (see Section 5.2.1). A powder with homogeneously sized agglomerates is believed to be more suitable for sintering. This is particularly visible when considering the powder loosened from the milling container every 15th minute (using a rotation speed of 155 RPM), which is believed to have undergone a more heavier milling process than the powder milled for 120 minutes at 155 RPM. Even so, this powder obtains a lower green body density, and still a higher final density after sintering.

6.2.3 Effect on microstructure

A final density of more than 95% is desirable, achieved using similar sintering temperatures and durations by both Hollenstein and Wang et al. [20, 36]. It should here be mentioned that temperature settings of furnaces provide some degree of uncertainty, which can be significant at higher temperatures. Several measures were taken to reduce this uncertainity to an absolute minimum (see Appendix A).

Using the conventional method or direct insertion, a density of 94 % is achieved when the temperature is chosen optimally. For the immediate descent method, the sintered densities were 95-97 %, slightly higher than by using the two other methods. The densities achieved are in accordance with what earlier authors have reported (see Section 2.4). This also correlates good with what authors using planetary milling have achieved [55]. The samples sintered using the immediate descent method also differs from the rest in that their porosities almost solely consist of closed porosity, indicating that the material is truly dense. Sintering materials using the two other methods to achieve mostly closed porosity seems difficult. It could be argued that it should be attempted to sinter at even higher temperatures, however so far this has only resulted in lower final densities.

Unfortunately the density dropped around 2 % of what had earlier been obtained for the same sintering treatment when thicker green bodies were sintered (see Table 4.6), probably due to an inhomogeneous green body as pressure gradients are more likely to occur in the thicker bodies.

When sintering without using a pre-heated furnace, a relatively broad grain size distribution evolves, and signs of excessive grain growth is observed (see Figure 5.17). This could be attributed to more time spent in the coarsening temperature range, due to a slower heating and cooling rate. When sintering using a pre-heated furnace, which results in a large heating rate and less time spent in the lower temperature range where coarsening is known to occur [51], a narrower grain size distribution, as well as a smaller average grain size, is achieved.

The immediate descent method seems to result in a narrow grain size distribution and the smallest average grain size. Still large grains of 4 µm are visible (see Figure 5.19), and

the standard deviation is estimated to be 0.25 μm, almost 17 % of the average grain size (see Table 5.3). It should be mentioned that the samples sintered using this method have spent the least amount of time in the furnace, 60 minutes in total. It could be speculated that this observed behaviour is due to *several* sintering mechanisms being dominant for the material, and operating in different temperature regions. That way, the temperature would have to be changed during the sintering process if more of these mechanisms are to be benefited from. The optimum temperature with respect to densification for one or more of these sintering mechanisms could also be believed to change during the sintering process, that is, to be a function of the achieved density and/or average grain size. In that sense, it would seem right to change the temperature during sintering as well.

It the light of Section 3.1, it could be speculated that the relatively inhomogeneous grain size distribution for all the sintered samples is due to the lithium dopants, and that it would be even more inhomogeneous if the tantalum dopants had not been added.

6.3 Compositional homogenity

A compositionally homogeneous material appears to have been achieved using the above mentioned synthesis and processing routes (see Section 5.3.4 and Appendix D). It is therefore likely that the contrast differences observed for the grains in the BSE images of Figure 5.20 are due to grain orientation and not compositional heterogeneities. The apperance of melting phases and the subsequent formation of glassy phases during sintering, could be due to silicon impurities. Silicon has absorption edges close to tantalum, so it would be difficult to detect using EDS.

Taking the reported purities of the starting chemicals of >99% (see Table 4.1) into account, it could be speculated that there is up to 1 % impurities present in the material synthesised. No such impurities have been detected using EDS (see Table 5.4), so it is assumed that these potential impurities in the starting chemicals were volatile and thus not present in the material synthesised in this work. At the same time, they cannot be completely ruled out due to EDS not being able to detect very small elemental amounts.

It has earlier been found that significant compositional inhomogeneity can erupt in Li- and Ta-modified KNN ceramics, which cannot be removed by a heat treatment process (see Section 3.1). These inhomogenities appear more pronounced when the material has been made using solid state synthesis, suggesting that the spray pyrolysis synthesis method used in this work may be advantageous in achieving compositionally homogeneous LKNNT ceramic bodies.

6.4 Dielectric properties

6.4.1 Unpoled response

On the background of Figure 5.22 and 5.23, it is apparant that the ferro- and piezoelectric effect is clearly visible in all the samples investigated (see Section 2.1). The piezoelectric effect varies in intensity depending on the sintering method, with the sample sintered using the immediate descent method achieving the most pronounced piezoelectric effect, with a d^*_{33} of 330 $\frac{pm}{V}$ at most. All measurements performed indicate that all samples, regardless of sintering method, achieve a d^*_{33} of at least 230 $\frac{pm}{V}$. 310 $\frac{pm}{V}$ has earlier been reported for the exact same composition [22].

Depending on the sintering method used, the material exhibits a different coercive field (see Table 5.5). There seems to be a correlation between the coercive field and the average grain size, as lower average grain sizes lead to higher coercive fields, suggesting that it takes more energy to achieve the switching in materials with smaller grains and more grain boundaries. It appears that the electric domains within small grains are more difficult to orient and switch than the electric domains within larger grains.

The sample sintered using the conventional method is not able to maintain the displacement during a bipolar measurement (see Figure 5.22), and it is observed not to follow a hysteresis loop until the field has dropped below 1.2 $\frac{kV}{mm}$. This should be viewed in the context of the unipolar displacement loops in some cases being seen to flatten out at electric fields above 1.2 $\frac{kV}{mm}$ (see Figure 5.23). It can be speculated that this is due to a electric field-induced phase transition, this is however unlikely due to the effect only being visible in some of the samples. It can be seen that this change of slope is accompanied by a polarization curve that increases when the field is being reduced, indicating a degree of conductivity, which would explain the observed behaviour. Earlier, it has been speculated that the degree of conductivity present severely affects the measurements [51]. Both the remnant polarizations and coercive fields found (see Table 5.5) may not reflect the real ferroelectric behavior of the material in the presence of too high conductivity (remnant polarization also arises due to moving electrons). In general, the real E_c and P_r will in that case be smaller [50]. A relatively high remnant polarization can indeed be seen where the behaviour described above is observed (see Figure 5.22.a and 5.23.a & b). These conductivity differences may have arisen due to different concentrations of vacancies in the samples, which may be traced back to the sintering method used.

Taking all the above mentioned effects into account, it would thus seem like the materials sintered to achieve smaller average grain size distributions (direct insertion, immediate descent) are better suited to operate in the higher electric field region, and the materials sintered to achieve larger average grain size distributions (conventional sintering method) are better suited to operate in the lower electric field regions.

Furthermore, when looking back at Section 6.2.3, it could then be argued that it should be possible to *tailor* the material through the use of selected sintering methods and parameters to achieve a particular coercive field (or a coercive voltage, for a given thickness).

6.4.2 Poling and aging

The effect of poling is clearly visible, by observing the difference in d_{33}^* before and after poling (see Figure 5.23 and 5.24). Poling increases the piezoelectric response significantly, and in some cases the value of d_{33}^* doubles after poling and aging. Aging is necessary as the piezoelectric constants are not stable directly after poling, and reduces to a more stable value in the hours following poling (see Section 2.1.4). Figure 5.26 suggests that the material has reached a stable state after 5 hours of aging after poling. Still, the long term effects of aging are not known, and measurements should be performed weeks and months after poling, to fully verify whether the piezo- and ferroelectric properties of the material are stable.

Several measurements suggests that the poling procedure could be simplified, as the same poling effect seems achieved even after short 4 $\frac{kV}{mm}$ bursts at room temperature (see Figure 5.27 and Appendix I). The expected increase in d_{33}^* is observed after applying the short bursts, and they appear to be as stable over time in the same manner as the normal poling procedure described in Section 4.2.6.

Figure 5.24 shows a significant dielectric response even without poling. This could indicate that poling takes place *during* measurement, and that LKNNT is easily polable.

6.4.3 Temperature effects

The value of d_{33}^* decreases as the temperature is increased, as the electric domains are randomized and the material depolarized due to the increased thermal energy (see Figure 5.28). It seems 110 °C is enough to reduce d_{33}^* to a stable value, it should however be noted that the Curie temperature of this material has been measured to 301 °C (see Table 5.5), which should be sufficient to fully depolarize the material and return it to its original shape. It is evident from Figure 5.28) that at temperatures of 90 °C and above, the electric domains of the material seems very mobile, as it seems the field applied to measure the piezoelectric response heavily affects the result. This effect is more pronounced for the sample sintered using the immediate descent method, having a smaller average grain size distributions.

It seems the value of d_{33}^* increases in the temperature region of 50-60 °C. This could be due to a phase transition occuring in that region, and is suggested that this is the orthorhombic to tetragonal phase transition, in accordance with what is observed by Wang et al. [20].

6.5 Reproducibility

Several measures were taken to increase the degree of reproducibility, described below.

6.5.1 Synthesis

The ceramic powder synthesis by spray pyrolysis has only been performed once (see Section 4.2.1 and 4.2.2), and it is therefore not known wheter it is reproducible. Generally, it is believed that the spray pyrolysis process is simple compared to other synthesis methods, and thus attains reproducibility with greater ease [31].

6.5.2 Milling

It appears that the step of stopping the mill and loosening the powder is necessary to achieve an effective milling process, and by doing this the green body densities obtained show a more narrow distribution, across different powder batches and also within a given powder batch (see Figure 5.12). The degree of moisture will probably affect the milling effect, and it could therefore be advantageous to include a heating step prior to the milling, in order to remove any moisture present. Moisture is indeed present in the powder after storage outside a dessicator, as a thermogravimetric analysis of calcined powder stored in a plastic box for a week shows (see Appendix E).

6.5.3 Sintering

With the above measures taken, sintering seems to provide reproducible results as well, regardless of the sintering method used (see Figure 5.14 and 5.16).

6.5.4 Dielectric properties

It is seen that the dielectric properties were not reproducible when the samples were kept in atmosphere for long durations (see Appendix F). It was speculated that this behaviour arose due to moisture effects, as well as a phase separation taking place in the surface of the samples. It was therefore needed to implement extra steps to ensure reproducibility (see Section 4.2.6). These were to keep the samples in dessicators to decrease the moisture exposure as much as possible, to sinter thicker samples and polish them on both sides, to attach electrodes on the whole surface, and to keep the sample in the dielectric tester after poling. At that point it is submerged in oil and any atmosphere exposure should therefore not be expected.

After implementing this method, all the samples investigated attain reasonable and expected dielectric results. Since the sintering procedure differs among the samples investigated, more samples should probably be prepared using the same sintering methods to check whether the dielectric properties are truly reproducible.

7 Conclusion

7.1 Concluding remarks

$K_{0.485}Na_{0.485}Li_{0.03}Nb_{0.8}Ta_{0.2}O_3$ powder has been synthesised by spray pyrolysis, and calcined at 600 °C. Spray pyrolysis appears to be an excellent way of synthesising this ceramic powder, as relatively few and simple processing steps are needed. Dry planetary milling, wet planetary milling as well as ball milling have been attempted varying rotation speed and duration. Scanning electron microscopy was used to evaluate the milling effect and investigate the powder morphology. It was found that dry planetary milling at 155 RPM was most suitable and effective, as it successfully breaks the initial spheres originating from the spray pyrolysis process without creating hard flakes in the powder. Hard flakes was observed when the pressure arising between the milling container walls and milling spheres were too high resulting from too high rotation speeds. To achieve a homogeneously milled powder as well as a high milling effect, steps were implemented where the powder was manually loosened from the milling container during milling, settling on 6 x 15 minutes of milling. Green bodies were pressed through the use of uniaxial pressing, and three different sintering methods were explored: conventional sintering, direct insertion and immediate descent. The reverse crucible was adapted, and in the two last methods the furnace was pre-heated to ensure a high heating rate. The highest densities achieved were around 94 % for the first two methods, sintering at 1156 °C, and 97 % when sintering using the immediate descent method, the only sintering method where the vast majority of the porosity is closed and thus truly dense.

The microstructure of the different samples was explored by polishing the samples using a water based solution with diamonds and investigate the surface by scanning electron microscopy. It was found that the conventional sintering method results in a broader grain size distribution than the two other, with a larger average grain size. It was speculated whether this was the result of too long exposure to the temperature range where coarsening is known to occur. For the immediate descent and direct insertion method, the grain size distributions attain a standard deviation of less than 0.3 µm, and average grain sizes of less than 2 µm. The immediate descent method resulted in the smallest average grain size, probably due to it spending the least amount of time inside the furnace. For all the sintering methods, compositional homogenity is observed.

Dielectric testing was performed on the samples sintered using the different sintering methods. The ferro- and piezoelectric effect is clearly observed for all samples investigated, and poling the material at 4 $\frac{kV}{mm}$ shows an increase in the normalized strain d_{33}^*. The value of d_{33}^* is found to be in the range of $230 - 330\frac{pm}{V}$, with the sample sintered according to the immediate descent method showing the largest value of d_{33}^*. It is seen that samples having a microstructure with a smaller average grain size, demonstrate a higher coercive

field. Conductivity differences are observed for different sintering methods, and it is believed that this arises due to differences in vacancy concentrations. It should be possible to tailor the material with respect to dielectric parameters using different sintering parameters.

A survey is made regarding the reproducibility of the results, and it is found that care needs to be taken in the milling process, as well as the dielectric testing. This is mostly due to moisture related effects, a variable which is difficult to control.

On the basis of the present results, $K_{0.485}Na_{0.485}Li_{0.03}Nb_{0.8}Ta_{0.2}O_3$ has potential as a leading candidate for environmentally friendly piezoelectric materials, and spray pyrolysis is a suitable synthesis method.

7.2 Future work

The sintering temperatures that have been used in this work are relatively high. It could be useful to include a sintering additive in order to reduce the sintering temperature and further avoid the problem of alkali evaporation, ease the processing route and further limit the grain growth.

Applying a high temperature X-Ray Diffraction (XRD) instrument on the powder would be helpful, as the orthorombic to tetragonal phase transition could be found this way. This phase transition temperature is probably an excellent choice of poling temperature, as the crystal structure is unstable at this temperature. It would also be interesting to study the other poling parameters such as field duration.

The milling treatment could also be further explored, by using for example high-energy attrition milling. This could result in even higher densities as the driving forces for sintering increases as the particle sizes are further reduced.

It would also be of interest to increase the cooling rate used in the immediate descent sintering method, as this could lead to even narrower grain size distributions as well as a smaller average grain size. By achieving more control over the sintering process the dielectric properties could be tailored to suit different needs.

The aging effect on the material could be even more thoughourly studied, by letting the material age for weeks and months, and then check wheter the dielectric properties has been degraded. It would also be interesting to find out whether different concentrations of vacancies arises through the use of different sintering methods.

References

[1] Saito, Y. et al., "Lead-free piezoceramics", *Nature*, 432(4), pp. 84-87 (2004).

[2] European Union Directive 2002/96/EC: "Waste Electrical and Electronic Equipment (WEEE)", Off. J. Eur. Union, 46, L37, 24–38 (2003).

[3] European Union Directive 2002/95/EC: "The Restriction of the use of certain hazardous substances in Electrical and Electronic Equipment", Off. J. Eur. Union, 46, L37, 19–23 (2003).

[4] Moulson, A., et al., "Electroceramics", second edition, Wiley (2003).

[5] Kwan, C., "Dielectric phenomena in solids", Elsevier Academic Press (2004).

[6] Shrout, T. et al., "Lead-free piezoelectric ceramics: Alternatives for PZT?", Journal of Electroceramics, 19:111–124 (2007).

[7] Matsubara, M. et al., "Processing and Piezoelectric Properties of Lead-Free $(K, Na)(Nb, Ta)NbO_3$ Ceramics", J. Am. Ceram. Soc., 88 [5] 1190–1196 (2005).

[8] Madaro, F., "Synthesis of textured $K_xNa_{1-x}NbO_3$ materials", PhD Thesis, Department of Materials Science and Engineering, Faculty of Natural Sciences and Technology, Norwegian University of Science and Technology (2009).

[9] Haertling, G., "Ferroelectric Ceramics: History and Technology", J. Am. Ceram. Soc., 82 [4] 797–818 (1999).

[10] Nagata, H. et al., "Fabrication and Piezoelectric Properties of Textured $Bi_{\frac{1}{2}}K_{\frac{1}{2}}TiO_3$ Ferroelectric Ceramics", Japanese Journal of Applied Physics, 49 (2010).

[11] Nam-Binh, D. et al., "Effect of Ta-Substitution on the Ferroelectric and Piezoelectric Properties of $Bi_{0.5}\left(Na_{0.82}K_{0.18}\right)_{0.5}TiO_3$ Ceramics", Transactions on Electrical and Electronic Materials, Vol. 12, No. 2, 64-67 (2011).

[12] Ullah, A. et al., "Phase Transition, Electrical Properties, and Temperature-Insensitive Large Strain in $BiAlO_3$-Modified $Bi_{0.5}\left(Na_{0.75}K_{0.25}\right)_{0.5}TiO_3$ Lead-Free Piezoelectric Ceramics", J. Am. Ceram. Soc., 1–7 (2011).

[13] Xu, M. et al., "Phase diagram and electric properties of the (Mn, K)-modified Bi0.5Na0.5TiO3–BaTiO3 lead-free ceramics", J Mater Sci 46, 4675–4682 (2011).

[14] Ishihara, T., "Perovskite Oxide for Solid Oxide Fuel Cells", Springer, 1-16 (2009).

[15] Wenk, H. et al., "Minerals: Their Constitution and Origin", Cambridge University Press, New York (2004).

[16] Richerson, D., "Modern Ceramic Engineering", Taylor & Francis (2006).

[17] Lu, C. et al., "The effect of grain size on domain structure in unsupported $PbTiO_3$ thin films", J. Phys.: Condens. Matter 8 8011–8016 (1996).

[18] Trolier-McKinstry, S., "Crystal Chemistry of Piezoelectric Materials", Springer (2008).

[19] Ahn, C. et al., "Sintering Behavior of Lead-Free $(K, Na)NbO_3$-BasedPiezoelectric Ceramics", Journal of the American Ceramic Society, 92, 2033–2038 (2009).

[20] Wang, Y. et al., "High-Temperature Instability of Li- and Ta-Modified $(K, Na)NbO_3$ Piezoceramics", J. Am. Ceram. Soc., 91 [6] 1962–1970 (2008).

[21] Kim, M. et al., "Microstructures and Piezoelectric Properties in the Li_2O-Excess $0.95(Na_{0.5}K_{0.5})NbO_3 - 0.05LiTaO_3$ Ceramics", J. Am. Ceram. Soc., 90 [10] 3338–3340 (2007).

[22] Hollenstein, E. et al., "Piezoelectric properties of Li- and Ta-modified $(K_{0.5}Na_{0.5})NbO_3$ ceramics", Applied Physics Letters 87, 182905 (2005).

[23] Wang, Y. et al., "Compositional Inhomogeneity in Li- and Ta-Modified $(K, Na)NbO_3$ Ceramics", J. Am. Ceram. Soc., 90 [11] 3485–3489 (2007).

[24] Wu, J. et al., "Microstructure and electrical properties of (Li, Ag, Ta, Sb)-modified $(K_{0.50}Na_{0.50})NbO_3$ lead-free ceramics with good temperature stability", J. Phys. D: Appl. Phys. 41 125405 (2008).

[25] Guo, Y. et al., "$(Na_{0.5}K_{0.5})NbO_3 - LiTaO_3$ lead-free piezoelectric ceramics", Materials Letters 59 241–244 (2005).

[26] Niu, X. et al., "Crystalline structural phase boundaries in $(K, Na, Li)NbO_3$ ceramics", Solid State Communications 146 395–398 (2008).

[27] Li, J. et al., "Normal sintering of $(K, Na)NbO_3$-based lead-free piezoelectric ceramics", Ceramics International 34 783–786 (2008).

[28] Shen, Z. et al., "Electrical and Mechanical Properties of Fine-Grained Li/Ta-Modified $(Na, K)NbO_3$-Based Piezoceramics Prepared by Spark Plasma Sintering", J. Am. Ceram. Soc., 93 [5] 1378–1383 (2010).

[29] Jaffe, B. et al., "Piezoelectric ceramics", Academic Press, London (1971).

[30] Lines, M. et al., "Principles and applications of ferroelectrics and related materials", Clarendon Press, Oxford (1977).

[31] Perednis, D. et al., "Thin Film Deposition Using Spray Pyrolysis", Journal of Electroceramics, 14, 103–111, (2005).

[32] Levy, M., "Crystal Structure and Defect Property Predictions in Ceramic Materials", PhD Thesis, Department of Materials, Imperial College of Science, Technology and Medicine, University of London (2005).

[33] Haugen, A. et al., "TiO_2, TiO_2/Ag and TiO_2/Au photocatalysts prepared by spraypyrolysis", J.Eur.Ceram. Soc. (2010).

[34] Bjørkeng, L., Master thesis, Department of Material Science and Engineering, Faculty of Natural Sciences and Technology, Norwegian University of Science and Technology (2010).

[35] Wang, K. et al., "Low-Temperature Sintering of Li-Modified $(K, Na)NbO_3$ Lead-Free Ceramics: Sintering Behavior, Microstructure, and Electrical Properties", J. Am. Ceram. Soc., 93 [4] 1101–1107 (2010).

[36] Hollenstein, E., "Preparation and properties of $KNbO_3$-based piezoelectric ceramics", PhD Thesis, la faculté des sciences et techniques de l'ingénieur, École polytechnique fédérale de Lausanne, Switzerland (2007).

[37] Uchino, K., Proc. New Actuator 2004 (Bremen, June 14–16), p.127 (2004).

[38] Uchino, K., "Piezoelectric actuators 2006", J. Electroceramics 20:301–311 (2008).

[39] Fujii, A., Proc. JTTAS Meeting on Dec. 2, Tokyo (2005).

[40] Ahart, M. et al., "Origin of morphotropic phase boundaries in ferroelectrics", Nature 451, 545-548 (2008).

[41] Chiang, Y. et al., "Lead-free high-strain single-crystal piezoelectrics in the alkaline–bismuth–titanate perovskite family", Applied Physics Letters 73, number 25, 3683-3685 (1998).

[42] Chu, B. et al., "Electrical properties of $Na_{\frac{1}{2}}Bi_{\frac{1}{2}}TiO_3 - BaTiO_3$ ceramics", Journal of the European Ceramic Society 22, 2115–2121 (2002).

[43] Kakimoto, K. et al., "Ferroelectric and Piezoelectric Properties of $KNbO_3$ Ceramics Containing Small Amounts of $LaFeO_3$", Jpn. J. Appl. Phys. Vol. 42, 6102–6105 (2003).

[44] Baker, D. et al., "A comprehensive study of the phase diagram of $K_xNa_{1-x}NbO_3$" Appl. Phys. Lett., 95, 091903 (2009).

[45] Tellier, J. et al., "Crystal structure and phase transitions of sodium potassium niobate perovskites" Solid State Sci., 11, 320-324 (2009).

[46] Zhen, Y. et al., "Normal Sintering of $(K, Na)NbO_3$-Based Ceramics: Influence of Sintering Temperature on Densification, Microstructure, and Electrical Properties", J. Am. Ceram. Soc., 89 [12] 3669–3675 (2006).

[47] Mochel, J., US Patent 2,564,707 (1951).

[48] Hill, J. et al., US Patent 3,148,084 (1964).

[49] Palcut, M. et al., "Cation Self-Diffusion and Nonstoichiometry of Lanthanum Manganite Studied by Diffusion Couple Measurements", J. Phys. Chem. C , 111, 813-822 (2007).

[50] Meyer, R. et al., "Dynamic leakage current compensation in ferroelectric thin-film capacitor structures", Applied Physics Letters 86, 142907 (2005).

[51] Strand, J., "Development of lead-free electroceramics - $K_{0.5}Na_{0.5}NbO_3$ substituted with $LiTaO_3$", Department of Material Science and Engineering, Faculty of Natural Sciences and Technology, Norwegian University of Science and Technology (2010).

[52] Grader, G. et al., "Spray pyrolysis of YBCO precursors", J. Mater. Res., Vol. 9, No. 10 (1994).

[53] López, R. et al., "Structural and electrical characterization of $(K_{0.48}Na_{0.52})_{0.96}\,Li_{0.04}Nb_{0.85}Ta_{0.15}O_3$ synthesized by spray drying", Journal of the European Ceramic Society, 30 1549–1553 (2010).

[54] Morozov, M. et al., "Effects of poling over the orthorhombic-tetragonal phase transition temperature in compositionally homogeneous $(K, Na)NbO_3$-based ceramics", Applied Physics Letters 98, 132908 (2011).

[55] Zuo, R. et al., "Sintering and Electrical Properties of Lead-Free $Na_{0.5}K_{0.5}NbO_3$ Piezoelectric Ceramics", J. Am. Ceram. Soc., 89, 2010 – 2015 (2006).

[56] Song, H. et al., "Microstructure and Piezoelectric Properties of $(1-x)(Na_{0.5}K_{0.5})NbO_3-xLiNbO_3$ Ceramics", J. Am. Ceram. Soc., 90, 1812 – 1816 (2007).

[57] Chang, Y. et al., "Microstructure, density, and dielectric properties of lead-free $(K_{0.44}Na_{0.52}Li_{0.04})(Nb_{0.96-x}Ta_xSb_{0.04})O_3$ piezoelectric ceramics", J. Am. Ceram. Soc., 90, 1656 – 1658, (2007).

A Sintering temperaure measurement adjustments

It was observed that, and confirmed in literature, that the LKNNT material is very sensitive with respect to sintering temperature [20, 36]. Even a small change of 5 - 10 ºC seemed to result in changes in the measured density of several percent (see Section 5.2.2). Therefore, it was imperative to seek as precise temperature measurements as possible. Two measures were taken to achieve this. Firstly, an attachement of an external thermocouple measuring circuit using an ice bath as the cold junction and pure Pt and Pt with 10% Rh as the thermocouple materials (Type S, NIST Standard Reference) provided a more accurate measurement of the temperature at the hot junction inside the furnace, as it should not depend on room temperature or possess any contaminations. Secondly, a measurement of the temperature gradient between the hot junction and the actual position where sintering takes place was performed by placing pure gold pellets inside the furnace and observing at which observed temperature they melted. The calculated deviations are shown in Figure A.1. It was found that the external thermocouple always showed a lower temperature than the embedded thermocouple, and this temperature difference varied between 3,5 °C to 8 °C. It is believed that this is due to the fact that the embedded thermocouple, having no fixed cold junction, is dependent on the room temperature. This temperature difference seemed to vary from hour to hour, and after switching heat elements. This made it difficult to heat the furnace to the desired temperature with a precision greater than 1,5 °C, since the furnace will heat according to the temperature measured by its embedded thermocouple. The difference between the top and bottom of the furnace was measured to be 14 °C (using the external thermocouple to measure the temperature at the top).

It is assumed that the temperature difference between the top and bottom of the furnace is the same around the melting temperature of gold (1064,18 °C), as it is in the sintering temperature range. It is also assumed that the external thermocouple measuring circuit has a significantly higher degree of accuracy than the thermocouple embedded in the furnace. Taking both of these assumptions into considerations, it is still expected that the temperature adjustments performed on this basis still have some level of inaccuracies (± 1 °C).

On this background, all the sintering temperatures used in this work have been adjusted to reflect the actual sintering temperature, by measuring using the external thermocouple and subtracting 14 °C.

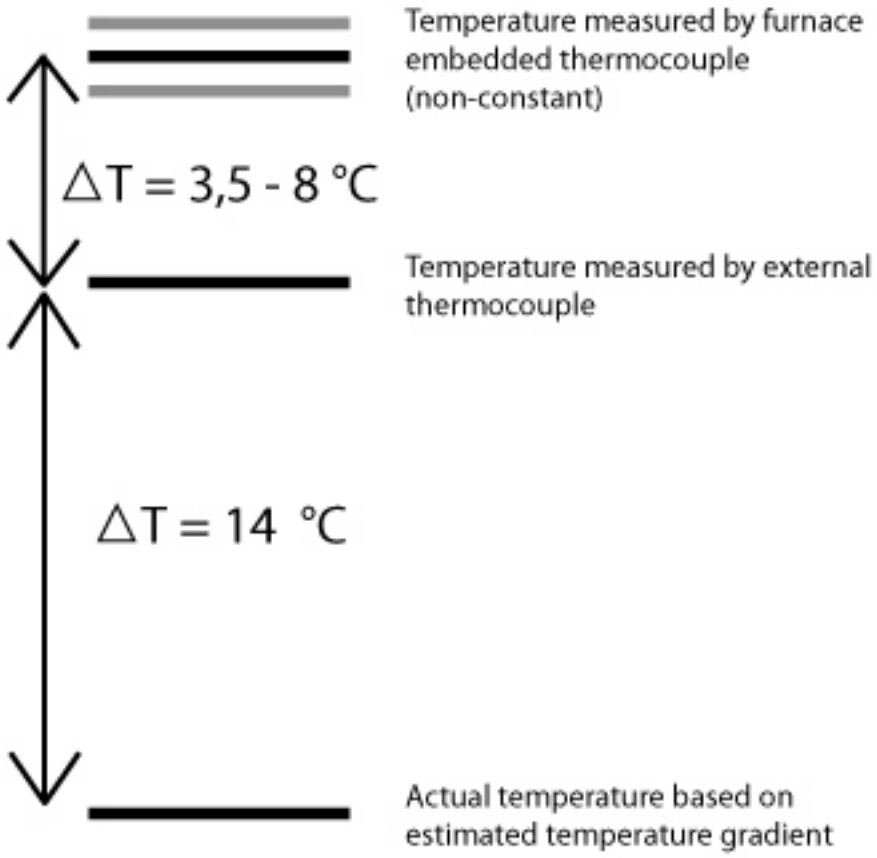

Figure A.1: Furnace setpoint with adjustments.

B Other sintering results

Figure B.1 shows the results of other milling and sintering attempts, resulting in lower densities and solely open porosity. The positive effect on sintered density by increasing milling time is visible. An overview of all the samples sintered using the direct insertion method are shown in Figure B.2. The improvement in final density by changing milling procedure and increasing sintering temperature is visible.

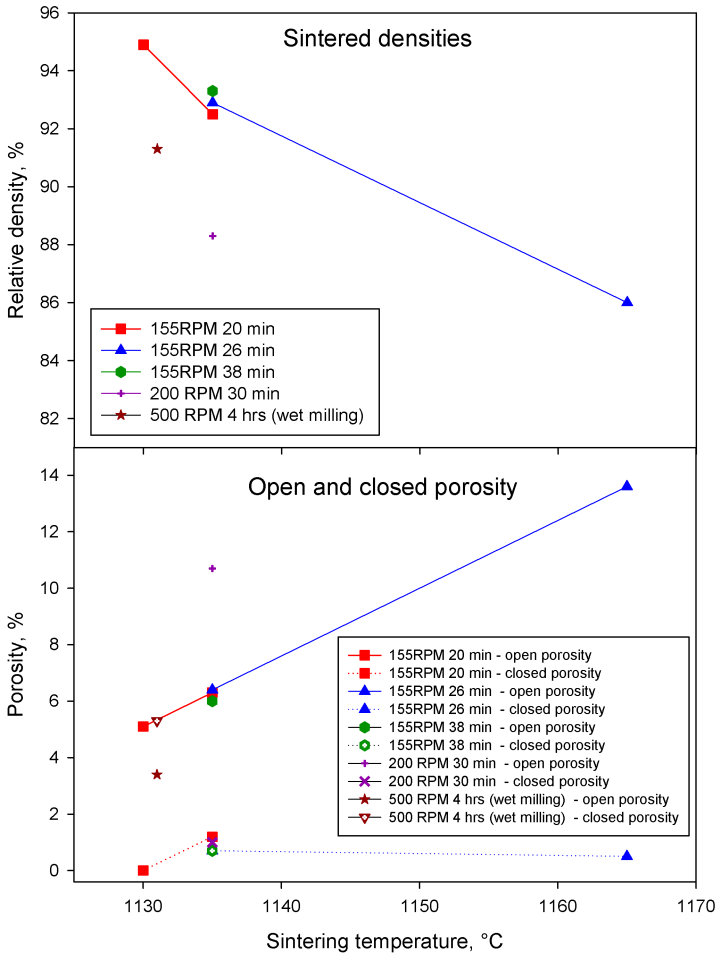

Figure B.1: Final densities after sintering for 1 hour by direct insertion, measured by Archimedes' method. The reversed crucible method was used, and the samples were inserted into a pre-heated furnace to ensure a high heating rate. After 1 hour they were quenched in air.

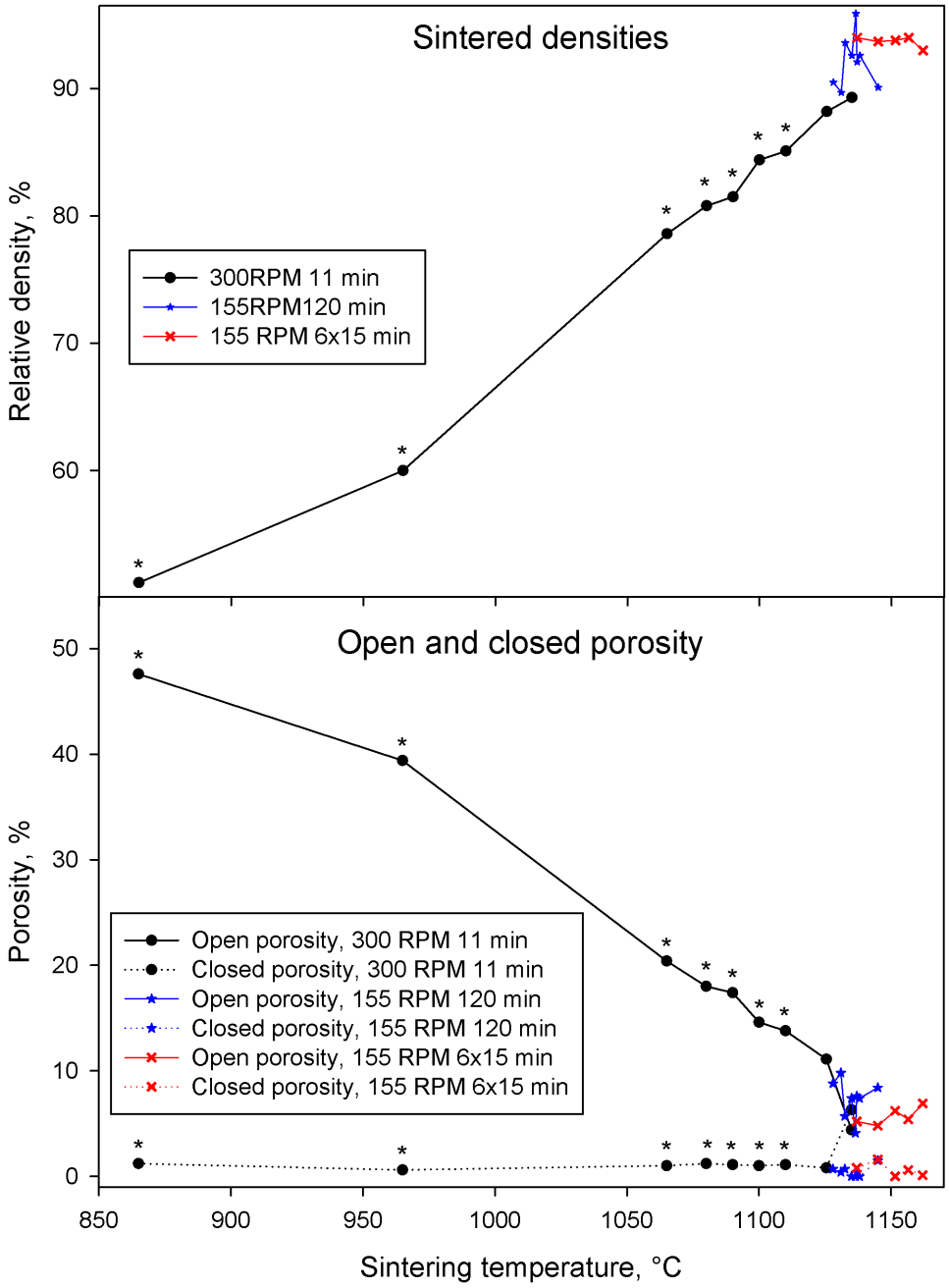

Figure B.2: Final densities after sintering for 1 hour by direct insertion, measured by Archimedes' method. The reversed crucible method was used, and the samples were inserted into a pre-heated furnace to ensure a high heating rate. After 1 hour they were quenched in air. The samples marked with (*) are from earlier work [51].

C Planetary milling calculations

To estimate the pressure between container wall and milling spheres, the energy delivered to the powder, and the area covered by the milling spheres during milling, an analytical approach was made, based on a model of milling spheres rotating inside the milling container. This way, new suitable planetary milling conditions based on already existing results could be found. Equation 1 is an estimate of the total energy delivered to the powder during milling. It can be divided on the total powder mass to estimate energy delivered per mass of powder. Equation 2 is an estimate of the total area covered by the milling spheres during milling. Equation 3 is an estimate of the pressure arising between the milling spheres and the wall of the container during milling. This pressure was especially important to estimate due to the problem of powder being compressed to flakes/green bodies during milling (see Section 6.1.1).

$$E = \frac{\pi n t m \omega^3 (R+r)^2}{108000} \tag{1}$$

$$A_{cov} = \frac{\pi^2 t n r_s^2 f_s^2 r \omega}{30m} \tag{2}$$

$$p = \frac{m\omega^2 (R+r)}{3600\pi r_s^2 f_s^2} \tag{3}$$

n - number of milling spheres

t - milling time (s)

m - mass of powder

ω - rotation speed (s^{-1})

R - radius of rotation axis

r - radius of milling container

r_s - radius of milling spheres

f_s - fraction of sphere cross sectional area (πr_s^2) in contact with container wall (measured to 0,17)

D EDS elemental mapping

EDS element maps showing the spatial distribution of elements are shown in Figure D.1. Similar mappings were taken on samples sintered using all the different methods, with close to identical results.

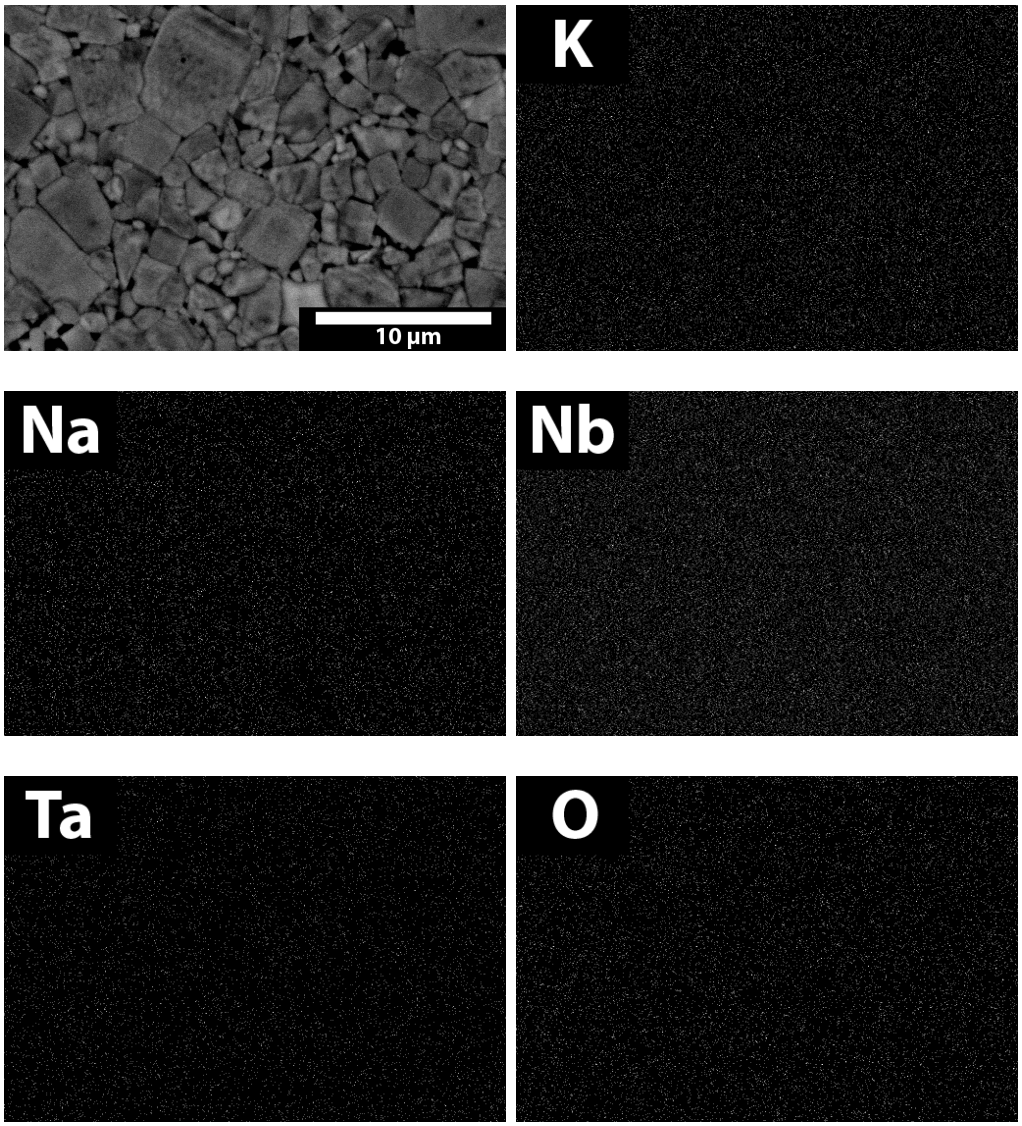

Figure D.1: EDS element maps showing the spatial distribution of elements. They are, K, Na, Li, Nb, Ta, O. The sample was been sintered using the conventional method at 1156 °C. Lithium could not be detected using EDS due to its low atomic number.

E Thermogravimetric analysis

To observe/confirm the presence of moisture in the ceramic powder, a thermogravimetric analysis was performed on calcined powder left in a plastic container for a week. A mass loss of more than 1 % is visible when the powder is heated to 400 °C.

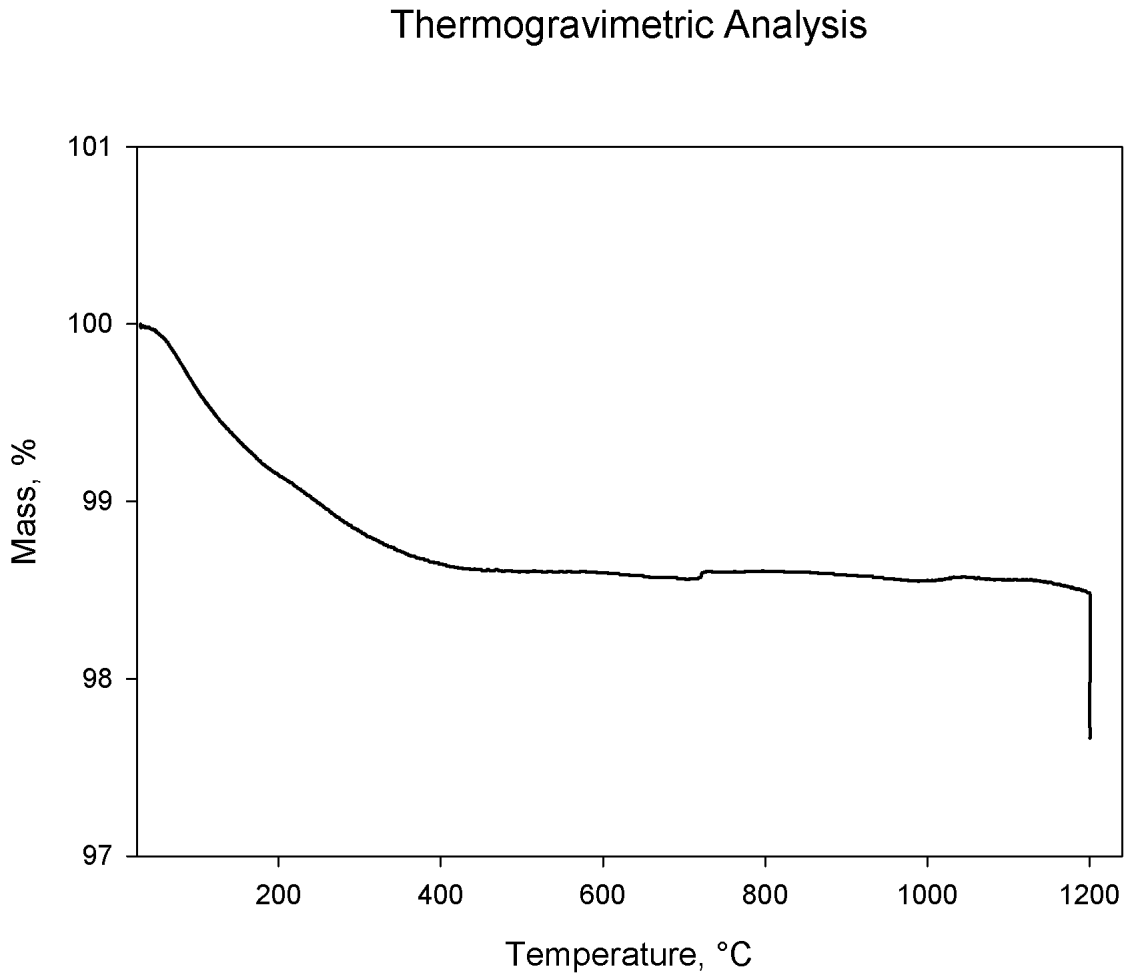

Figure E.1: Thermogravimetric analysis performed on powder calcined at 600 °C using a heating rate of 10 $\frac{^{\circ}C}{min}$, a holding time of 1 hour, in pure O_2.

F Other dielectric results

Figure F.1 shows selected results where the samples were *not* polished and kept in dessicators prior to measurements, as described in Section 4.2.6. It was observed that samples sintered and treated similarly, did not show similar dielectric results. reproducibility was difficult to achieve. Therefore, it was decided to include these extra processing steps in order to reduce the experimental errors.

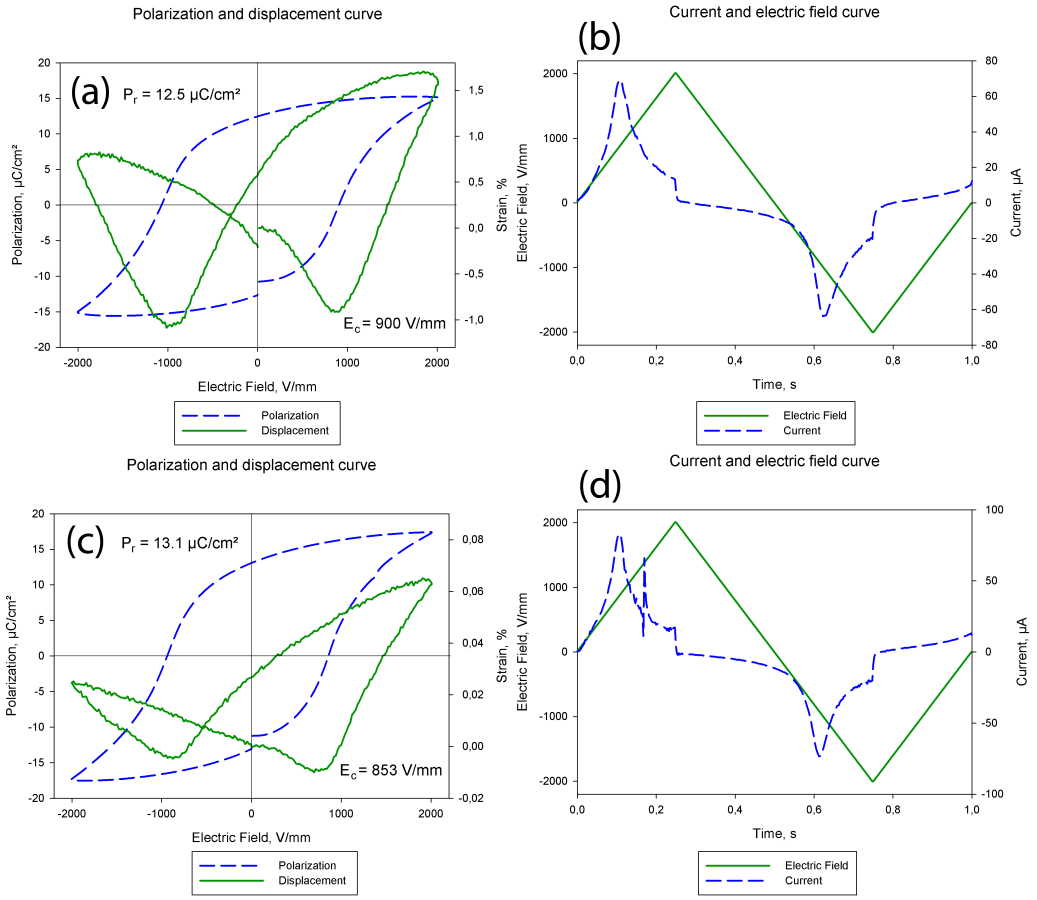

Figure F.1: Bipolar polarization-displacement measurements and the corresponding I-V curves for LKNNT samples milled using dry planetary milling at 155 RPM for 120 minutes, and sintered using the direct insertion method, at (a, b) 1165 °C and (c, d) 1170 °C. The measurements were made at room temperature and without any poling performed, using a frequency of 1 Hz and an electric field of 2 $\frac{kV}{mm}$.

G Bipolar dielectric measurements using 1 $\frac{kV}{mm}$

Figure G.1 shows bipolar polarization- and displacement-electric field hysteresis loops of the samples sintered using the conditions found to be optimal for each sintering technique (see Section 4.2.4), and the corresponding I-V curves. The switching effect is clearly observed in all the samples. The sample sintered using the immediate descent method appears to have more difficulty switching than the two other samples (note the unsteep polarization curve) at these electric fields. This sample does indeed display the highest coercive field when measured at 2 $\frac{kV}{mm}$ (see Section 5.4.1).

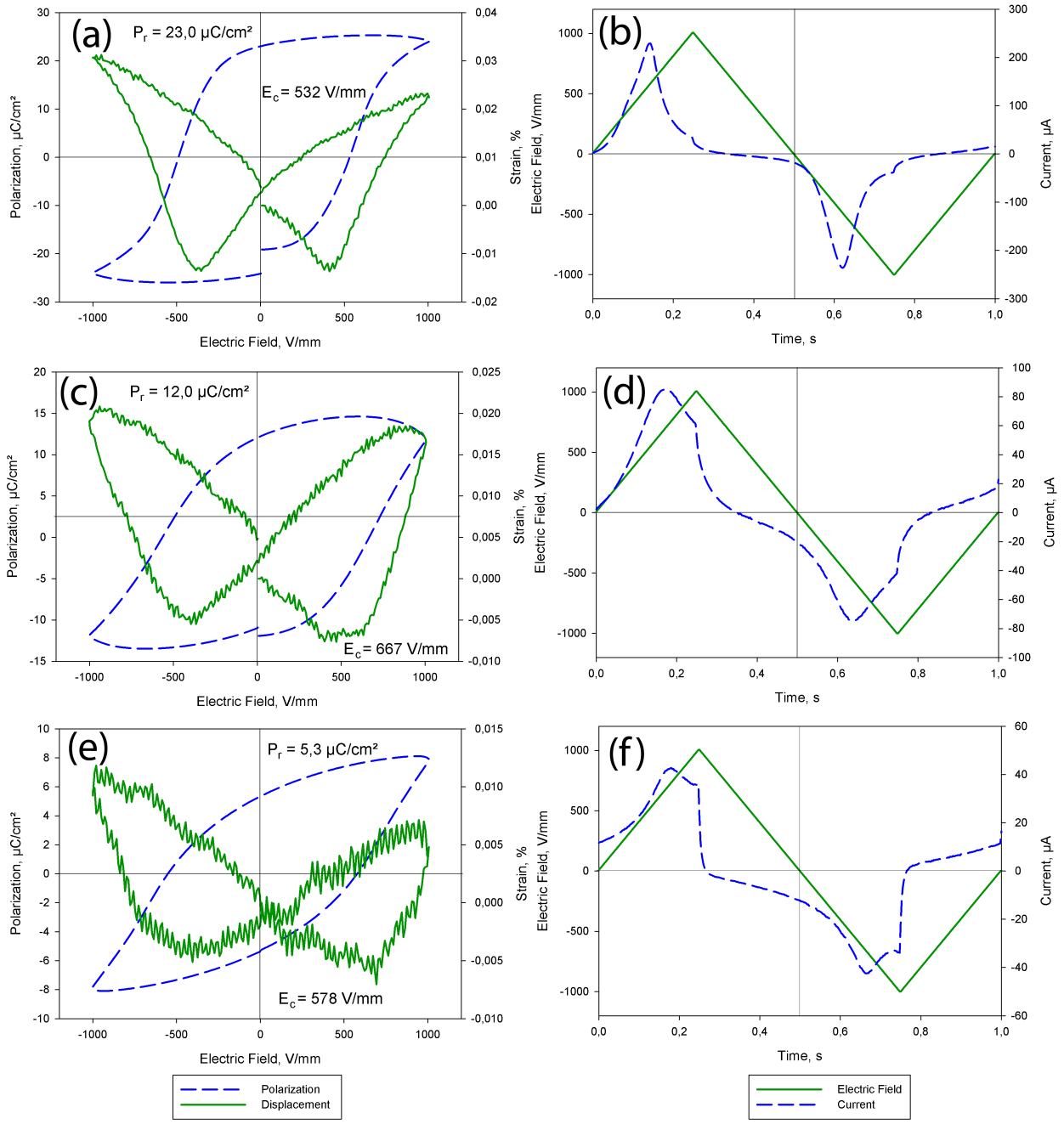

Figure G.1: Bipolar polarization-displacement measurements and the corresponding I-V curves for the LKNNT samples sintered using the (a, b) conventional, (c, d) direct insertion and (e, f) immediate descent method. The measurements were made at room temperature and without any poling performed, using a frequency of 1 Hz and an electric field of 1 $\frac{kV}{mm}$.

H 250 mHz unipolar dielectric measurements

Figure H.1 and H.2 show the same measurements depicted in Section 5.4.1 and 5.4.2, however using a frequency of 250 mHz instead of 1 Hz. The same behaviour as described in Section 5.4 can be observed for these measurements as well.

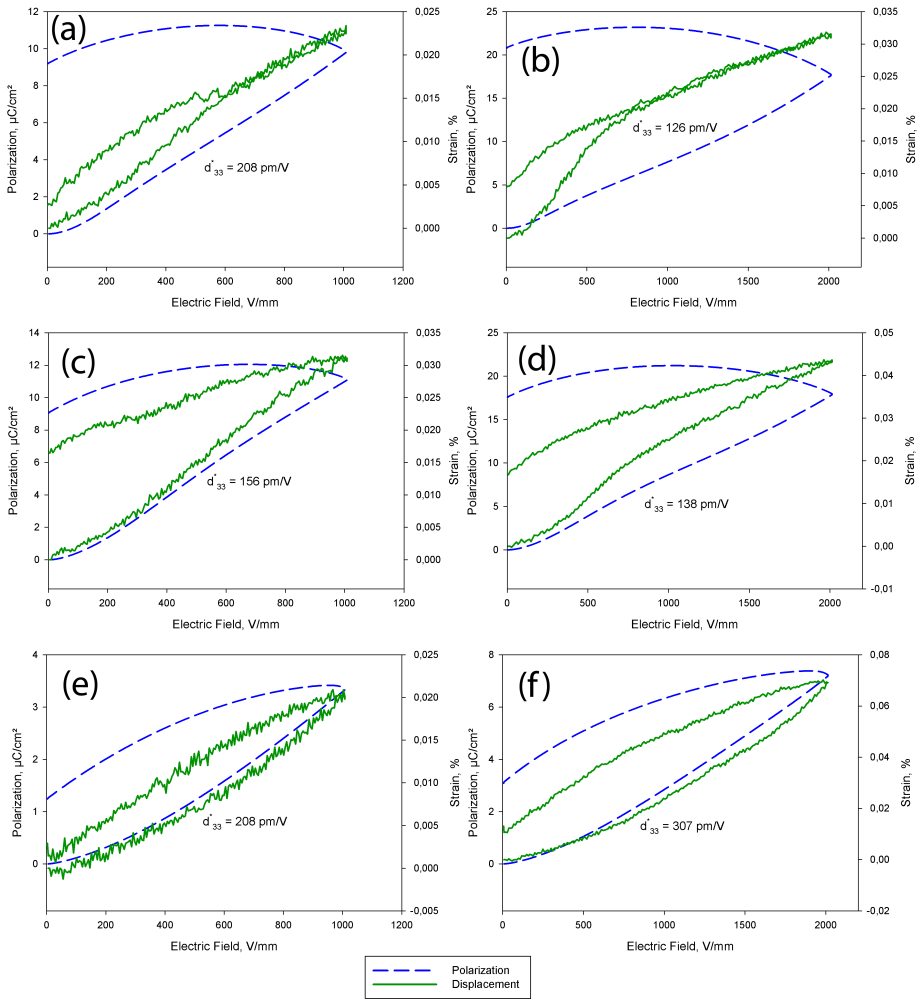

Figure H.1: Unipolar polarization-displacement measurements for the LKNNT samples sintered using the (a, b) conventional, (c, d) direct insertion and (e, f) immediate descent method. The measurements were made at room temperature and without any poling performed, using a frequency of 250 mHz and an electric field of (a, c, e) 1 $\frac{kV}{mm}$ and (b, d, f) 2 $\frac{kV}{mm}$.

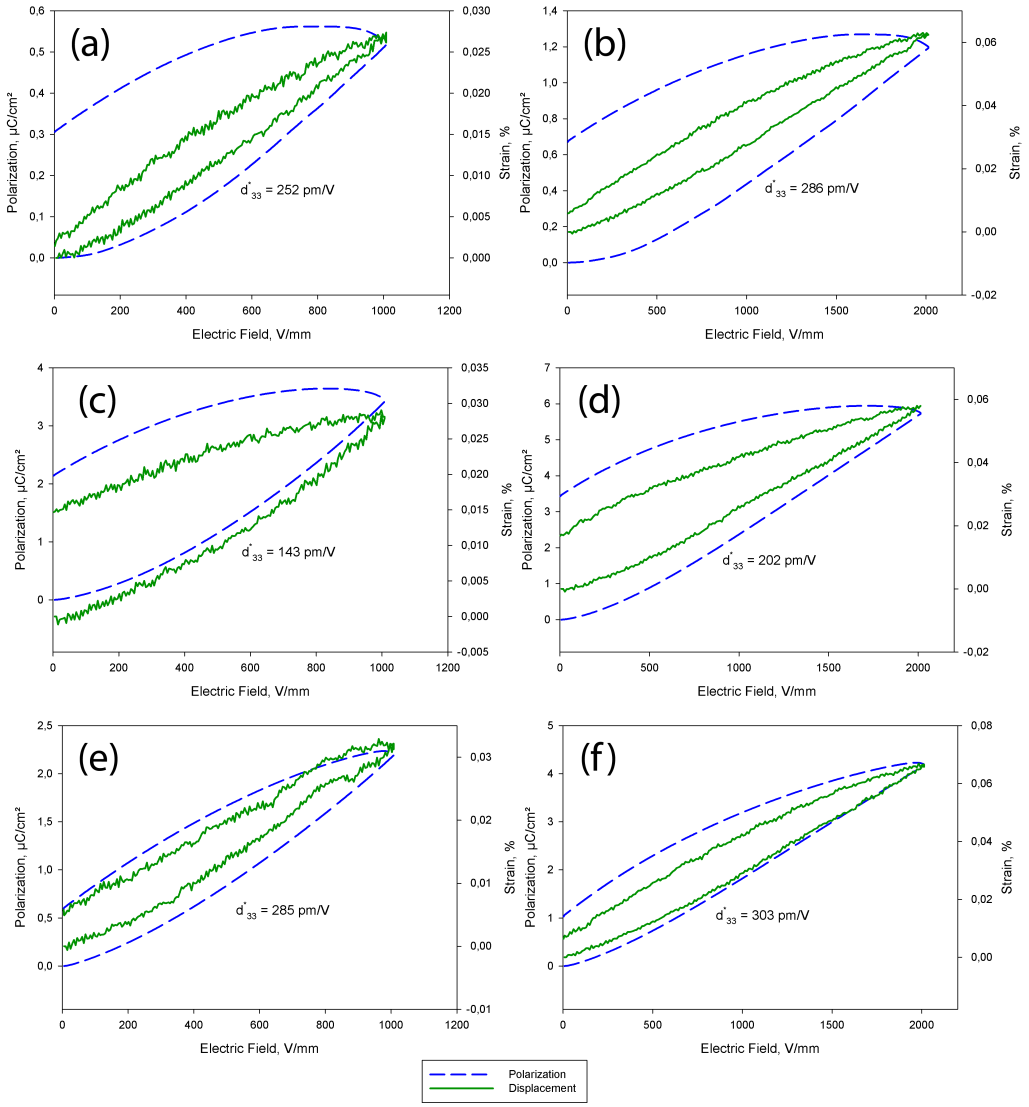

Figure H.2: Unipolar polarization-displacement measurements for the LKNNT samples sintered using the (a, b) conventional, (c, d) direct insertion and (e, f) immediate descent method. The measurements were made at room temperature and after poling, using a frequency of 250 mHz and an electric field of (a, c, e) 1 $\frac{kV}{mm}$ and (b, d, f) 2 $\frac{kV}{mm}$.

I Short poling bursts

Some attempts were made to achieve the poling effect using short burst of electric fields, instead of the longer poling treatment described in Section 4.2.6, as it was suspected that the LKNNT materials were easily poled (see Section 6.4.2). Figure I.1 shows three measurements, taken seconds after one another. They show how the sample is (a) poled initially, (b) "unpoled" by applying a bipolar burst, and (c) apparantly poled again by applying a 3 $\frac{kV}{mm}$, 1 Hz, unipolar burst.

Figure I.2 shows how a sample, initially unpoled, is apparantly poled using a 4 $\frac{kV}{mm}$, 1 Hz, unipolar burst, and that the poling effect appears to still be present 6 hours after the burst.

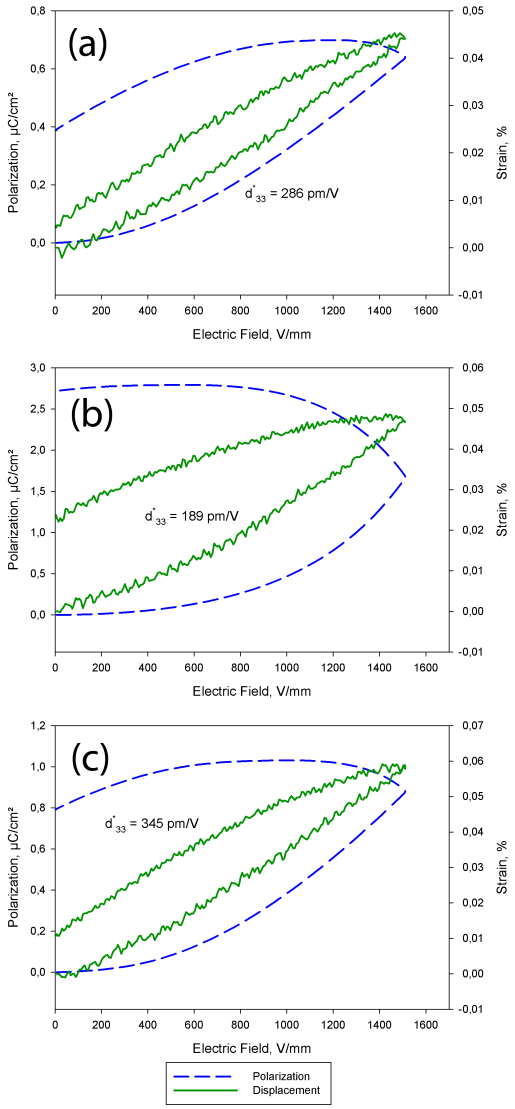

Figure I.1: Unipolar polarization-displacement measurements for the LKNNT sample sintered using the conventional method, made seconds after one another. The measurements were made at room temperature, using a frequency of 1 Hz and an electric field of 1.5 kV mm, and (a) 24 hours after poling, (b) after applying a bipolar burst, (c) after a 3 $\frac{kV}{mm}$ poling burst.

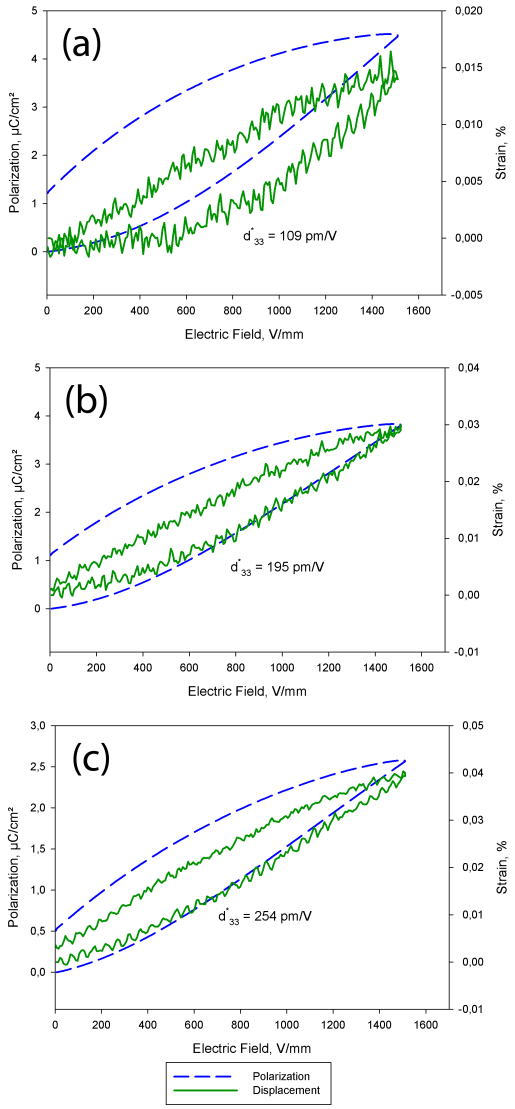

Figure I.2: Unipolar polarization-displacement measurements for the LKNNT sample sintered using the direct insertion method,. The measurements were made at room temperature, using a frequency of 1 Hz and an electric field of 1.5 $\frac{kV}{mm}$, and (a) without any poling, (b) after applying a unipolar 4 $\frac{kV}{mm}$ burst, (c) 6 hours of aging after the burst.